

DEPARTMENT OF PHYSICS
UNIVERSITY OF JYVÄSKYLÄ
RESEARCH REPORT No. 4/2018

Modeling of intracellular transport in realistic cell geometries

Vesa Aho

Academic Dissertation
for the Degree of
Doctor of Philosophy

*To be presented, by permission of the
Faculty of Mathematics and Natural Sciences
of the University of Jyväskylä,
for public examination in Auditorium FYS1 of the
University of Jyväskylä on April 6th, 2018
at 12 o'clock noon*

JYVÄSKYLÄ, FINLAND 2018

ABSTRACT

Aho, Vesa

Modeling of intracellular transport in realistic cell geometries

Jyväskylä: University of Jyväskylä, 2018, 61 p.

(Department of physics, University of Jyväskylä, Research Report No. 4/2018

ISSN 0075-465X)

ISBN 978-951-39-7384-1 (paper copy)

ISBN 978-951-39-7385-8 (pdf)

The transport of molecules inside cells is a complex process, the characterization of which is important to gain full understanding of cellular processes. Understanding of intracellular transport is also important for medical applications, for example when analyzing transport of medicine inside cells. The intracellular environment is very complex, and at least the most crucial parts of this complexity must be accounted for to solve transport problems in cells. In this thesis the results of studies in modeling intracellular transport are presented. The aim of the work was to model intracellular transport of proteins and viral capsids in realistic cell environments. To this end, microscopic methods were used to image cellular structures, which were then digitally reconstructed and used as an environment for modeling particle transport in numerical simulations.

Keywords: Intracellular transport, numerical modeling, viral transport, diffusion, lattice-Boltzmann method, random walk, image analysis

Author

Vesa Aho
Department of Physics
University of Jyväskylä
Jyväskylä, Finland

Supervisors

Adjunct Professor Maija Vihinen-Ranta
Department of Biological and Environmental Science
University of Jyväskylä
Jyväskylä, Finland

Professor Jussi Timonen
Department of Physics
University of Jyväskylä
Jyväskylä, Finland

Adjunct Professor Keijo Mattila
Department of Physics
University of Jyväskylä
Jyväskylä, Finland

Adjunct Professor Thomas Kühn
Department of Applied Physics
University of Eastern Finland
Kuopio, Finland

Reviewers

Adjunct Professor Jari Hyväluoma
Natural Resources Institute
Jokioinen, Finland

Professor Andre S. Ribeiro
Biomeditech Institute
University of Tampere
Tampere, Finland

Opponent

Professor Matthias Weiss
Department of Physics
University of Bayreuth
Bayreuth, Germany

ACKNOWLEDGEMENTS

The work reported in this thesis was carried out during the years 2011-2017 at the Department of Physics and the Department of Biological and Environmental Science at the University of Jyväskylä, Finland. This work is part of a collaboration between the groups of professor Jussi Timonen and adjunct professor Maija Vihinen-Ranta, and I am deeply grateful for their guidance and support. I would also like to express my gratitude to Thomas Kühn and Keijo Mattila for practical instructions I have received during my work. I would like to thank adjunct professor Jari Hyväluoma and professor Andre S. Ribeiro for providing valuable comments to help me improve this thesis.

The numerous colleagues I have worked with at the Department of Biological and Environmental Science have introduced me to the world of cellular biology and created a friendly and relaxed atmosphere in the workplace. I would like to thank Sami Willman, Elina Mäntylä, Jori Virtanen, Visa Ruokolainen, Artur Kazmertsuk, Satu Hakanen and Salla Mattola among others for sharing the ups and downs of scientific research.

Although support from my colleagues was crucial to this work, the biggest thanks go to my family. I would like to thank my parents for their loving care and upbringing. Finally, and most importantly, I want to thank my wife and daughters, who have always supported me and given me joy beyond words. They have made this journey worth taking.

Jyväskylä, February 22th, 2018
Vesa Aho

LIST OF PUBLICATIONS

- I Aho, V., Mattila, K., Kühn, T., Kekäläinen, P., Pulkkinen, O., Brondani Minussi, R., Vihinen-Ranta, M. & Timonen, J. 2016. Diffusion through thin membranes: Modeling across scales. *Physical Review E* 93, 043309.
- II Myllys, M., Ruokolainen, V., Aho, V., Smith, E. A., Hakanen, S., Peri, P., Salvetti, A., Timonen, J., Hukkanen, V., Larabell, C. A. & Vihinen-Ranta, M. 2016. Herpes simplex virus 1 induces egress channels through marginalized host chromatin. *Scientific Reports* 6:28844.
- III Aho, V., Myllys, M., Ruokolainen, V., Hakanen, S., Mäntylä, E., Virtanen, J., Hukkanen, V., Kühn, T., Timonen, J., Mattila, K., Larabell, C. A. & Vihinen-Ranta, M. 2017. Chromatin organization regulates viral egress dynamics. *Scientific Reports* 7:3692.
- IV Aho, V., Ohkawa, T., Chen, J. H., Kühn, T., Mattila, K., Volkman, L., Larabell, C. A., Welch, M. D. & Vihinen-Ranta, M. 2018. Actin-propelled navigation of baculovirus through the chromatin network. Manuscript.

The author has designed and performed all the numerical simulations of publications III, and IV, and most of the simulations, especially the simulations in the cellular environment, of publication I. He has also been the principal author and performed most of the data analysis in those three publications. In addition, the author has performed part of the data analysis and contributed to the writing of publication II.

CONTENTS

ABSTRACT

ACKNOWLEDGEMENTS

LIST OF PUBLICATIONS

CONTENTS

1	INTRODUCTION	10
2	THEORY OF DIFFUSION.....	12
2.1	Particle-level description	12
2.1.1	Mean displacement and mean squared displacement	12
2.1.2	Anomalous diffusion.....	14
2.2	Continuum-level description.....	15
2.2.1	Fick's laws and diffusion equation.....	16
2.2.2	Diffusion through a membrane.....	17
3	INTRACELLULAR TRANSPORT	19
3.1	Timescales of intracellular transport - active and passive transport	19
3.2	Transport in cytoplasm and nucleus.....	21
3.3	Transport across the plasma and nuclear membranes.....	23
3.4	Transport of viral capsids and proteins in cells	24
3.4.1	Diffusion of HSV-1 in cell nucleus.....	25
3.4.2	Active motion of baculovirus in cells.....	26
4	NUMERICAL MODELING OF PARTICLE MOTION IN CELLS.....	27
4.1	The lattice-Boltzmann method.....	27
4.2	The random walk method	29
4.3	Modeling in image-based geometries.....	30
4.3.1	Imaging three-dimensional structure of cells - confocal fluorescence microscopy and soft x-ray tomography.....	30
4.3.2	Segmenting the cell and the nucleus	32
4.3.3	Obstructions to bulk diffusion and the problem of nonuniform equilibrium distribution.....	33
4.3.4	Modeling diffusion through membranes	35
5	EXPERIMENTAL METHODS.....	37
5.1	Confocal fluorescence microscopy of living cells	37
5.2	Soft x-ray tomography of HSV-1- and baculovirus-infected cells.....	38
5.3	Lattice-Boltzmann simulation of nuclear envelope permeation by EYFP.....	38
5.4	Random walk simulation of HSV-1 capsids in the nucleus	39
5.5	Correlated random walk simulation of baculovirus capsids in the nucleus.....	40

6	RESULTS OF MODELING BIOMOLECULE TRANSPORT IN CELLS.....	42
6.1	Determination of nuclear envelope permeability to fluorescent molecules.....	42
6.2	Diffusion of HSV-1 capsids in the nucleus	45
6.3	Active motion of baculovirus capsids in the nucleus.....	48
7	SUMMARY	51
	REFERENCES.....	53

1 INTRODUCTION

Everyone has an intuitive notion of what the word *motion* means. Everything around us, ourselves included, is in constant motion. We are currently speeding over a hundred thousand kilometers per hour around the Sun. The entire Earth is also rotating around its axis, making a full revolution once a day.

Coming down from the celestial scale to the scale of human beings, the everyday experience is that to start or maintain motion, a force needs to be supplied to the body being moved. Once the body is moving, it is said to possess kinetic energy. The mechanism that prevents objects from moving indefinitely is friction, which occurs when the moving body interacts with its surroundings, such as water around a swimmer or the surface under a sliding object. As a result of friction, the body transfers energy to its surroundings and slows down. In the process the surroundings heat up.

So, on a large scale the fact that things are surrounded by substances, like for instance the atmosphere, slows them down. For this reason, it might be surprising that in a small enough scale the molecules of the surrounding medium actually help things to move. The molecules of the atmosphere are constantly moving around and hitting us, exerting extremely small forces on our bodies. While we are too massive to be moved by these collisions, the same is not true for a grain of pollen in water, for example. The numerous collisions of water molecules are not always balanced, and occasionally more molecules hit the grain from one side than from the other. As a result, the pollen grain moves in a random way. This type of a motion is called Brownian motion, named after its discoverer Robert Brown. Brownian motion of particles gives rise to diffusion, which is the motion of substances from the areas of high concentration to the areas of lower concentration. One characteristic of diffusional motion is that it is efficient only over very short distances. For example, it takes a few seconds for a typical protein to diffuse the distance of ten micrometers, but the corresponding time for a distance of one millimeter is more than twelve hours! The size of a typical human cell is about ten micrometers, so diffusion is an important method of transport at the cellular scale.

In some cases, diffusional transport is too slow, which is why cells also use active transport, where a molecule uses energy to move or is actively moved by another molecule in a directed manner, as opposed to the random thermal motion. A common example of active motion is the transport of cargo on cell cytoskeletal fibers by motor proteins. Many bacteria and even some viruses utilize active transport.

Understanding these various forms of transport at the cellular scale enables us to find more pieces to the puzzle of life. The transport of molecules inside cells is also important in medical applications, where efficient transport of medicine to the site-of-action is required. It has been proposed that some of the nervous system diseases, such as ALS and Alzheimer's disease, might be partly explained by faulty transport in nerve cells.

Even though the experimental tools of biology, especially microscopy methods, have evolved at an amazing rate, there are still limitations to direct observations of particle motion inside cells. To gain more insight into these phenomena, we have developed computational tools to model intracellular transport. The environment inside a cell is highly complex, including for example the chromatin network and membrane structures. In order to realistically model intracellular transport, the essential features of this environment must be captured and incorporated into a model. The focus of this work was to more accurately model intracellular transport by utilizing realistic environments reconstructed from images obtained with microscopy methods.

The first part of this work consists of modeling diffusion through the nuclear envelope. In this study, the permeability of the nuclear envelope to a fluorescent molecule is determined by comparing simulated changes in the fluorophore distribution to changes measured in a fluorescence microscopy experiment. The second part of this work consists of modeling the diffusive motion of herpes simplex virus 1 capsids towards the nuclear envelope through the chromatin network that is characterized using soft x-ray tomography imaging. The last part of this work was done to model the active, actin-propelled motion of baculovirus capsids in the cell nucleus. In conclusion, it will be shown that simulating the motion of particles in the reconstructions of their actual environments allows us to gain new insights into intracellular transport phenomena.

In Chapters 2-3, the theory of mass transport in general and in the cellular environment are outlined. In Chapter 4 the numerical modeling of transport, especially in a cellular environment, is considered. The microscopy methods used in the experiments and the simulation setups are discussed in Chapter 5, and finally, the results of our modeling studies in the cellular environment are presented in Chapter 6.

2 THEORY OF DIFFUSION

The molecules of matter are incessantly moving around in thermal motion. The statistics of this motion gives rise to diffusion, which is manifested by the net motion of particles from regions of high concentration to regions of low concentration. Thermal motion also gives rise to Brownian motion of particles suspended in a fluid. In this chapter, particle- and continuum-level descriptions of diffusion are given.

2.1 Particle-level description

The motion of a particle moving in a fluid is far from being deterministic. The particle is constantly colliding with other fluid particles, which affects its motion in a random manner, making the calculation of its path an impossible task. However, if the motion of many identical particles is observed, it turns out that despite the inherent randomness the average quantities of motion follow precise physical laws. In this section the microscopic theory of diffusion is outlined, and the laws governing the motion of individual particles on average are considered.

2.1.1 Mean displacement and mean squared displacement

Due to collisions with the surrounding particles of the fluid, the movements of one particle in a fluid are random. In this random motion no direction is preferred over any other, and therefore the mean position of many particles does not change over time (for random movements in any direction, there are on average as many movements in the opposite direction). In one dimension, for example, the total displacement of a particle after n movements, x_n , can be described as a series of consecutive movements Δx_i :

$$x_n = \sum_{i=1}^n \Delta x_i = \Delta x_1 + \Delta x_2 + \cdots + \Delta x_n. \quad (1)$$

For non-biased motion, each of the displacements Δx can be either negative or positive, and the jumps to the positive direction have on average the same length as the jumps to the negative direction. For this reason, when averaged over many experiments or many particles, the mean of each of the individual displacements, $\langle \Delta x_i \rangle$, is zero. Therefore, the mean displacement after n movements, $\langle x_n \rangle$, is

$$\langle x_n \rangle = \langle \Delta x_1 \rangle + \langle \Delta x_2 \rangle + \cdots + \langle \Delta x_n \rangle = 0. \quad (2)$$

Although the mean position does not change, diffusion causes the particles to spread out from their initial location. This is illustrated in Figure 1, where the mean location of the particles is approximately at the origin, but the particle distribution spreads when time increases. Because the mean displacement of a particle is always zero, it is not a very useful quantity to describe diffusional behavior. A better quantity, which captures the spreading of particles in the course of time, is the variance of the position with respect to the initial position, also known as the mean squared displacement. The increase of the mean squared displacement over time can be shown by looking at the square of the particle displacement after n movements:

$$\begin{aligned} x_n^2 &= \left(\sum_{i=1}^n x_i \right)^2 = (\Delta x_1 + \Delta x_2 + \cdots + \Delta x_n) \cdot (\Delta x_1 + \Delta x_2 + \cdots + \Delta x_n) \\ &= \sum_{i=1}^n (\Delta x_i)^2 + \sum_{j=1}^n \sum_{k \neq j}^n \Delta x_j \Delta x_k. \end{aligned} \quad (3)$$

When the squared displacement is averaged over many experiments, the second term is as likely to be positive as negative and is on average zero, resulting in

$$\langle x_n^2 \rangle = n \langle \Delta x^2 \rangle. \quad (4)$$

Because the number of movements is proportional to the observation time, in regular diffusion the mean squared displacement is proportional to time. The mean squared displacement also depends on the dimensionality of the system. To generalize to an arbitrary number of dimensions, d , and starting point, \mathbf{r}_0 , the mean displacement and the mean squared displacement of a diffusing particle are

$$\begin{aligned} \langle \mathbf{r}(t) - \mathbf{r}_0 \rangle &= 0 \\ MSD &= \langle (\mathbf{r}(t) - \mathbf{r}_0)^2 \rangle = 2dDt, \end{aligned} \quad (5)$$

where $\mathbf{r}(t)$ is the location of a particle at time t . The diffusion coefficient D tells how fast the motion of particles occur, and it depends on the size of the particle and on the properties of the surrounding medium. If the mean squared displacement of particles can be measured, the diffusion coefficient of the particles can be directly calculated using Equation (5).

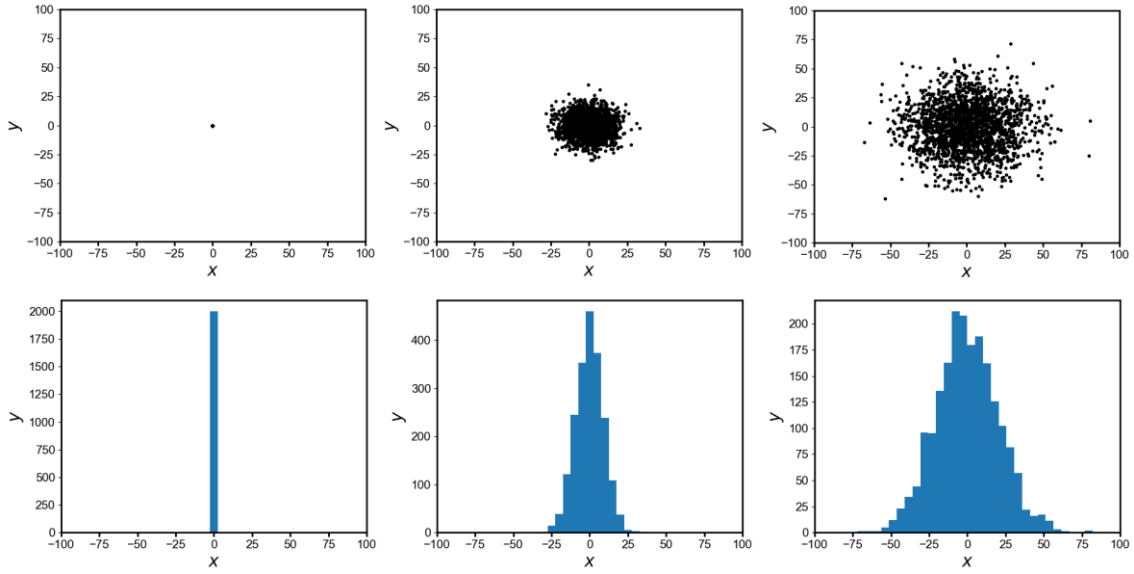


Figure 1. Diffusion of 2000 non-interacting particles from the origin at increasing times (top row), and the concentration profile of particles in the x -direction at corresponding times (bottom row). The diffusion of particles was modeled using a random walk algorithm. Note that the mean of the distribution is always approximately at the origin. Notice also the approximate Gaussian shape of the distribution (see Section 2.2.1).

2.1.2 Anomalous diffusion

According to Equation (5), in regular diffusion the mean squared displacement is proportional to time. This can be generalized to non-linear time dependency:

$$MSD = 2dDt^\alpha. \quad (6)$$

The case $\alpha = 1$ corresponds to regular diffusion, but in many transport processes so-called anomalous diffusion ($\alpha \neq 1$) is observed (Klafter & Sokolov 2005). In anomalous diffusion, the case $\alpha < 1$ is called subdiffusion and $\alpha > 1$ superdiffusion. Subdiffusion usually arises when the diffusive motion is confined or obstructed by the environment (a typical situation, for example, inside cells). Consider, for example, particles moving in the limited space constricted by solid obstacles (Figure 2). At the short time scale, when the particles move between the obstacles, the motion is well represented by regular diffusion (linear $MSD(t)$). When the particles start to encounter obstacles, the mean squared displacement decreases as a function of time. At this time scale the restricted motion is manifested as subdiffusion. At still longer time scales the particles need to find detours around the obstacles in order to spread further. In effect, the particle pathways become more tortuous when compared to unrestricted motion over a given distance. At this time scale the motion is well represented by regular diffusion again, but now the spreading of particles is slower than at the shortest time scale. In other words, the motion along more tortuous pathways can be captured by adopting an effective diffusion coefficient that is smaller in value than the intrinsic, particle-fluid diffusion coefficient. The effective diffusion coefficient depends both on the unobstructed diffusion coefficient in the pure liquid and the size and distribution of the obstacles.

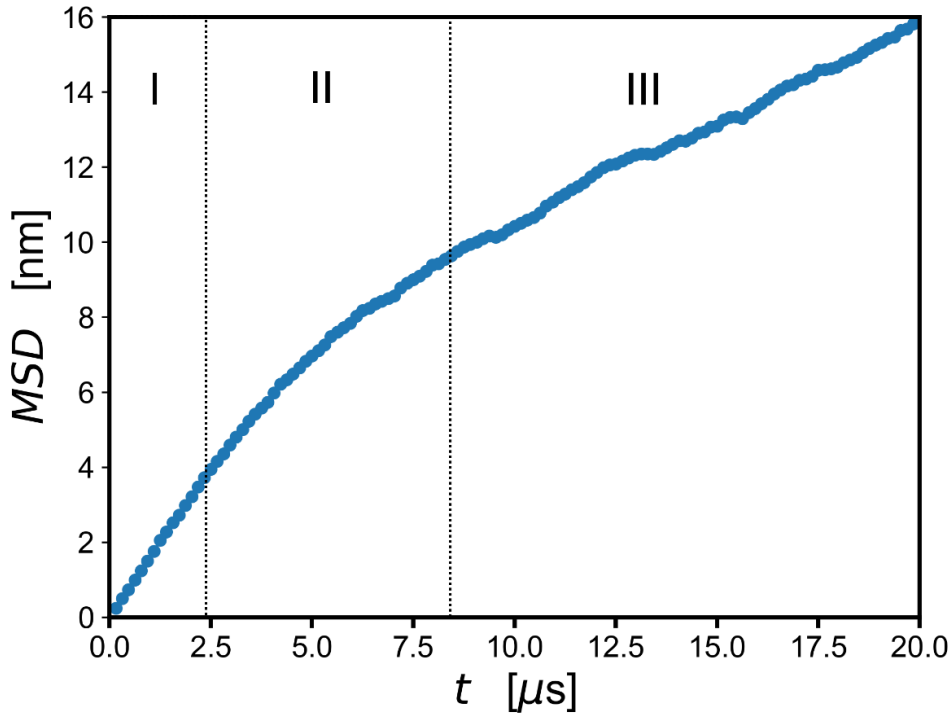


Figure 2. The mean squared displacement of 2000 particles diffusing among obstacles. The particle motion was simulated using a two-dimensional random walk. Spherical obstacles of diameter 90 nm were placed on a grid such that the distance between the obstacle centers in the x - and y -directions was 100 nm. The initial location of the particles was at the center of the free space between the obstacles. The diffusion coefficient of the particles was $10 \mu\text{m}^2/\text{s}$ and they were assumed to be negligibly small compared to the obstacle size. At the beginning (region I) the motion is diffusive (linear MSD), followed by a subdiffusive period (region II), and at later times the motion is again diffusive (region III). Note that the effective diffusion coefficient at the later times is lower than the intrinsic diffusion coefficient at the beginning.

An example of superdiffusion is Lévy flight, where regular diffusion is occasionally interrupted by more directed movements to a new region. This kind of motion is seen in nature for example in the movement of marine predators (Viswanathan et al. 1996) and bacteria (Ariel et al. 2015), or in active intracellular transport (Reverey et al. 2015).

2.2 Continuum-level description

Instead of considering the motion of individual particles, it is often useful to consider the concentration of particles, $c(\mathbf{r}, t)$, which is the number of particles averaged over a small volume. The interest is then in solving the concentration as a function of position \mathbf{r} and time t . When the concentration of diffusing particles is observed, it is found, for example, that on average the particles tend to move from regions of high concentration to regions of low concentration, which means that differences in the concentration tend to disappear over time. In this

section, a macroscopic theory of diffusion is presented and diffusion through a membrane is considered.

2.2.1 Fick's laws and diffusion equation

If the movement of particles in a fluid is random, the mean location of one particle does not change. To understand how the random motion of individual particles can lead to a deterministic motion of a large number of particles, we can examine a case where the concentration of particles is not uniform but depends on the position within the fluid (Figure 3). For two positions close to each other with concentrations c_1 and c_2 , separated by an imaginary surface, the probability for any particle to cross the surface is the same. For this reason, the number of particles crossing the surface from one side to another must be proportional to the number of particles on that side. This means that the total flux of particles (the number of particles crossing to the right side minus the number crossing to the left side) through the surface is proportional to the concentration difference over the surface.

The flux \mathbf{J} of diffusing molecules (the net number of particles crossing a surface in a unit time) is given by Fick's first law

$$\mathbf{J} = -D \nabla c. \quad (9)$$

Combining Fick's first law with the continuity equation,

$$\frac{\partial c}{\partial t} = -\nabla \cdot \mathbf{J}, \quad (10)$$

results in the diffusion equation (also known as Fick's second law):

$$\frac{\partial c}{\partial t} = \nabla \cdot (D \nabla c). \quad (11)$$

The solution of the diffusion equation in one dimension when the concentration is initially c_0 at the origin and zero elsewhere is (Einstein 1905)

$$c(x, t) = \frac{c_0}{\sqrt{4\pi Dt}} e^{-\frac{x^2}{4Dt}}. \quad (12)$$

This is a Gaussian distribution with standard deviation $\sqrt{2Dt}$. If the standard deviation of the concentration is taken as the typical distance the particles travel during time t , an estimate can be derived for the typical time it takes a particle with diffusion coefficient D to travel a distance x :

$$t_D = \frac{x^2}{2D}. \quad (13)$$

This is in principle the same result that was obtained for the microscopic picture in Equation (5). The x^2 -dependency is the reason why diffusion is an efficient method of transport at short distance scales but not at longer scales.

It is intuitive that the diffusion coefficient of a particle depends on the temperature T and viscosity η of the solvent. For a spherical particle of radius R in a viscous fluid, it can be shown that the diffusion coefficient follows the Stokes-Einstein relation,

$$D = \frac{k_B T}{6\pi\eta R}, \quad (14)$$

where k_B is the Boltzmann constant.

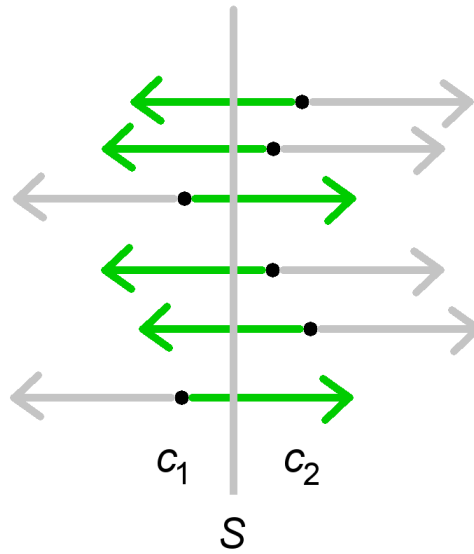


Figure 3. Flux caused by a concentration gradient. Every particle has an equal probability to jump either left or right, and, as $c_2 > c_1$, the number of particles crossing over the surface S (green arrows) from right to left is higher than from left to right. The total flux is proportional to the difference $c_2 - c_1$.

2.2.2 Diffusion through a membrane

The explanation above for Fick's first law can be expanded to a case where the surface between two points is no longer imaginary, but an actual membrane separating these points.

Assuming that there is a volume of liquid that is divided into two parts by a membrane, and the other part is filled with liquid where the concentration of particles is c_1 and the other part with liquid of concentration c_2 , there exists a density difference $\Delta c = c_2 - c_1$ between the two parts. The flux through the membrane is, as above, proportional to the concentration difference between the two sides:

$$J = -P \Delta c. \quad (15)$$

The constant of proportionality, P , is the permeability of the membrane. In a solubility-diffusion model, for example, the permeability can be written as

$$P = \frac{KD_m}{w}, \quad (16)$$

where K is the solubility of the permeating molecule in the membrane, D_m is the intrinsic diffusion coefficient of the membrane, and w is the width of the membrane (Finkelstein 1976).

An important example is the experimental determination of the permeability of a membrane-enclosed compartment of volume V and surface area A . The change of total mass inside the compartment, m_{tot} , depends on the flux that passes through the membrane:

$$\frac{dm_{tot}}{dt} = JA = -P\Delta cA. \quad (17)$$

If transport through the membrane is assumed slow compared to transport within and outside of the compartment (implying uniform concentrations both inside and outside the compartment), and the mean concentrations inside and outside the compartments are written as c_{in} and c_{out} , then the above equation can be written as

$$V \frac{dc_{in}}{dt} = -P(c_{in} - c_{out})A. \quad (18)$$

With the further assumption that c_{out} does not depend on time, i.e. the volume of the compartment interior is small compared to its exterior, the above equation may be solved as a separable differential equation for c_{in} :

$$c_{in} = c_{out} - (c_{out} - c_0)e^{-\frac{PA}{V}t}. \quad (19)$$

In the above equation c_0 is the concentration inside the compartment at $t = 0$. If the concentrations inside and outside the compartment can be measured as a function of time, the permeability of the enclosing membrane can be calculated from Equation (19).

3 INTRACELLULAR TRANSPORT

Cells are compartmentalized complexes, meaning that they have specific areas where cellular functions such as the synthesis of proteins, DNA replication and adenosine triphosphate (ATP) production occur. Because of the compartmentalization, transport of molecules between the various parts of the cell is essential for cellular functions. An illustrative example is the synthesis of proteins. The genetic code for the protein synthesis is located in the DNA inside the nucleus, where this information is copied into a messenger RNA molecule in a process called transcription. The messenger RNA must then travel out of the nucleus through a nuclear pore of the nuclear envelope to the cytoplasmic ribosomes, where the RNA code is then translated into a protein. If the protein is needed in the nucleus, such as DNA polymerases required for DNA replication, the transport leads back to the nucleus through a nuclear pore.

In this chapter, the basic principles of intracellular transport are discussed first. Then transport in the crowded cellular compartments of cytoplasm and nucleus are described. We also illustrate transport through the plasma membrane and nuclear envelope, and finally give a brief explanation of the transport of viruses in cells, giving two examples that are related to the experimental part of this work.

3.1 Timescales of intracellular transport – active and passive transport

In this thesis, the focus is on the eukaryotic cell, the main building block of humans, plants and fungi (Figure 4). A typical size scale of an animal cell diameter is 10 μm . A protein with diffusion coefficient $D \sim 10 \mu\text{m}^2/\text{s}$ is able to diffuse this distance, according to Equation (13), in about five seconds. If the diffusion coefficient decreases to $0.02 \mu\text{m}^2/\text{s}$, a value that has been measured for herpesvirus capsids in the nucleus of the cell (Bosse et al. 2015), the time increases to over one hour, which is probably why cytoplasmic transport of herpesviruses is car-

ried out by the motor protein dynein that moves on microtubules (Sodeik, Eberold & Helenius 1997).

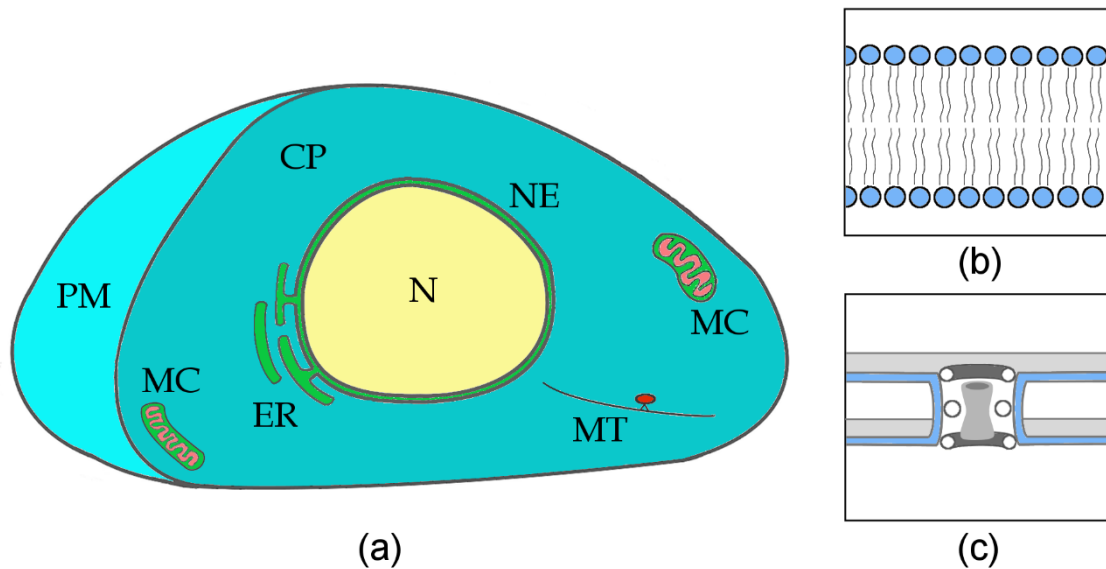


Figure 4. (a) A schematic of an eukaryotic cell cross section, showing the plasma membrane (PM), cytoplasm (CP), nuclear envelope (NE) and nucleus (N). Mitochondria (MC), an active transport of a vesicle by a motor protein on a microtubulus (MT) and a part of the endoplasmic reticulum (ER) are also shown. (b) A schematic of the plasma membrane, consisting of lipid bilayer of phospholipid molecules arranged with their hydrophobic tails pointing toward each other. (c) The nuclear envelope, consisting of two lipid bilayers and nuclear pore complexes forming channels across the envelope for particle transport.

The motion inside cells can be divided into two cases: passive and active. Passive motion, which is in this thesis interchangeably called diffusion, is driven by the thermal motion of the surrounding molecules. This type of motion is usually random, and no direction is preferred over another. Due to the small size of most cells, diffusion is an efficient method of transport inside them. The size of the diffusing particle also affects the diffusion rate (see Equation (14)), which is why smaller molecules almost always travel passively in the cell. Table I gives estimates of some molecules and their diffusion times over several distances. Since diffusion times for large molecules are so long, cells (and some viruses) have developed other means of transport.

Active motion, regularly used by large molecules and particles, such as virus particles and vesicles, is often directed and requires a source of energy, such as the energy gained by converting ATP to adenosine diphosphate (ADP). During active transport molecules are moved by cellular proteins that are specialized in binding to the transported molecule and moving it to other parts of the cell, usually along cable-like filaments that form the cell cytoskeleton (by motor proteins), across the plasma membrane (by carrier proteins) or across the nuclear envelope (by karyopherins). Even if the particle is moving actively, it is usually subject to diffusive motion as well.

Table I. Estimated diffusion times for some molecules over various length scales.

Distance	Calcium ion $D \sim 1000 \mu\text{m}^2/\text{s}$	Green fluorescent protein (GFP), $D \sim 10 \mu\text{m}^2/\text{s}$	HSV-1 capsid $D \sim 10^{-2} \mu\text{m}^2/\text{s}$
100 nm	5 microseconds	0.5 milliseconds	0.5 seconds
1 μm	0.5 milliseconds	50 milliseconds	50 seconds
10 μm	50 milliseconds	5 seconds	5000 seconds

The thermal energy of a diffusing particle is of the order $k_B T$, whereas the hydrolysis of a single ATP molecule to an ADP molecule yields over $20k_B T$ of energy in physiological conditions (Phillips et al. 2012). As an example, the motor protein kinesin moves 8 nm when it hydrolyses a single ATP (Schnitzer & Block 1997). When this is combined with the observation that these proteins move up to 800 nm per second (Visscher, Schnitzer & Block 1999), it can be estimated that kinesin can hydrolyze 100 molecules of ATP to ADP per second, which is a tremendous amount of energy at the cellular scale. These findings also indicate that actively transported molecules need to be large enough in order to gain significant advantage over diffusion. The diffusion time for a molecule with $D = 10 \mu\text{m}^2/\text{s}$, which is true for a typical protein, to diffuse a distance of 10 micrometers is about five seconds, while active transport using kinesin would take twice as long.

The diffusion coefficient is proportional to the temperature (see Equation (14)). Therefore, the difference in the passive transport rates between, for example, the physiological temperature (310 K) and room temperature (293 K) is only about six percent. Active transport on the other hand has a stronger dependence on the temperature due to the exponential relation between the binding reaction rate k and temperature,

$$k = A e^{-\frac{E_a}{k_B T}}, \quad (20)$$

which increases rapidly as a function of T in typical conditions, where $E_a \gg k_B T$. For this reason, measuring the transport rate at various temperatures can give information on whether the process is passive or active in nature. Another method is to measure dynamics before and after depleting cellular ATP with, for example, sodium azide and 2-deoxyglucose.

3.2 Transport in cytoplasm and nucleus

The cytoplasm of the cell is a crowded environment containing, for example, cytoskeletal networks, vesicles, mitochondria and the endoplasmic reticulum (Luby-Phelps 2000). The diffusion coefficient of a 27 kDa protein has been measured to be several times lower in the cell cytoplasm than in pure water (Potma et al. 2001, Kühn et al. 2011), and most of this decrease is probably explained by the obstacle-induced reduction of the protein diffusion volume (No-

vak, Kraikivski & Slepchenko 2009). A common way to analyze diffusion in obstructed space is to determine the porosity of the material, ε , which is the ratio of available space to the total space. If the diffusion coefficient in a pure solution without obstructions (when $\varepsilon = 1$) is D_0 , the effective diffusion coefficient in a porous material filled with the same solution is then (neglecting tortuosity of the material) given by

$$D = \varepsilon D_0. \quad (21)$$

Although more commonly used in geological applications, this approach has also been applied to analyze diffusion of fluorescent molecules in the cellular environment (Kühn et al. 2011, Aho et al. 2016). The fluorescence intensity at a certain location is higher if there is more free space available at that location to hold the fluorescent molecules. For this reason, the porosity and diffusion coefficient were in the above studies assumed to be proportional to the fluorescence intensity of the observed molecules. Because the cytoplasm of the cell is such a crowded environment filled with obstacles, the motion in the cytoplasm may under some conditions be subdiffusive (see Section 2.1.2), which has been observed in animal and bacterial cells (Weiss et al. 2004, Golding & Cox 2006).

Because the cytoplasm is usually the largest part of the cell, it is natural that the cytoplasmic transport of large molecules is often active in nature, resulting in more efficient transport between the various parts of the cell. The active transport in the cytoplasm is carried out by motor proteins that move along actin and microtubule fibers. Actin has one associated motor protein, myosin (Sweeney & Houdusse 2010, Syamaladevi, Spudich & Sowdhamini 2012), and myosin motion along actin fibers plays a crucial role, for example, in the contraction of muscle cells (Piazzesi et al. 2007). Microtubule has two associated motor proteins, kinesin and dynein (Roberts et al. 2013, Woehlke & Schliwa 2000). Microtubules are polar structures, and they are usually arranged in such a way that the so-called minus ends are located near the cell center and nucleus, coming together in a microtubule organizing center, and the plus ends are located near the cell periphery and the plasma membrane. The motor protein kinesin prefers to move towards the plus ends of the microtubules, so they are responsible for transporting cargo, such as secretory vesicles, towards the cell periphery. Dyneins on the other hand move cargo, such as endocytic vesicles, from the cell periphery towards the center of the cell. Active transport by motor proteins is especially important for nerve cells, which in humans can be up to a meter long. Transport over such distances depends strongly on the active, directed motion over cytoskeletal networks (Franker & Hoogenraad 2013).

The cell nucleus, separated from the cytoplasm by the nuclear envelope, contains the DNA of the cell. The 2 nm thin DNA strand is compactly packed by being wound around large globular structures, consisting of eight histone proteins. The combination of the histone core and the DNA wound around it is called the nucleosome. In every nucleosome, 146 base pairs of DNA are wrapped around the histones (Luger et al. 1997), and the nucleosomes are linked to each other with a short length (10-80 base pairs) of DNA. This complex of packed DNA and histones is called chromatin. The DNA of a cell can be

over a meter long, but the packaging helps to fit it into a nucleus of $\sim 10 \mu\text{m}$ in diameter. Chromatin exists in two forms, euchromatin and heterochromatin. Euchromatin is less densely packed, containing genes that are actively expressed, whereas more densely-packed heterochromatin contains inactive genes.

Like the cytoplasm, the nucleus is also a large, crowded intracellular region. For this reason, the above discussion concerning passive cytoplasmic transport is applicable to passive transport in the nucleus as well. As in the cytoplasm, the diffusion coefficient in the nucleus is likewise several times lower than in water (Dross et al. 2009, Aho et al. 2016), and anomalous subdiffusion has been observed there (Wachsmuth, Waldeck & Langowski 2000, Bronstein et al. 2009). Smaller molecules can move in the nucleus relatively freely, but larger molecules are obstructed by the chromatin network. Large particles (of size $\sim 100 \text{ nm}$ or larger) are mostly confined in the interchromatin regions (so called chromatin corrals), and they can move inside the corrals rather freely, but their movement over longer distances is dependent on the movement of the corrals (Görisch et al. 2004). The chromatin is a moving and changing structure, but this motion is usually slow; the diffusion coefficient of chromatin has been estimated to be about $10^{-3} - 10^{-4} \mu\text{m}^2/\text{s}$ (Dion & Gasser 2013).

3.3 Transport across the plasma and nuclear membranes

The cell is separated from its exterior by a less than 10 nm thick (Schneiter et al. 1999) membrane called the plasma membrane or the cell membrane. The plasma membrane is a lipid bilayer, which is a common membrane structure in cells, consisting of two layers of phospholipid molecules (see Figure 4b). The plasma membrane phospholipids are amphipathic molecules that have a hydrophilic head and a hydrophobic tail. This enables them to arrange in the watery cellular environment spontaneously into a membrane where the tails are positioned against each other, and the heads point out to the surface of the membrane.

Many lipid-soluble molecules and neutral, small molecules are able to pass through the plasma membrane diffusively. The permeability of the membrane is low for many large molecules, polar molecules, charged molecules and ions. These molecules have to utilize protein-mediated transport in the form of carrier proteins or channel proteins embedded in the membrane. The carrier proteins bind their cargo on one side of the membrane and then change their conformation so that the cargo moves to the other side of the membrane. Channel proteins on the other hand maintain an open aqueous channel through the membrane, allowing molecules to pass through. Another form of active transport across the plasma membrane is endo- and exocytosis, where the imported (or exported) molecules are engulfed by the membrane, resulting in a lipid-coated vesicle that contains the molecule.

As manifested by Equation (15), diffusive transport across a membrane results in net transfer of molecules from the side of the membrane where the concentration is higher to the side where it is lower. To move molecules against a

concentration gradient, which is important, for example, to maintain a potential difference over the plasma membrane, the cell must use energy in the process, and active transport must be utilized. The potential difference is achieved by sodium-potassium pumps, which are transmembrane proteins that transport sodium ions out of the cell and potassium ions into the cell. During one cycle, three sodium ions are transported out of and two potassium ions into the cell.

The traffic of molecules between the cytoplasm and nucleus is restricted by the nuclear envelope (see Figure 4c). It consists of two lipid bilayers separated by an intermembrane space of about 30-50 nm (Franke et al. 1981). The transport of most molecules in and out of the nucleus occurs through massive, 60 MDa protein complexes, called nuclear pores (Cronshaw et al. 2002). The nuclear pores form channels through the envelope, and there can be thousands of nuclear pores in the nuclear envelope (Maul et al. 1972, Maul & Deaven 1977). Immuno-electron microscopy has shown that the diameter of the inner channel of a nuclear pore is about 38 nm (Alber et al. 2007), which is in accordance with the observation that the maximum diameter of particles that can be translocated through the pore is 39 nm (Pante & Kann 2002). However, only smaller molecules (up to about 12.5-14.5 nm (Feldherr 1965) or 60 kDa) can freely diffuse through the nuclear pores, whereas larger molecules need active transport mediated by a specialized class of proteins called karyopherins. Recently, it has been shown that the size limit is not absolute, and the structure of the nuclear pore allows diffusion of molecules over 100 kDa in mass (Wang & Brattain 2007) with gradually decreasing permeability as a function of the molecule mass (Timney et al. 2016).

Passive transport across the nuclear envelope is proportional to the concentration difference on the two sides of the membrane, according to Equation (15). However, this cannot be true for active transport in general. It is intuitive that active transport depends not only on the concentration of transported molecules but also on the availability of the transporting proteins.

3.4 Transport of viral capsids and proteins in cells

The life cycle of viruses is dependent on their efficient transport inside the cell. This is especially true for most DNA viruses, which need to get their genomes into the nucleus for replication by either passing through the nuclear envelope intact, or by releasing the viral genome at the nuclear envelope so that it can travel through a nuclear pore. After new viruses have been assembled, they first need to travel inside the nucleus to the nuclear envelope to pass through it, followed by transport through the cytoplasm for egress through the plasma membrane.

Viruses can move passively by diffusion, but, being masters of exploiting the cellular machinery for their own needs, many viruses also use active transport machinery and motor proteins for their transportation. In addition, some viruses can generate forces required for their movement by forming so

called actin comet tails (Welch & Way 2013). These viruses, including many poxviruses and baculoviruses, use actin polymerization to increase their motility, resulting in more efficient transport over large distances. Even when moving passively, viruses can modify their environment to allow faster diffusion. Marginalization of chromatin to the nuclear periphery is an example of such a process. In the following, two examples that have a direct connection to the experimental part of this thesis are described: the diffusion of HSV-1 capsids in the cell nucleus, and the active actin-propelled movement of baculoviruses inside cells.

3.4.1 Diffusion of HSV-1 in cell nucleus

Herpes simplex virus 1 (HSV-1) is an enveloped, double-stranded DNA virus. After cell entry by envelope fusion with the plasma membrane, the capsid-tegument complex is released into the peripheral cytoplasm, from where it needs to travel to the nuclear envelope. Due to the size of the complex (capsid diameter ~ 125 nm (Schrag et al. 1989)) and the long distance involved, the virus uses dynein-mediated active transportation along microtubules (Sodeik, Ebersold & Helenius 1997, Lyman & Enquist 2009). Once at the nuclear envelope, the capsid docks at a nuclear pore complex and injects its genome into the nucleus, where the transcription and assembly of new capsids takes place.

To spread the infection, nascent viruses need to travel first out of the nucleus, and eventually out of the cell. After the capsids reach the nuclear envelope, they bud through the nuclear envelope in a process mediated by viral proteins UL31 and UL34 (Bigalke et al. 2014). Once in the cytoplasm, they move to the cellular periphery using the microtubule network. In the process they undergo their final maturation, during which the nucleocapsids become surrounded by the viral tegument proteins and lipid envelope (Mettenleiter, Klupp & Granzow 2006).

Until quite recently, it was not clear how the assembled HSV-1 capsids move in the cell nucleus. One of the earliest studies suggested that they move in an active manner, dependent on actin polymerization (Forest, Barnard & Baines 2005). However, more recent studies have found no evidence of active transport (Bosse et al. 2014, Bosse et al. 2015). In publication III of this thesis, using simulations in the chromatin geometry of infected cells, it was verified that passive diffusion is sufficient for effective transport to the nuclear envelope (Aho et al. 2017).

The HSV-1 capsid is relatively large (125 nm), making its motion in the nucleus is restricted by the chromatin network of the host cell. As mentioned above, particles of this size become trapped in interchromatin corrals, and their motion over longer distances becomes restricted. During herpesvirus infection many small replication compartments form, and when the infection proceeds, these compartments merge into one big compartment that fills most of the central parts of the nucleus, pushing the host chromatin to the edges of the nucleus (Randall & Dinwoodie 1986, Aho et al. 2017). This modification has been observed to increase the size of interchromatin spaces (Bosse et al. 2015) and result

in the formation of additional interchromatin channels (Myllys et al. 2016), leading to enhanced capsid mobility.

3.4.2 Active motion of baculovirus in cells

Baculoviruses are DNA viruses that infect invertebrates. Baculoviruses of nuclear polyhedron type have rod-shaped nucleocapsids, and these viruses utilize actin-mediated transport common with bacteria of many genera (Tilney & Portnoy 1989, Gouin et al. 1999). In this motion, actin fibers are polymerized from the rear surface of the virus capsid, causing a propulsive force that pushes the capsid forward in a more directed manner than would be possible by thermal motion (Ohkawa, Volkman & Welch 2010). In addition to baculoviruses, some other viruses, like vaccinia (Cudmore et al. 1995) and SV-40 (Pelkmans, Püntener & Helenius 2002), use actin polymerization to move. The exact mechanism for the force generation by actin polymerization is still under debate, although many models have been proposed (Dickinson & Purich 2002, Mogilner & Oster 2003, Plastino & Sykes 2005, Mueller et al. 2014).

The most commonly studied baculovirus is *Autographa californica* nuclear polyhedrosis virus (AcNPV), which is a baculovirus of the nuclear polyhedron type with a rod-shaped capsid of approximately 260 by 21 nm (Fraser 1986, Ihalainen et al. 2010). Actin polymerization requires quite a small number of components; the movement has been reproduced in vitro using plastic beads coated with actin polymerization activator N-WASP in a mixture of five purified proteins (Wiesner et al. 2003). The actin polymerization of AcNPV is promoted by a N-WASP-like protein p78/83 (Lanier & Volkman 1998, Machesky, Insall & Volkman 2001).

Some quantitative details of baculovirus motion have been resolved in previous studies. In the cell cytoplasm, the velocity of AcNPV capsids has been measured to be about 230 nm/s (Ohkawa, Volkman & Welch 2010). Another study conducted with plastic beads showed that the velocity of the beads was independent of their diameter and of the viscosity of the surrounding medium. The motion of baculovirus capsid seems to consist of straight motion and occasional changes of direction. The angular distribution of the turns (determined from the xy-projection of the motion) has been measured to be $22.0 \pm 24.4^\circ$ (mean \pm std).

The nucleus of the cell also contains actin that is typically in non-filamentous form (de Lanerolle & Serebryanny 2011, Kristó et al. 2016). Interestingly, it has been found that baculoviruses can promote filamentation on actin also in the nucleus (Charlton & Volkman 1991), and that baculovirus infection causes nuclear localization of cellular actin and its polymerization by p78/83 (Goley et al. 2006). One of the possible uses for this polymerization is the intranuclear propulsion of the capsids, which has been observed recently (Ohkawa & Welch 2016).

4 NUMERICAL MODELING OF PARTICLE MOTION IN CELLS

Due to the complexity of the cellular world, solutions of the mathematical models describing intracellular transport in a detailed manner are often not attainable by analytical means. However, the cellular environment and phenomena are so rich that, even when resorting to numerical methods, it is impossible to include every detail into the model. A remaining alternative is to pursue approximate model solutions using numerical or computational techniques.

In this chapter, an elementary information of modeling particle motion using lattice-Boltzmann and random walk methods is given first. After that, practical considerations that must be taken into account when constructing modeling environment for particle transport in realistic cellular environments are discussed.

4.1 The lattice-Boltzmann method

The lattice-Boltzmann method (Succi 2001) can be perceived as a discretized version of the Boltzmann equation for the probability density function f of a particle in a phase space. That is, the lattice-Boltzmann method (LBM) emerges from the kinetic theory of gases and can be characterized as a mesoscopic method. In the lattice-Boltzmann method a set of distribution functions, one for every prescribed direction of motion, are solved as a function of time at every lattice site. The method consists of alternating collision and streaming steps that emulate particles moving in space and colliding with each other. In the streaming step distribution functions of one site are moved to the neighboring lattice sites (Figure 5), and in the collision step the distribution functions are relaxed toward an equilibrium distribution f_i^{eq} (when the so-called BGK collision operator is used):

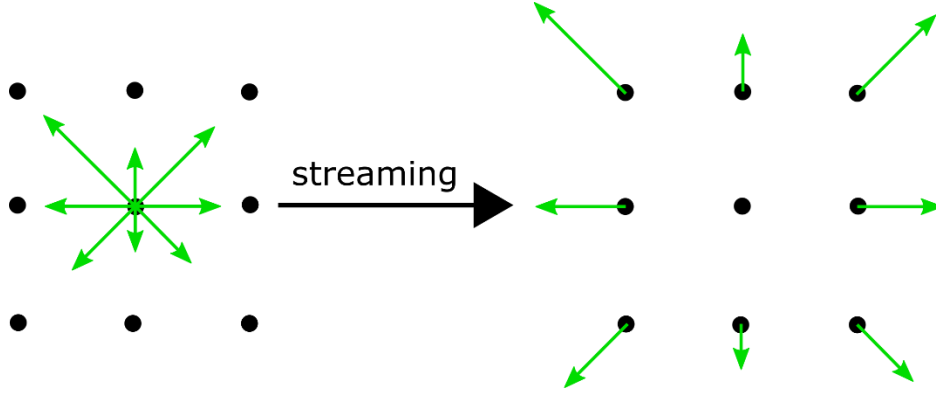


Figure 5. Illustration of streaming in the lattice-Boltzmann method: Lattice-Boltzmann distribution functions originating from a lattice site propagate to the neighboring sites.

$$f_i(\mathbf{r}, t) = f_i(\mathbf{r}, t) - \frac{f_i(\mathbf{r}, t) - f_i^{eq}(c)}{\tau^*} \quad (\text{collision})$$

$$f_i(\mathbf{r} + \delta r \mathbf{e}_i, t + \delta t) = f_i(\mathbf{r}, t) \quad (\text{streaming}). \quad (22)$$

In the above equation τ^* is the single, dimensionless relaxation time, and \mathbf{e}_i are the dimensionless lattice vectors connecting a lattice site to the neighboring sites; the index i covers all directions of motion involved (see below).

Three-dimensional diffusion can be modeled in the lattice-Boltzmann framework using the so-called D3Q7 model (three dimensions, seven distribution functions), where the distributions move in the direction of cartesian coordinate axes (the seventh distribution function is associated with the so-called rest or zero lattice vector). In this model, the equilibrium functions can be chosen as

$$f_i^{eq}(c) = c(1 - 3b) \quad \text{for } i = 0$$

$$f_i^{eq}(c) = cb/2 \quad \text{for } i \neq 0, \quad (23)$$

where the domain of the parameter b is $0 < b \leq \frac{1}{3}$. Concentration c of the transported substance is defined as the zeroth moment of the distribution function,

$$c = \sum_i f_i^{eq}, \quad (24)$$

and the diffusion coefficient is given by (Wolf-Gladrow 1995, Aho et al. 2016)

$$D = \left(\tau^* - \frac{1}{2} \right) \frac{b \delta r^2}{\delta t}. \quad (25)$$

Impermeable boundaries are particularly convenient to implement in the lattice-Boltzmann method using the bounce-back rule. As an example, if there is a boundary cutting the link between lattice sites \mathbf{r} and $\mathbf{r} + \delta r \mathbf{e}_i$, where \mathbf{r} belongs to the transport domain, the bounce-back rule can be written as

$$f_i(\mathbf{r}, t + \delta t) = f_{-i}(\mathbf{r}, t). \quad (26)$$

The above bounce-back rule and the regular streaming step can be combined such that only part of the distribution function is reflected back, and this partial bounce-back scheme can be used to model diffusion through a membrane (discussed in Section 6.1).

4.2 The random walk method

A random walker is an extremely useful model for many problems such as Brownian motion (Kac 1947), behavior of polymer chains and even stock markets (Fama 1965). Perhaps the simplest random walk consists of a particle moving a constant distance δr during time δt . If for every time step the particle moves a step length δr randomly forwards or backwards into each of the d dimensions, the diffusion coefficient is given by

$$D = \frac{(\delta r)^2}{2d \delta t}. \quad (27)$$

The step length does not need to be constant, and it can be drawn from a probability distribution. For example, by adopting a Gaussian step length, with zero mean and standard deviation σ_r , the diffusion coefficient is

$$D = \frac{\sigma_r^2}{2d \delta t}. \quad (28)$$

The time step can also be a (continuous) random variable, which means that the waiting time for a particle between jumps is selected from a probability distribution. These methods are called continuous-time random walks (Montroll & Weiss 1965). The waiting time for a regular diffusion needs to be exponentially distributed. One example of such a random walk is the time-domain random walk on a lattice (McCarthy 1993, Delay, Porel & Sardini 2002). In the time-domain random walk the jumping probability from lattice site i to lattice site j , p_{ij} , is proportional to the harmonic average of the effective diffusion coefficient of those two sites:

$$p_{ij} = \frac{b_{ij}}{\sum_j b_{ij}}. \quad (29)$$

In the above equation b_{ij} is given by

$$b_{ij} = \frac{S_{ij}}{L_{ij}} H(\varepsilon D)_{ij}, \quad (30)$$

where S_{ij} is the interface area separating the two lattice volumes V_i and V_j (defined for each lattice site such that the lattice sites are located at the center of the volumes), L_{ij} is the distance between the lattice sites, and $H(\varepsilon D)_{ij}$ is the harmonic mean of the product εD of the sites i and j (ε is the porosity). The waiting time between two jumps, $t_{n+1} - t_n$, can be selected by drawing a number u_{01} from the uniform distribution between 0 and 1, and setting the waiting time as

$$t_{n+1} - t_n = -\frac{\varepsilon V_i}{\sum_j b_{ij}} \log(u_{01}). \quad (31)$$

When modeling diffusion with a spatially varying diffusion coefficient, one has to be careful when using a spatially-varying step size to describe the process. In this case the simulations have a systematic error of particles accumulating to areas of lower diffusivity. This is due to particles having a higher probability to jump from a region with high diffusivity to the areas of low diffusivity than vice versa. There are, however, corrections to the random walker to circumvent the problem. In the corrections, the mean of the step distribution

is shifted away from zero by an amount proportional to the gradient of diffusion coefficient (Hunter, Craig & Phillips 1993), or particle jumping probabilities are adjusted such that the probability to jump in the direction of increasing diffusion coefficient is increased (Farnell & Gibson 2005).

In a regular random walk, the moving direction of the particle during a jump does not depend on the moving direction during the previous jump. Assume a motion where a particle moves in a straight line with occasional turns randomly to left or right by an angle $\delta\theta$. Then, depending on the turning angle, the direction of movement can become correlated. This type of motion is commonly called correlated random walk (Kareiva & Shigesada 1983). In a correlated random walk, the new direction of motion for a particle is not completely random, but the previous direction affects the next direction. The mean squared displacement after n steps of a particle exhibiting correlated random walk is given by

$$MSD = nE(l^2) + 2E(l)^2 \frac{c}{1-c} \left(n - \frac{1-c^n}{1-c} \right), \quad (32)$$

where E is the expectation value, l is the length of the straight segment and $c = E(\cos \delta\theta)$. Both the turning angle $\delta\theta$ and the segment length l can be selected from a probability distribution. The above equation has a long time (large n) limit,

$$MSD = n \left(E(l^2) + 2E(l)^2 \frac{E(\cos \delta\theta)}{1 - \cos \delta\theta} \right). \quad (33)$$

As in this limit the MSD is proportional to n , this means that in the long time limit the motion is diffusive. The correlated random walk has been used, for example, to model the motion of insects (Kareiva & Shigesada 1983) and mammals (Bergman, Schaefer & Luttich 2000).

4.3 Modeling in image-based geometries

4.3.1 Imaging three-dimensional structure of cells – confocal fluorescence microscopy and soft x-ray tomography

In fluorescence microscopy methods, a fluorescent sample is illuminated with a light of certain wavelength, and the sample emits light of longer wavelength, which makes it possible to separate the emitted light from the excitation light using fluorescence filters. Cellular components can be made to fluoresce by subjecting them to fluorescent molecules that specifically bind to these structures (Figure 6), or cells can be made to express a hybrid fluorescent protein, which consists of the protein of interest fused to a fluorescent marker protein. Expression of a hybrid fluorescent protein is achieved introducing to the cells a plasmid that replaces a sequence of cellular DNA by a modified sequence that contains instructions to make the protein in a fluorescent form. The ability to selectively label different components of cells has made fluorescence microscopy an

indispensable tool, and its contribution to the advances of biology cannot be overestimated.

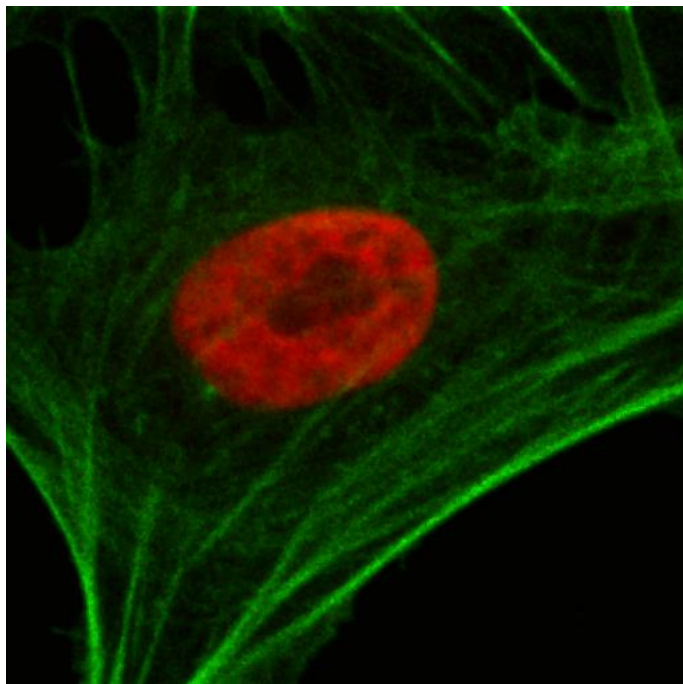


Figure 6. A HeLa cell that has its actin filaments and DNA stained using FITC phalloidin and DAPI.

In regular fluorescence microscopy, fluorescent light from the whole sample is detected, which is why the axial resolution is poor. Confocal fluorescence microscopy improves this by introducing a small pinhole in the path of emitted light. This pinhole prevents out-of-focus light from entering the detector. With confocal microscopy a typical resolution in the z-direction is about 1 μm , while the lateral resolution is about 200 nm. The sample can be moved so that the focus plane passes through the sample, which allows for gathering a three-dimensional image of the sample.

In soft x-ray tomography, x-rays are passed through the sample and the absorbance of the sample to the radiation is recorded. Like in the traditional transmitted-light microscopy, with one angular position of the sample it is only possible to get the accumulated absorbance through the whole sample. To obtain the three-dimensional structure of the sample, the sample is rotated and information from many angles is computationally combined. Due to the shorter wavelength, the resolution of a soft x-ray microscope (~ 30 nm) is higher than that of a light microscope. Living cells cannot be imaged, and cells must be cryofixed to reduce radiation damage to the sample (McDermott et al. 2009). The cells are, however, intact and hydrated.

As the name of the technique suggests, the x-rays used for the imaging are of relatively low energy. The energy is around 300-500 eV, because water does not absorb well at that range, whereas carbon absorbance is much higher. This gives good contrast in biological samples, where the non-absorbant watery background of the cells can be separated from the carbon-containing biomole-

cules. Soft x-ray microscopy can be used, for example, to analyze chromatin density in the nucleus (Le Gros et al. 2016). Up to now, soft x-ray microscopes have mostly been located at large facilities, where particle accelerators have been used to produce the x-rays needed for imaging. However, recent advances have made it possible to build laboratory-scale soft x-ray microscopes that use laser plasma sources (Fogelqvist et al. 2017).

4.3.2 Segmenting the cell and the nucleus

For a realistic transport simulation in cellular environment, the model must include those details of the environment that are crucial to the transport. To simulate, for example, permeation of a molecule across the nuclear envelope, the location of the nuclear envelope must be accurately determined. The same is true for volume diffusion in the cytoplasm or nucleus, where the boundaries of the cytoplasm or nucleus must be specified.

In fluorescence microscopy, there are many ways to obtain this type of structural information. The specificity of fluorescent stains makes it possible to selectively mark organelles and other cellular components. To separate the cell from its surroundings, the whole cell can be made fluorescently visible by transfecting the cell with a plasmid that encodes any non-binding fluorescent molecule that spreads throughout the cell and therefore shows the boundaries of it (Figure 7a). The most traditional way to separate the nucleus from the rest of the cell is to use a fluorescent molecule that binds to DNA, such as DAPI or Hoechst dyes. Alternatively, the cell can be transfected with a plasmid to make it express one of the histone proteins in a fluorescent form (Figure 7b). The DNA is separated from the nuclear envelope by the nuclear lamina. The thickness of the lamina is typically less than 80 nm (Gerace, Blum & Blobel 1978), which is much below the resolution of light microscopy. For this reason, DNA or histone staining is a good method for segmentation of nuclei. When the cell and its nucleus are made visible this way, segmentation of them from the rest of the image is easy to do, for example, by setting an intensity threshold manually or using an automatic algorithm (for example Otsu's method (Otsu 1979)) and interpreting pixels that are above this value belonging to the cell or nucleus, respectively (Figure 7c). Some nuclei contain nucleoli (shown as dark spots in Figure 7a and Figure 7b). They are dense structures that exclude many molecules and are weakly stained by DAPI and Hoechst dyes due to low chromatin concentration. For this reason, it is sometimes necessary to use a hole-filling algorithm after setting the threshold to segment the entire nucleus.

Electron microscopy and x-ray tomography (Figure 7d) lack the specificity that makes fluorescence microscopy such a powerful tool in cellular biology. They partially compensate this shortcoming by higher resolution. With these methods it is much more difficult to, for example, segment the nucleus from the rest of the cell.

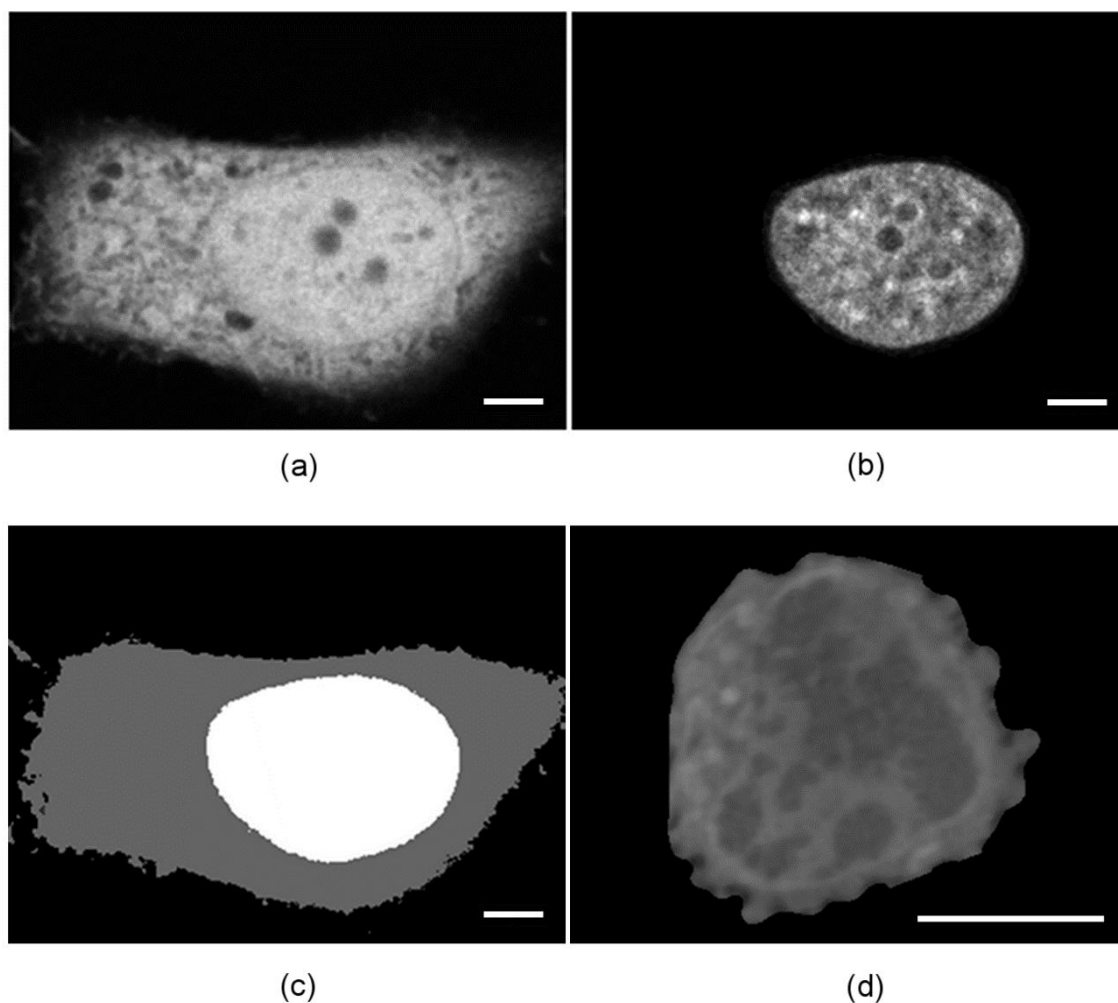


Figure 7. A confocal plane of a HeLa cell fluorescently labeled with (a) non-binding EYFP, showing the whole cell and (b) histone-binding H2B-ECFP showing the nuclear chromatin. (c) Segmentation of the cell and its nucleus by manually determined threshold values. (d) A single orthoslice of a soft x-ray tomography imaged mouse B cell. All the scale bars are 5 μm in length.

4.3.3 Obstructions to bulk diffusion and the problem of nonuniform equilibrium distribution

The equilibrium distribution of a population of fluorescent particles does not give information about their dynamics, unless fluctuations in the signal can be measured, as is done in fluorescence correlation spectroscopy (Magde, Elson & Webb 1972, Krichevsky & Bonnet 2002). The equilibrium can be disturbed by irreversibly photobleaching (destroying the fluorescence by illumination with high-intensity light) a part of the fluorescent signal in some region of the cell. The diffusion coefficient of the fluorescent molecule can then be determined by fitting a mathematical function to the recovering fluorescence intensity in that area. This method is called fluorescence recovery after photobleaching (FRAP) (Axelrod et al. 1976, Soumpasis 1983, Braga, Desterro & Carmo-Fonseca 2004). The method is quite accurate when the shape of the photobleached profile is simple and there are no obstructions to diffusion near the photobleached region.

Another way to extract transport coefficients from measurements is to simulate the evolution of fluorescence after photobleaching in the actual cell geometry, and to compare the simulation to a measured evolution of fluorescence (Kühn et al. 2011, Aho et al. 2016). As in FRAP, the equilibrium distribution of the fluorescent signal is disturbed, and changes in the fluorescence are recorded after this. These experimental changes can then be compared with the simulated changes and, for example, the diffusion coefficient and permeability of the nuclear envelope can be calculated from the simulation parameters that yield the best match between the simulation and experiment. There are two important issues that need to be considered when simulating the evolution of fluorescence in cells. Both of these issues concern the obstacles that the fluorescent molecules encounter in cells. The first one is the fact that the equilibrium distribution of even non-interacting proteins is nonuniform, like the one seen in Figure 7a. In the cytoplasm mitochondria and vesicles, for example, and in the nucleus chromatin and nucleoli exclude particles, which is why the signal of fluorescent molecules is lower at those locations. That is, although the real concentration of fluorescent molecules in the fluid phase can be the same at two locations, the concentration may appear to be different due to obstacles reducing the available space. This has to be taken into account in the simulations to maintain the nonuniformity of the distribution; the evolution of the fluorescent signal cannot be directly simulated, because the solution of the diffusion equation is a uniform distribution, which is obviously not true in a cell filled with obstacles. The second detail is that the cause of this nonuniformity, the obstacles and the restricted space available for the molecules, slows transport of the particles.

Both of the above problems can be addressed if the equilibrium fluorescence distribution, I_{eq} , of the molecule in the cell is known. The diffusion of the molecules can then be corrected in the simulation using the equilibrium distribution. One method to take the non-uniform equilibrium distribution into account is to use a diffusion-advection equation, where the advective term is proportional to the gradient of the equilibrium distribution (Kühn et al. 2011). This advective term acts to recover the part of particle flux that is due to apparent, not real, concentration differences caused by the difference in accessible volume for the fluorescent particles. Another possibility is to simulate the diffusion of intensity relative to the equilibrium intensity, $R(t) = I(t)/I_{eq}$, which also results in an equilibrium distribution as a long-time limit (Aho et al. 2016). Because the local fluorescence intensity of a non-binding fluorescent molecule reflects the space available for the fluorescent molecules at the position (the signal is higher in places where there are more fluorescent molecules), this data gives access to the relative diffusion coefficient in the form of the porosity approximation of Equation (21). That is, the diffusion coefficient can be scaled locally by equation

$$D(r) = D_{ref} \frac{I(r)}{I_{ref}}. \quad (34)$$

This requires that the value of the diffusion coefficient, D_{ref} , is known at some reference intensity I_{ref} , or that D_{ref} can be used as a fitting parameter (Kühn et al. 2011, Aho et al. 2016).

When diffusion to a region is not only partly restricted, but completely prevented, treatment of these impermeable regions depends on the numerical model used. In the lattice-Boltzmann method, impermeable borders can be handled using the bounce-back rule, which completely reflects a distribution function at the border. In random walks the jumps to those areas can be prevented, or if dealing with the time domain random walk, the diffusion coefficient of the impermeable regions can be set to zero, which makes the jump probability to those areas zero (since the jump probability is proportional to the harmonic average of the diffusion coefficients of the two sites). In particle-based methods, if the particle has non-zero dimensions, the motion to those areas where the particle would intersect impermeable material must be prevented. The intersection of spherical particles with the surrounding obstacles is relatively easy to check, especially if the obstacles themselves are spherical or cubical (or consists of them, as is the case in the experimental part of this work, where obstacles determined from microscopy images can be thought to consist of cubical voxels). This can be expanded to check the intersection of a rod-shaped object by modeling the rod as a series of spheres having their centers located on a line. By adjusting the distance between the spheres, the rod can be modeled with the desired precision.

4.3.4 Modeling diffusion through membranes

In numerical models with discrete space, diffusion through a membrane can be modeled explicitly by representing the membrane with grid nodes, or implicitly through a boundary condition between nodes. The membrane usually restricts diffusion, meaning that the simulation has to account for the reduced flux through the membrane. In explicit methods the membrane is represented by a surface of finite thickness, consisting of a series of lattice points. To restrict diffusion through the membrane, the local diffusion coefficient is reduced in those points, compared to the points outside the membrane (Kühn et al. 2011). However, the problem in this approach is that the real thickness of the membrane is not always known. And even if it was, the membranes are usually so thin that the simulation grid needs to be very dense at the membrane. In cells, for example, the thickness of the plasma membrane is less than 10 nm, and the thickness of the nuclear envelope is less than 100 nm. This is a small length scale compared to the size of the cell, which is usually tens of micrometers in diameter. To represent the whole cell with such a fine grid is often, due to computational constraints, impossible. Local grid refinement methods can sometimes be used, but these tend to be usually quite complex.

In an implicit method, the membrane can be represented as a boundary condition between two grid points. In a grid-based method, the particle concentration is only defined at grid points, whereas the equation for membrane permeability, Equation (15), gives the flux as a function of concentration difference at the opposite sides of the membrane. This equation can be modified to give the flux as a function of the concentration difference between two grid points on the opposite sides of the membrane. If there is a grid point on both sides of the membrane at a distance h from it, the flux through the membrane is given by

$$J_m = -\frac{l}{l+h} P \delta c, \quad (35)$$

where l is the so-called efficient thickness of the membrane, $l = \frac{D}{2P}$, and δc is the concentration difference between the two grid points on opposite sides of the membrane (Aho et al. 2016).

5 EXPERIMENTAL METHODS

In this chapter, the experimental methods used are described. The experimental part of this work consisted mainly of confocal fluorescence and soft x-ray microscopy, to yield three-dimensional structures of the cells, and computational methods to model particle motion in the cellular geometries extracted from the microscopy images.

5.1 Confocal fluorescence microscopy of living cells

To measure the nuclear envelope permeability for EYFP molecules, human carcinoma HeLa MZ cells, grown at 37°C temperature in Dulbecco's modified Eagle medium supplemented with 10% fetal bovine serum, were transfected with EYFP-N3 plasmid. To visualize the location of the nucleus and nuclear envelope, the cells were also simultaneously transfected with fluorescently labeled histone H2B-ECFP plasmid. The cells were imaged 24 hours after the transfection.

The fluorescence signal was imaged with an Olympus FV1000 laser-scanning confocal fluorescence microscope using a 60x water immersion objective (numerical aperture 1.2). During imaging, the stage heater of the microscope was kept at 37°C. Equilibrium distributions of EYFP and H2B-ECFP were first imaged by taking confocal cross-sections through the entire cells. The pixel size and the distance between the confocal planes was set to 150 nm, and typically the whole cell was contained in about 80 cross-sections. The image resolution was 320x240 pixels.

The dynamics of EYFP was imaged by photobleaching a circular area from the nucleus. The diameter of the area was 1.5 μm , and the bleaching was done using maximum power from the 514 nm laser. The evolution of fluorescence was recorded immediately after the photobleaching with 5.2-5.5 frames per second. Due to the fast diffusion of EYFP in the cell, the evolution was imaged in

one confocal layer and a smaller region of size 320x90 or 320x100 pixels to increase the acquisition speed.

5.2 Soft x-ray tomography of HSV-1- and baculovirus-infected cells

The immortalized mouse B cell line used for HSV-1 studies was Abelson murine virus transformed pre-B cell line of female mouse. Cells were maintained in a suspension culture at 37 °C in RPMI-1640 medium, supplemented with 10% or 15% of fetal bovine serum (FBS) (GIBCO, Invitrogen, Inc.), L-glutamine, penicillin, streptomycin and 5% CO₂. The HSV-1 strain was expressing EYFP-ICP4 and the viruses were isolated as previously described (Everett, Sourvinos & Orr 2003). The cells were infected by inoculating them with HSV-1 or HSV-1 EYFP-ICP4 at a multiplicity of infection of 5–10. After this the cells were kept at 37 °C until live-cell microscopy, fixation, and soft x-ray tomography analysis.

For studies with baculovirus-infected cells, Sf9 insect cells derived from *Spodoptera frugiperda* were maintained as suspension cultures in a non-humidified shaking incubator at 26–28°C in Grace's insect media supplemented with 10% fetal bovine serum FBS and 1% Pluronic F-68. Autographa californica multiple nucleopolyhedrovirus virus, with protein VP39 fused at its C terminus with three copies of monomeric red fluorescent protein mCherry, was used for infections.

The cells were infected 24 hours prior to imaging, for which the cells were transferred into glass capillaries and frozen. During the imaging the capillaries were kept frozen in a stream of liquid nitrogen-cooled helium gas. The imaging was done using the XM-2 soft x-ray microscope at the Lawrence Berkeley National Laboratory. Each cell was imaged by increasing the sample rotation by 1–2° between projection images, resulting in 90–180 projection images per cell. Exposure time was between 300–400 ms. Iterative reconstruction methods were used to reconstruct the 3D structure from the projections. The voxel size of the images was 32 nm.

5.3 Lattice-Boltzmann simulation of nuclear envelope permeation by EYFP

The cells were segmented using the EYFP signal which was, due to the small size of the molecule, located both in the cytoplasm and nucleus. The nucleus of the cell was segmented using the H2B-ECFP signal. Both the segmentations were performed using a manually determined threshold. The initial distribution for the simulation was set by first calculating the ratio of the EYFP intensity after the photobleaching to the equilibrium intensity, $\gamma(x, y, t = 0) = I(x, y, t =$

$0)/I_{eq}(x, y)$, in the one confocal plane where the photobleaching experiment was conducted. The 3D distribution for the simulation was then obtained by assuming that the photobleached profile was constant in z -direction (Kühn et al. 2011), and the distribution after the photobleaching was thus given by

$$I(x, y, z, t = 0) = \gamma(x, y)I_{eq}(x, y, z).$$

Diffusion of EYFP was simulated in the reconstruction of HeLa cells with a D3Q7 model of the lattice-Boltzmann method, and the simulation grid size was set to the same value as the pixel size in the microscopy images (150 nm). Each of the velocity distributions was then given the value $I^*/7$, where $I^* = I(t = 0)/I_{eq}$. The ratio to the equilibrium was chosen, instead of directly simulating the evolution of the distribution I , because that way the heterogenous equilibrium distribution, which is due to obstacles in the cell preventing motion to certain regions, could be maintained during the simulation (see Section 4.3.3). In the simulations, the full bounce-back rule was implemented at the borders of the cell and a partial-bounceback rule was implemented between the grid points of the nucleus and cytoplasm. During the simulation, images of the simulated distribution in one confocal plane were saved at constant time intervals for later comparison with the experimental distribution. After the simulation, the saved evolution of I^* was converted back to the intensity values $I(t)$, for comparison with the measured intensity changes in the experiment, by multiplying with the value I_{eq} . The comparison between the experimental and simulated intensities was done by calculating the Pearson correlation coefficient between them.

5.4 Random walk simulation of HSV-1 capsids in the nucleus

The motion of HSV-1 capsids in the reconstructions of HSV-1-infected nuclei was simulated using the time domain random walk method (Delay, Porel & Sardini 2002, Bortz, Kalos & Lebowitz 1975, McCarthy 1993), where the waiting times between jumps are exponentially distributed, and the jumping probability between two sites is proportional to the harmonic average of the diffusion coefficients of the sites (see Section 4.2). The particles were moved in the geometry defined by the soft x-ray images of infected mouse B cells, and the step size was set to 8 nm by dividing the 32 nm voxels of the microscopy images into four lattice points in each cartesian direction. For each step, the new candidate location after the jump was compared with the microscopy image of the chromatin density. If the particle was within 62.5 nm (the radius of a HSV-1 capsid) from a location that had its density above the density limit, the jump was not allowed. The density limit for the capsid motion was obtained by segmenting the nucleus into two regions based on the minimum between the two populations in the density histogram. 30,000 particles were randomly placed in the allowed regions of the nucleus at the beginning of the simulation, and the motion of a capsid was simulated for the total time of 4 h or until it reached the

nuclear envelope. The arrival times of the particles to the nuclear envelope were recorded, and distinct export locations were calculated based on groups of continuous pixels.

5.5 Correlated random walk simulation of baculovirus capsids in the nucleus

The motion of baculovirus capsids was simulated using a correlated random walk method. In this model the particle repetitively moves a distance L on a straight line, followed by a random turn (in a 2D motion either to left or right) by an angle $\delta\theta$ (Kareiva & Shigesada 1983). Three-dimensional motion was obtained by taking two turning angles, one in the xy -plane and another orthogonal to it. The angle distribution was assumed to be Gaussian, and the mean \pm the standard deviation was $22 \pm 24^\circ$ (Mueller et al. 2014). The length distribution of the straight segments was assumed Poissonian, and the mean of the distribution (350 nm) was selected by comparing the simulated straightness of the virus paths to an experimental value (Ohkawa, Volkman & Welch 2010). The length of the virus was 260 nm, and the width was 21 nm (Fraser 1986, Ihalainen et al. 2010), which was implemented in the simulations by modeling the capsid as a segment of 21 spheres that had the capsid width (21 nm) as their diameter. The distance between the centers of the spheres was thus about 11.4 nm. The density limit for the capsid movement was determined by segmentation of the LAC-values of the nucleus to two populations by the Gaussian mixture model (Farnoosh, Yari & Zarpak 2008) and allowing the capsids to move in the low-density regions.

In every simulation, 20,000 capsids were first placed randomly in the allowed locations of the nucleus. This was done by selecting a random location for the center of the capsid and two random angles for the capsid orientation. Then it was checked if the capsid intersected with impermeable material. If it did, a new position and new angles were randomly chosen. When a suitable location and orientation was found, a segment length L was selected from the probability distribution and the capsid was moved forward in increments of 7 nm (0.2 pixels in the microscopy images). For every step it was checked that the capsid did not hit an impermeable region. When the capsid hit an obstacle or moved the full length L , the motion was stopped and two turning angles were selected ($\delta\theta$ in the xy -plane and $\delta\varphi$ defining the change in z -coordinate). The capsid was turned to the new orientation in steps such that the increment was 1 degree for the largest of the above angles and $\min\{\delta\theta/\delta\varphi, \delta\varphi/\delta\theta\}$ for the other. In this way, both the turning angles could be covered in an equal number of steps. The turning was performed simultaneously for both angles, and during every turning step, the possible intersection of the capsid with impermeable material was checked. If the capsid was to collide with impermeable material during the turning, the turning was stopped. The turning was performed

around the geometric center of the capsid, and the turning rate was adjusted such that the linear velocity of the capsid rear during turning was the same as the capsid velocity in the straight translational motion. The total time of the simulation was selected such that setting the time longer than that did not increase the number of particles arriving to the nuclear envelope.

6 RESULTS OF MODELING BIOMOLECULE TRANSPORT IN CELLS

6.1 Determination of nuclear envelope permeability to fluorescent molecules

To improve previous fluorescence photobleaching-based methods to measure the permeability of the nuclear envelope (Peters 1983), a new method that aims to take more accurately into account the actual cellular geometry was developed. In the existing methods part of the fluorescent signal in the nucleus is destroyed by photobleaching, and the recovering intensity is then recorded as a function of time (Peters 1983, Wei et al. 2003). This method assumes that the diffusion through the nuclear envelope is slow so that the concentrations in the nucleus and cytoplasm are uniform, and that the volume of the cytoplasm is much larger than the volume of the nucleus so that the concentration in the cytoplasm is constant in time. Under these conditions, Equation (19) can be utilized for the determination of the nuclear envelope permeability.

The method presented here is based on measuring the evolution of the fluorescent molecule distribution and comparing that with simulations of molecule transport in the reconstructed geometry of the same cell. In this study, the permeability of the nuclear envelope was determined to enhanced yellow fluorescent protein (EYFP), a protein of 27 kDa mass that is known to be able to pass through the nuclear envelope passively. The diffusion of EYFP was simulated using the lattice-Boltzmann method and, to avoid representing the thin nuclear envelope with lattice points, a partial-bounce-back method was implemented between the nucleus and cytoplasm to control the flux through the nuclear envelope. In the partial bounce-back method the regular bounce-back method (see Section 4.1) can be modified such that only part of the distribution function is reflected back, allowing the rest to pass through the surface (Figure 8). This can be represented mathematically as

$$f_i(\mathbf{r} + \delta r \mathbf{e}_i, t + \delta t) = \phi f_i(\mathbf{r}, t) + (1 - \phi) f_{-i}(\mathbf{r} + \delta r \mathbf{e}_i, t). \quad (36)$$

Partial bounce-back models have been used before, for example, to model transport in porous media (Dardis & McCloskey 1998) and heat conduction between two materials (Han, Feng & Owen 2008).

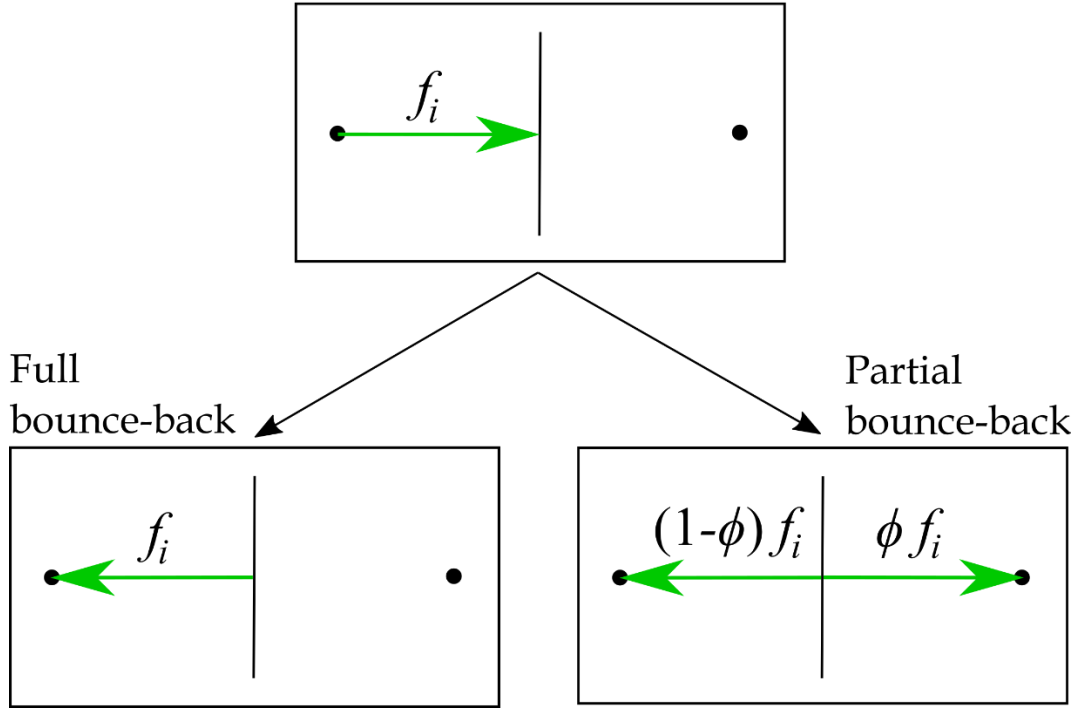


Figure 8. A full and a partial bounce-back rule in the lattice-Boltzmann method. When a distribution function arrives at a boundary (top part of figure), it can be reflected back in a full bounce-back scheme (lower left) or partially reflected in a partial bounce-back scheme (lower right). The ratio of the transmitted part to the whole distribution function is ϕ .

For the partial bounce-back treatment of the membrane it was derived that when the ratio ϕ of a distribution function is allowed to pass through a membrane (see Figure 8), the permeability of the membrane is given by

$$P = \frac{\phi}{1 - \phi} \frac{b \delta x}{2 \delta t}. \quad (37)$$

The parameters of the above equation are described in Section 4.1. The above equation for permeability was verified against an analytical solution in a steady-state case, and a semi-analytical (infinite series) solution in a transient case. In both cases the lattice-Boltzmann scheme showed excellent agreement with the analytical solutions.

To get realistic simulation geometries for simulations of intracellular transport, HeLa cells expressing enhanced yellow fluorescent protein (EYFP) were imaged using confocal fluorescence microscopy, and 3D models of the cells were constructed using the microscopy data (Figure 9(a)-(d)). The equilibrium fluorescence distribution of EYFP was used to scale the local diffusion coefficients according to equation (21). The equilibrium fluorescence distribution was disturbed by photobleaching a cylindrical region through the nucleus, and the evolution of fluorescence was observed in one confocal plane of the cell (Figure 9e, see also Figure 10a).

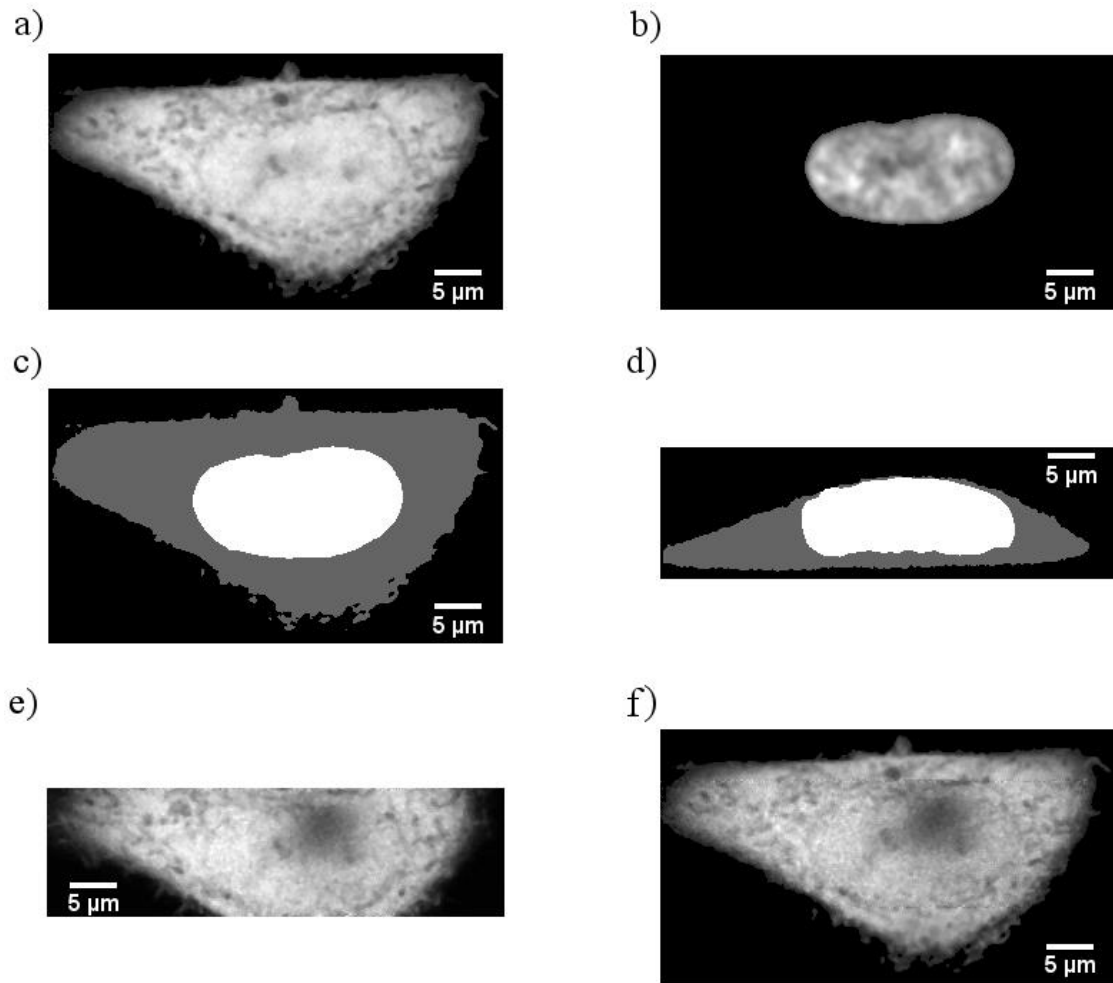


Figure 9. Construction of the simulation geometry and initial condition from the confocal fluorescence microscopy data. a) Equilibrium fluorescence distribution of EYFP in one confocal plane. b) Equilibrium fluorescence distribution of H2B-ECFP in one confocal plane. c) A top view of constructed simulation geometry, consisting of cytoplasm (grey) and nucleus (white). d) A side view of the simulation geometry. e) Fluorescence distribution of EYFP immediately after the photobleaching. f) The initial condition of the simulation, calculated using distributions of Fig. 2a and Fig. 2e. Figure taken from (Aho et al. 2016).

The fluorescence distribution right after the photobleaching was taken as the initial condition of the simulation, and the fluorescence evolution in the cell was simulated with different nuclear envelope permeability values until the most linear correspondence between the simulation and the experiment was found (Figure 10). The time step of the simulation was calculated from the slope of the best (the most linear) fit between the simulation and the experiment.

When the time step of the simulation and the value of ϕ that gave the most linear correspondence between the simulation and experiment were known, the diffusion coefficients in the cell and the membrane permeability for EYFP could be calculated using Equations (25) and (37). The analysis was done for 12 cells.

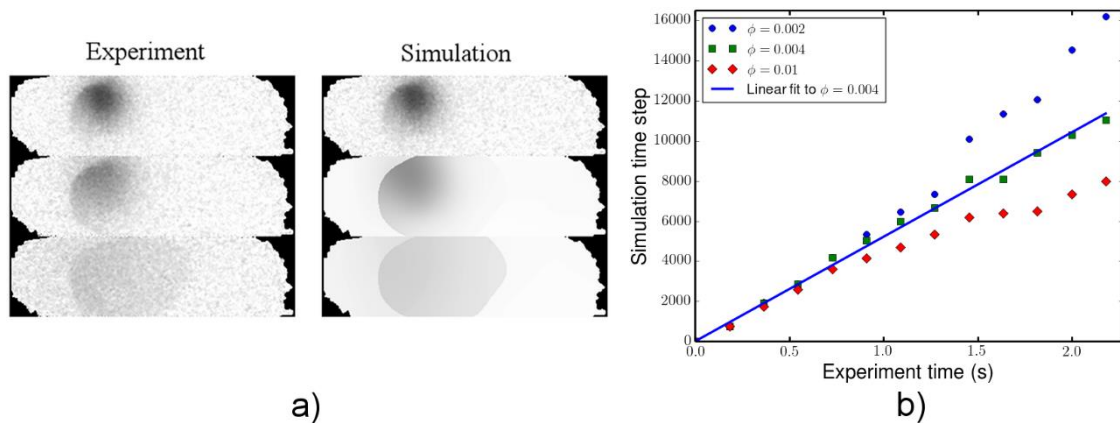


Figure 10. a) Comparison of fluorescence distribution in a cell, relative to the equilibrium distribution, at three timepoints in an experiment and a simulation. b) Simulation time points with highest cross correlation with the experimental data as a function of time, determined for three values of nuclear envelope permeability. Figure taken from (Aho et al. 2016).

The mean \pm standard deviation of the nuclear envelope permeability values was $0.5 \pm 0.3 \mu\text{m/s}$. The value is somewhat higher than what has been previously measured for a similar molecule, enhanced green fluorescent protein (Wei et al. 2003). That study was conducted in COS7 cells, and a nuclear envelope permeability of $0.011 \mu\text{m/s}$ was obtained. Some of the discrepancy can probably be explained by the different cell line. The method used for COS7 cells also underestimates the permeability, because of the assumptions that the concentration is uniform in the nucleus and cytoplasm and that the cytoplasmic concentration stays constant. Both of these assumptions are especially problematic at the top and bottom sides of the nuclear envelope of adherent cells, where the space between the nuclear envelope and the plasma membrane is restricted and the molecules transported through the nuclear envelope are not easily replaced (see Figure 9d).

The mean diffusion coefficient in the nucleus, obtained in our study, was $27 \pm 7 \mu\text{m}^2/\text{s}$, which is in good agreement with previous studies (Braga, Desterro & Carmo-Fonseca 2004, Potma et al. 2001, Kühn et al. 2011).

6.2 Diffusion of HSV-1 capsids in the nucleus

The emergence of the viral replication compartments in the nuclei of HSV-1-infected cells modifies the organization of the host chromatin. To study how HSV-1 capsids are able to diffuse in the chromatin geometry of infected nuclei, infected and non-infected mouse B cells were imaged, chosen because of their small size, using soft x-ray microscopy. These high-resolution images were then reconstructed into a 3D environment for simulations of capsid transport in the nucleus.

Analysis of the soft x-ray images showed that the average volume of the cell nuclei increased significantly during the infection; the total volume of the nucleus increased from $170 \mu\text{m}^3$ to $260 \mu\text{m}^3$. It was further found that low-density regions of chromatin formed channels in the nucleus, and the area density of these channels increased substantially in the viral infection. In the infected nuclei the amount of low-density chromatin was much higher next to the nuclear envelope, compared to the non-infected cells (24.7% in the infected versus 7.5% in the non-infected).

Based on the observation that HSV-1 capsids move in the interchromatin regions and avoid chromatin, the nucleus was divided into two areas, based on the linear absorption coefficient values of the soft x-ray micrographs. The motion of the capsids was restricted to the low-density regions, and their motion was simulated with a time-domain random walk method (Delay, Porel & Sardini 2002, Bortz, Kalos & Lebowitz 1975, McCarthy 1993). The diameter of the simulated particles was 125 nm, meaning that if the center of the particle tried to travel closer than 62.5 nm to an impermeable region, the jump was not allowed. The diffusion coefficient of the particles was $2 \times 10^{-2} \mu\text{m}^2/\text{s}$ (Bosse et al. 2015), and the diffusion of the chromatin network was not taken into account.

The transport of capsids was simulated in both the infected (Figure 11a) and non-infected chromatin geometries to see the effects of infection to the capsid transport. When the median transport time to the nuclear envelope was measured, it was noted that there were large differences between cells (Figure 11b), but the transport times were more consistent in the infected cells than in the non-infected cells. Transport time in some of the non-infected cells was very long, and one cell did not allow transport to the nuclear envelope at all. This suggests that the infection-induced changes to the chromatin geometry might facilitate capsid egress.

In the infected cells the transport time was 9 ± 2 minutes (mean \pm the standard error of the mean). The chromatin geometry of the infected cells was such that it eventually allowed the transport of almost all the capsids (99.9%) to the nuclear envelope. These findings suggest that there are channels at a given moment during the infection to allow capsid passage through the chromatin, and that chromatin motion is not necessary for this passage. Furthermore, passive motion seems adequate for capsid transport, which supports the recent findings that the capsids move by diffusion (Bosse et al. 2014, Bosse et al. 2015).

Although the chromatin geometry allowed the passage of capsids to the nuclear envelope, the chromatin structure of the infected cells was found to restrict the motion of capsids to the nuclear envelope strongly. When the chromatin density limit to the motion was removed, the transport time to the nuclear envelope decreased to 15 seconds, which shows that the effect of chromatin structure in the nucleus to the capsid transport is dramatic.

The locations where the capsids could reach the nuclear envelope were studied next (Figure 11c). It was found that approximately the same percentage (2%) of the nuclear envelope area was accessible to the capsids, but that the

number of distinct locations was much higher in the infected cells (150 ± 20 in infected versus 37 ± 17 in the non-infected cells).

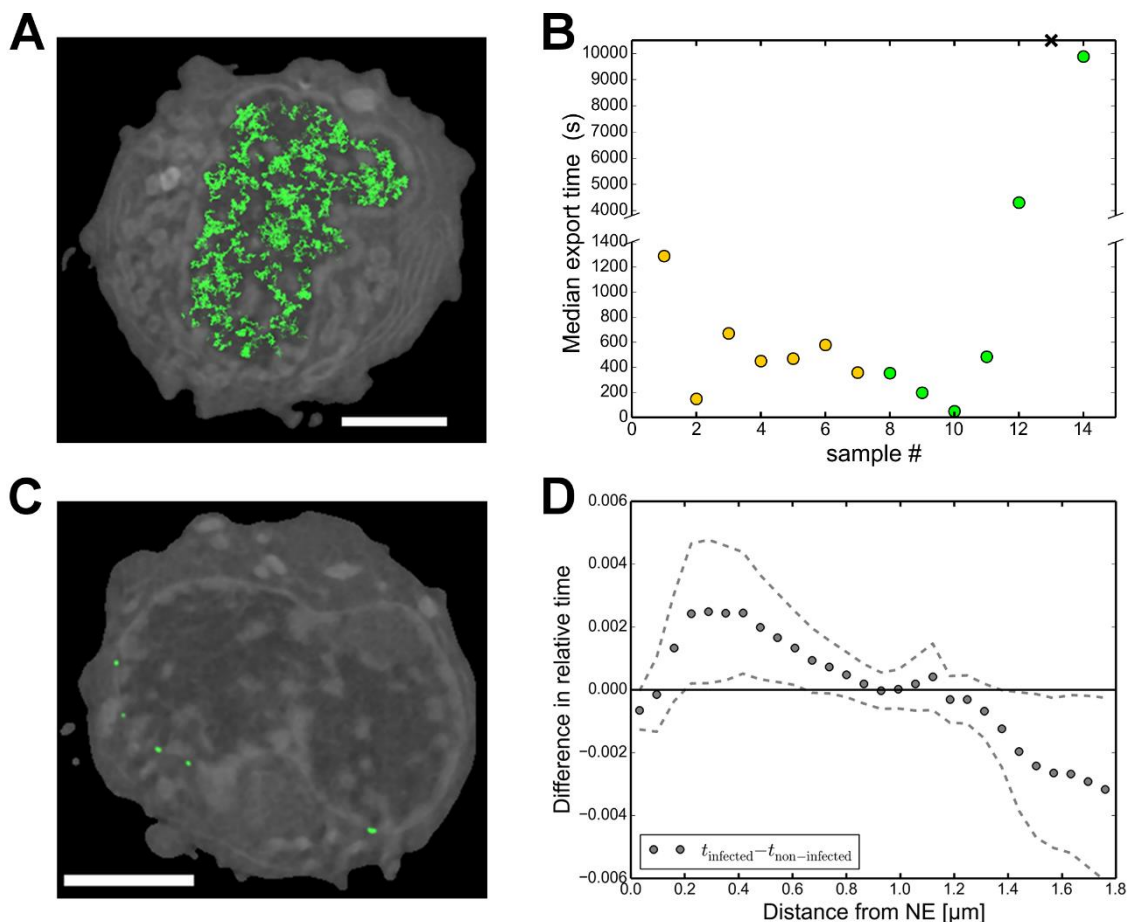


Figure 11. (a) Paths of capsids near one orthoslice of a soft x-ray tomography reconstruction. (b) Median transport time of capsids to the nuclear envelope simulated in the reconstructions of infected (yellow dots) and noninfected (green dots) cells. (c) Export locations (locations where capsids reached the nuclear envelope) marked using green color. The higher grayscale value of the background shows higher linear absorption coefficient and chromatin density at a location. (d) The difference between the simulations in the infected and noninfected chromatin geometries of the time spent by the capsids at various distances from the nuclear envelope. Figure taken from (Aho et al. 2017).

Finally, the amount of time the capsids spent inside the nucleus as a function of the distance from the nuclear envelope was calculated. It was found that in the infected cells capsids spent a larger fraction of the total time near the nuclear periphery than in the non-infected cells (Figure 11d). The reason for this behavior might be that the capsids at these locations were already inside the peripheral chromatin in the control cell geometries, whereas in the infected cell geometries the capsids were at that distance still trying to find paths through the chromatin that was displaced more toward the edge of the nucleus. Consistently, analysis of the chromatin distribution showed that heterochromatin was located closer to the nuclear envelope in infected cells than in non-infected cells. In the non-infected cells, the capsids spent more time in the central parts of the

nucleus, which can be explained by the more central distribution of chromatin, which restricted the motion away from there.

6.3 Active motion of baculovirus capsids in the nucleus

To study the motility of baculovirus capsids in the cell nucleus, the motion of capsid-sized particles was simulated in a soft x-ray tomography reconstruction of a cell infected with AcNPV baculovirus 24 hours prior to measurements (Figure 12a).

The nucleus was segmented into low- and high-density chromatin areas using Gaussian mixture modeling segmentation (Figure 12b). The amount of chromatin as a function of the distance from the nuclear envelope was analyzed, and it was found that the concentration of chromatin was highest at the vicinity of the nuclear envelope (Figure 12c). This is consistent with previous confocal microscopy studies in which marginalization of chromatin during baculovirus infection was also observed (Nagamine et al. 2008).

The motion of baculovirus capsids in the nucleus was simulated using the correlated random walk model (Figure 13a), and the simulation parameters were obtained from studies of baculovirus capsid motion in the cytoplasm. The motion of the capsids in the simulations was such that they moved straight with constant velocity of 230 nm/s (Ohkawa, Volkman & Welch 2010), and turned occasionally either left or right (and simultaneously either up or down). Both the turning angles were drawn from a Gaussian distribution with the mean \pm the standard deviation of $22 \pm 24^\circ$ (Mueller et al. 2014). This simple approach with two turning angles was selected to connect more easily the measured 2D projections of the turning angles from the above study to the simulation parameters in this study. The lengths of the straight segments were assumed to be Poissonian distributed, and the mean of the distribution (350 nm) was obtained by comparing the straightness of the capsid paths to an experimental value (Ohkawa, Volkman & Welch 2010).

The capsids were allowed to move in the low-density regions, and they were forced to stop and turn their direction if they collided with a high-density region. The simulations showed that only about 25% of the particles were able to travel to the nuclear envelope of the cell. The analysis of the particles that were not able to travel to the nuclear envelope showed that they were retained at the marginalized chromatin layer near the nuclear envelope (Figure 13b). Further live-cell studies are needed to determine if the invaginations seen at the edge of the marginalized chromatin actually contain capsids, and whether they open up later, allowing capsid access to the nuclear envelope. These findings suggest that the trapping of capsids near the nuclear envelope might be important regarding the eventual release of the capsids from the nucleus.

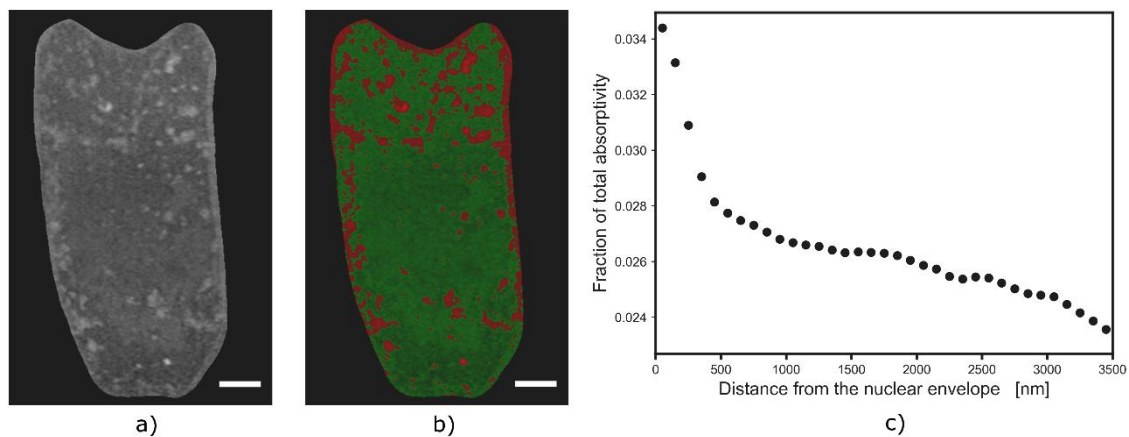


Figure 12. a) An orthoslice of a soft x-ray tomography data of a baculovirus-infected Sf9 cell. b) Segmentation of the nucleus to the low density (green) and high-density (red) chromatin regions. c) Nuclear localization of high-density chromatin as a function of the distance from the nuclear envelope. The length of the scale bars is 2 μm .

To study whether the observed turning angle of the capsid is optimal for transport in the nucleus to the nuclear envelope, the mean travel time of particles with various turning angles was calculated (Figure 13c). The standard deviation of the distribution was kept constant at 24 degrees while the mean was changed. At higher turning angles the nucleocapsid travel times were clearly increased. These studies revealed that the transport was fastest with the lowest angles, which suggests that the experimentally observed mean turning angle (22°) of the capsid turns in the cytoplasm might not be optimal in the chromatin network of the nucleus. In the model used for capsid transport here, there are two processes that affect the export times: the free motion and the collisions. It is intuitive that, since the apparent diffusion coefficient of the correlated random walk is higher for a smaller turning angle (Kareiva & Shigesada 1983), the smallest turning angle will yield fastest transport to the nuclear envelope in the absence or with a small number of obstacles. If the number of obstacles is high, on the other hand, then the particles can become stuck to the obstacles for a long period of time if the turning angle is small. This leads to further questions of whether the capsid motion is optimized for the cytoplasmic transport from the plasma membrane to the nucleus, is the movement reoptimized for nucleoplasmic transport, and what is the physical process behind the turns of the motion.

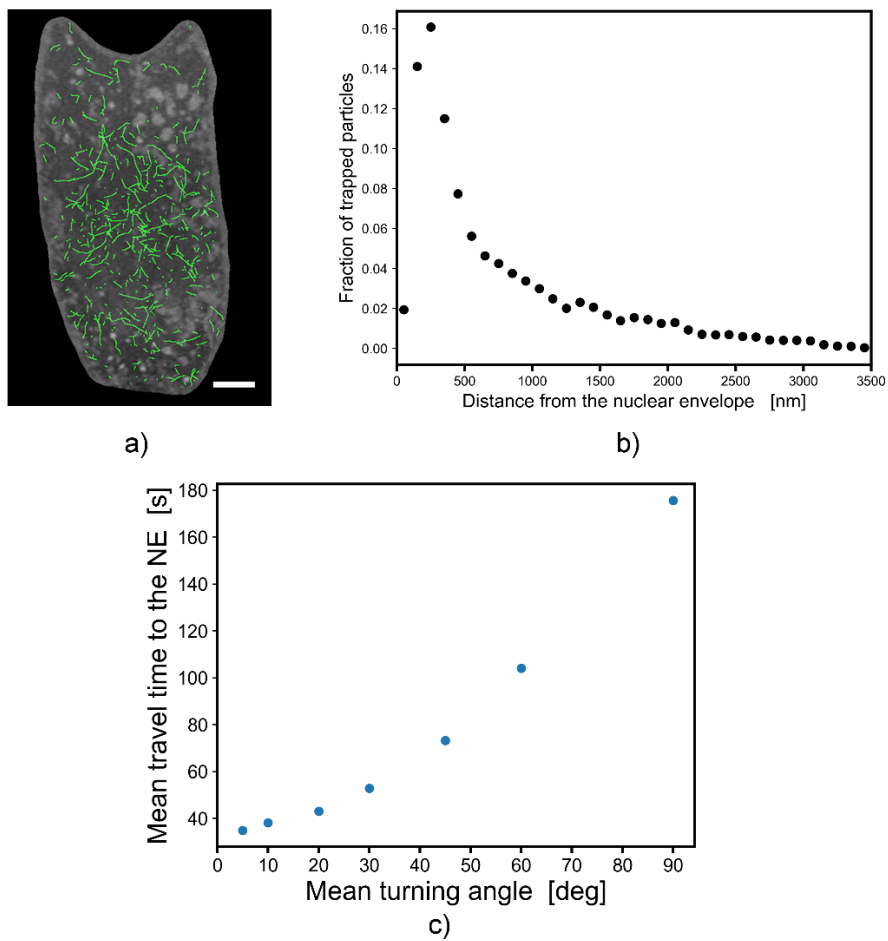


Figure 13. a) Paths of capsids during a simulation, recorded in a 350 nm thick slice (10 orthoslices) of the cell. The background shown is the maximum intensity projection of the soft x-ray orthoslices. b) The location of trapped particles in the simulation as a function of the distance from the nuclear envelope. c) The mean travel time of the particles as a function of mean turning angle of the capsids in the simulation.

7 SUMMARY

This work consists of studies that were conducted to include cellular structures in numerical simulations, in order to yield a more realistic picture of intracellular transport phenomena. Although the cellular environment is very complex, many structural details can be revealed by microscopy and utilized to create 3D-reconstructions for computer simulations of intracellular motion.

In the study of modeling nuclear envelope permeability, principles were derived for modeling diffusion through thin membranes in grid-based methods, and a new partial-bounceback scheme for the lattice-Boltzmann method was devised to model restricted diffusion between two lattice points. The parameters of the scheme were related to the permeability of the membrane, and the scheme was verified against analytical solutions. The developed lattice-Boltzmann scheme was used to determine the permeability of the nuclear envelope and the mean diffusion coefficient in the nucleus for enhanced yellow fluorescent protein by a method that consists of comparing the evolution of fluorescence in a simulation to the evolution in an experiment. The method can be extended for studying transport of any fluorescent molecule.

Microscopy methods also allow us to see the altered chromatin distribution in the virus-infected cells. High-resolution 3D-images of chromatin distribution in the nucleus of herpes- and baculovirus-infected cells were obtained using soft x-ray tomography. In cells infected with HSV-1, it was found that the virus infection increased the number of interchromatin channels that can facilitate capsid diffusion to the nuclear envelope. In both the HSV-1- and baculovirus-infected cells, we found that the virus infection marginalized host cell chromatin to the periphery of the nucleus. The effects of these changes to the diffusive transport of herpesvirus and active transport of baculovirus were studied by simulating the motion of those viruses in the chromatin environment reconstructed from soft x-ray tomography images. It was found that practically all the HSV-1-capsids were able to travel to the nuclear envelope in a reasonable time, which further verifies the recent findings that the nuclear transport of HSV-1 is passive in nature. The propulsive motion of the baculovi-

ruses led them to accumulate at the border of the marginalized chromatin, and only 25% of the capsids reached the nuclear envelope.

Computer simulations can answer some questions that experiments cannot. The effect of obstacles can be removed, or the transport of viral particles can be simulated in the chromatin geometry of infected and non-infected cells, which allows us to see the effect infection has on the transport. The properties of motion can be changed for particles, such as baculoviruses moving actively inside cells, to see if the observed motion is optimized for the transport. However, computer simulations depend on experimental data both to provide input parameters, and for comparisons with the simulation results, for example to determine fitting parameters of the simulation, or to eventually verify the results of a simulation. Computer simulations can also guide experimental research to a particular direction if interesting phenomena are detected.

REFERENCES

- Aho, V., Mattila, K., Kühn, T., Kekäläinen, P., Pulkkinen, O., Brondani Minussi, R., Vihinen-Ranta, M. & Timonen, J. 2016. Diffusion through thin membranes: Modeling across scales. *Physical Review E* 93, 043309.
- Aho, V., Myllys, M., Ruokolainen, V., Hakanen, S., Mäntylä, E., Virtanen, J., Hukkanen, V., Kühn, T., Timonen, J., Mattila, K., Larabell, C. A. & Vihinen-Ranta, M. 2017. Chromatin organization regulates viral egress dynamics. *Scientific Reports* 7:3692.
- Alber, F., Dokudovskaya, S., Veenhoff, L. M., Zhang, W., Kipper, J., Devos, D., Suprpto, A., Karni-Schmidt, O., Williams, R., Chait, B. T., Sali, A. & Rout, M. P. 2007. The molecular architecture of the nuclear pore complex. *Nature* 450, 695-701.
- Ariel, G., Rabani, A., Benisty, S., Partridge, J. D., Harshey, R. M. & Be'er, A. 2015. Swarming bacteria migrate by Lévy Walk. *Nature Communications* 6, 8396.
- Axelrod, D., Koppel, D. E., Schlessinger, J., Elson, E. & Webb, W. 1976. Mobility measurement by analysis of fluorescence photobleaching recovery kinetics. *Biophysical Journal* 16 (9), 1055-1069.
- Bergman, C. M., Schaefer, J. A. & Luttich, S. N. 2000. Caribou movement as a correlated random walk. *Oecologia* 123 (3), 364-374.
- Bigalke, J. M., Heuser, T., Nicastro, D. & Heldwein, E. E. 2014. Membrane deformation and scission by the HSV-1 nuclear egress complex. *Nature Communications* 5, 4131.
- Bortz, A. B., Kalos, M. H. & Lebowitz, J. L. 1975. A new algorithm for Monte Carlo simulation of Ising spin systems. *Journal of Computational Physics* 17 (1), 10-18.
- Bosse, J. B., Hogue, I. B., Feric, M., Thiberge, S. Y., Sodeik, B., Brangwynne, C. P. & Enquist, L. W. 2015. Remodeling nuclear architecture allows efficient transport of herpesvirus capsids by diffusion. *PNAS* 112 (42), E5725-E5733.
- Bosse, J. B., Viriding, S., Thiberge, S. Y., Scherer, J., Wodrich, H., Ruzsics, Z., Koszinowski, U. H. & Enquist, L. W. 2014. Nuclear herpesvirus capsid motility is not dependent on F-actin. *mBio* 5 (5), e01909-14.
- Braga, J., Desterro, J. M. & Carmo-Fonseca, M. 2004. Intracellular macromolecular mobility measured by fluorescence recovery after photobleaching with

- confocal laser scanning microscopes. *Molecular Biology of the Cell* 15 (10), 1749-1760.
- Bronstein, I., Israel, Y., Kepten, E., Mai, S., Shav-Tal, Y., Barkai, E. & Garini, Y. 2009. Transient anomalous diffusion of telomeres in the nucleus of mammalian cells. *Physical Review Letters* 103 (1), 018102.
- Charlton, C. A. & Volkman, L. E. 1991. Sequential rearrangement and nuclear polymerization of actin in baculovirus-infected *Spodoptera frugiperda* cells. *Journal of Virology* 65 (3), 1219-1227.
- Cronshaw, J. M., Krutchinsky, A. N., Zhang, W., Chait, B. T. & Matunis, M. J. 2002. Proteomic analysis of the mammalian nuclear pore complex. *The Journal of Cell Biology* 158 (5), 915-927.
- Cudmore, S., Cossart, P., Griffiths, G. & Way, M. 1995. Actin-based motility of vaccinia virus. *Nature* 378, 636-638.
- Dardis, O. & McCloskey, J. 1998. Lattice Boltzmann scheme with real numbered solid density for the simulation of flow in porous media. *Physical Review E* 57 (4), 4834-4837.
- de Lanerolle, P. & Serebryanny, L. 2011. Nuclear actin and myosins: Life without filaments. *Nature Cell Biology* 13, 1282-1288.
- Delay, F., Porel, G. & Sardini, P. 2002. Modelling diffusion in a heterogeneous rock matrix with a time-domain Lagrangian method and an inversion procedure. *Comptes Rendus Geoscience* 334 (13), 967-73.
- Dickinson, R. B. & Purich, D. L. 2002. Clamped-filament elongation model for actin-based motors. *Biophysical Journal* 82 (2), 605-617.
- Dion, V. & Gasser, S. M. 2013. Chromatin movement in the maintenance of genome stability. *Cell* 152 (6), 1355-64.
- Dross, N., Spriet, C., Zwirger, M., Müller, G., Waldeck, W. & Langowski, J. 2009. Mapping eGFP oligomer mobility in living cell nuclei. *PLoS One* 4 (4), e5041.
- Einstein, A. 1905. Über die von der molekularkinetischen Theorie der Wärme geforderte Bewegung von in ruhenden Flüssigkeiten suspendierten Teilchen. *Annalen der Physik* 17, 549-560.
- Everett, R. D., Sourvinos, G. & Orr, A. 2003. Recruitment of herpes simplex virus type 1 transcriptional regulatory protein ICP4 into foci juxtaposed to ND10 in live, infected cells. *Journal of Virology* 77 (6), 3680-3689.

- Fama, E. F. 1965. Random walks in stock market prices. *Financial analysts journal* 21 (5), 55-59.
- Farnell, L. & Gibson, W. G. 2005. Monte Carlo simulation of diffusion in a spatially nonhomogeneous medium: A biased random walk on an asymmetrical lattice. *Journal of Computational Physics* 208, 253-265.
- Farnoosh, R., Yari, G. & Zarpak, B. 2008. Image segmentation using Gaussian mixture models. *IUST International Journal of Engineering Science* 19.
- Feldherr, C. M. 1965. The effect of the electron-opaque pore material on exchanges through the nuclear annuli. *The Journal of Cell Biology* 25 (1), 43-53.
- Finkelstein, A. 1976. Water and nonelectrolyte permeability of lipid bilayer membranes. *The Journal of General Physiology* 68 (2), 127-135.
- Fogelqvist, E., Kördel, M., Carannante, V., Önfelt, B. & Hertz, H. M. 2017. Laboratory cryo x-ray microscopy for 3D cell imaging. *Scientific Reports* 7, 13433.
- Forest, T., Barnard, S. & Baines, J. D. 2005. Active intranuclear movement of herpesvirus capsids. *Nature Cell Biology* 7 (4), 429-431.
- Franke, W. W., Scheer, U., Krohne, G. & Jarasch, E. -. 1981. The nuclear envelope and the architecture of the nuclear periphery. *The Journal of Cell Biology* 91 (3), 39s-50s.
- Franker, M. A. & Hoogenraad, C. C. 2013. Microtubule-based transport – basic mechanisms, traffic rules and role in neurological pathogenesis. *Journal of Cell Science* 126, 1-11.
- Fraser, M. J. 1986. Ultrastructural observations of virion maturation in *Autographa californica* nuclear polyhedrosis virus infected *Spodoptera frugiperda* cell cultures. *Journal of Ultrastructure and Molecular Structure Research* 95 (1-3), 189-195.
- Gerace, L., Blum, A. & Blobel, G. 1978. Immunocytochemical localization of the major polypeptides of the nuclear pore complex-lamina fraction. Interphase and mitotic distribution. *Journal of Cell Biology* 79, 546-566.
- Golding, I. & Cox, E. C. 2006. Physical nature of bacterial cytoplasm. *Physical Review Letters* 96, 098102.
- Goley, E. D., Ohkawa, T., Mancuso, J., Woodruff, J. B., D'Alessio, J. A., Cande, W. Z., Volkman, L. E. & Welch, M. D. 2006. Dynamic nuclear actin assem-

- bly by Arp2/3 complex and a baculovirus WASP-like protein. *Science* 314 (5798), 464-467.
- Görisch, S. M., Wachsmuth, M., Ittrich, C., Bacher, C. P., Rippe, K. & Lichter, P. 2004. Nuclear body movement is determined by chromatin accessibility and dynamics. *Proceedings of the National Academy of Sciences of the United States of America* 101 (36), 13221-13226.
- Gouin, E., Gantelet, H., Egile, C., Lasa, I., Ohayon, H., Villiers, V., Gounon, P., Sansonetti, P. J. & Cossart, P. 1999. A comparative study of the actin-based motilities of the pathogenic bacteria *Listeria monocytogenes*, *Shigella flexneri* and *Rickettsia conorii*. *Journal of Cell Science* 112 (11), 1697-1708.
- Han, K., Feng, Y. T. & Owen, D. R. J. 2008. Modelling of thermal contact resistance within the framework of the thermal lattice Boltzmann method. *International Journal of Thermal Sciences* 47 (10), 1276-1283.
- Hunter, J. R., Craig, P. D. & Phillips, H. E. 1993. On the use of random walk models with spatially variable diffusivity. *Journal of Computational Physics* 106 (2), 366-376.
- Ihalainen, T. O., Laakkonen, J. P., Paloheimo, O., Ylä-Herttua, S., Airene, K. J. & Vihinen-Ranta, M. 2010. Morphological characterization of baculovirus *Autographa californica* multiple nucleopolyhedrovirus. *Virus Research* 148 (1-2), 71-74.
- Kac, M. 1947. Random walk and the theory of Brownian motion. *The American Mathematical Monthly* 54 (7), 369-391.
- Kareiva, P. M. & Shigesada, N. 1983. Analyzing insect movement as a correlated random walk. *Oecologia* 56, 234-238.
- Klafter, J. & Sokolov, I. M. 2005. Anomalous diffusion spreads its wings. *Physics World* 18 (8), 29-32.
- Krichevsky, O. & Bonnet, G. 2002. Fluorescence correlation spectroscopy: the technique and its applications. *Reports on Progress in Physics* 65, 251-297.
- Kristó, I., Bajusz, I., Bajusz, C., Borkúti, P. & Vilmos, P. 2016. Actin, actin-binding proteins, and actin-related proteins in the nucleus. *Histochemistry and Cell Biology* 145 (4), 373-388.
- Kühn, T., Ihalainen, T. O., Hyväluoma, J., Dross, N., Willman, S. F., Langowski, J., Vihinen-Ranta, M. & Timonen, J. 2011. Protein diffusion in mammalian cell cytoplasm. *PLoS One* 6 (8), e22962.

- Lanier, L. M. & Volkman, L. E. 1998. Actin binding and nucleation by *Autographa californica* M nucleopolyhedrovirus. *Virology* 243 (1), 167-177.
- Le Gros, M. A., Clowney, E. J., Magklara, A., Yen, A., Markenscoff-Papadimitriou, E., Colquitt, B., Myllys, M., Kellis, M., Lomvardas, S. & Larabell, C. A. 2016. Soft x-ray tomography reveals gradual chromatin compaction and reorganization during neurogenesis in vivo. *Cell Reports* 17 (8), 2125-2136.
- Luby-Phelps, K. 2000. Cytoarchitecture and physical properties of cytoplasm: volume, viscosity, diffusion, intracellular surface area. *International Review of Cytology* 192, 189-221.
- Luger, K., Mäder, A. W., Richmond, R. K., Sargent, D. F. & Richmond, T. J. 1997. Crystal structure of the nucleosome core particle at 2.8 Å resolution. *Nature* 389, 251-260.
- Lyman, M. G. & Enquist, L. W. 2009. Herpesvirus Interactions with the Host Cytoskeleton. *Journal of Virology* 83, 2058-66.
- Machesky, L. M., Insall, R. H. & Volkman, L. E. 2001. WASP homology sequences in baculoviruses. *Trends in Cell Biology* 11, 286-287.
- Magde, D., Elson, E. & Webb, W. W. 1972. Thermodynamic fluctuations in a reacting system – measurement by fluorescence correlation spectroscopy. *Physical Review Letters* 29, 705-708.
- Maul, G. G. & Deaven, L. 1977. Quantitative determination of nuclear pore complexes in cycling cells with differing DNA content. *The Journal of Cell Biology* 73 (3), 748-760.
- Maul, G. G., Maul, H. M., Scogna, J. E., Lieberman, M. W., Stein, G. S., Hsu, B. Y. & Borun, T. W. 1972. Time sequence of nuclear pore formation in phytohemagglutinin-stimulated lymphocytes and in HeLa cells during the cell cycle. *The Journal of Cell Biology* 55 (2), 433-447.
- McCarthy, J. F. 1993. Continuous-time random walks on random media. *Journal of Physics A General Physics* 26 (11), 2495-503.
- McDermott, G., Le Gros, M. A., Knoechel, C. G., Uchida, M. & Larabell, C. A. 2009. Soft X-ray tomography and cryogenic light microscopy: the cool combination in cellular imaging. *Trends in Cell Biology* 19 (11), 587-595.
- Mettenleiter, T. C., Klupp, B. G. & Granzow, H. 2006. Herpesvirus assembly: a tale of two membranes. *Current Opinion in Microbiology* 9, 423-9.

- Mogilner, A. & Oster, G. 2003. Force generation by actin polymerization II: the elastic ratchet and tethered filaments. *Biophysical Journal* 84 (3), 1591-1605.
- Montroll, E. W. & Weiss, G. H. 1965. Random walks on lattices. II. *Journal of Mathematical Physics* 6 (2), 167-81.
- Mueller, J., Pfanzelter, J., Winkler, C., Narita, A., Le Clainche, C., Nemethova, M., Carlier, M. -, Maeda, Y., Welch, M. D., Ohkawa, T., Schmeiser, C., Resch, G. P. & Small, J. V. 2014. Electron tomography and simulation of baculovirus actin comet tails support a tethered filament model of pathogen propulsion. *PLoS Biology* 12 (1), e1001765.
- Myllys, M., Ruokolainen, V., Aho, V., Smith, E. A., Hakanen, S., Peri, P., Salvetti, A., Timonen, J., Hukkanen, V., Larabell, C. A. & Vihinen-Ranta, M. 2016. Herpes simplex virus 1 induces egress channels through marginalized host chromatin. *Scientific Reports* 6:28844.
- Nagamine, T., Kawasaki, Y., Abe, A. & Matsumoto, S. 2008. Nuclear marginalization of host cell chromatin associated with expansion of two discrete virus-induced subnuclear compartments during baculovirus infection. *Journal of Virology* 82 (13), 6409-18.
- Novak, I. L., Kraikivski, P. & Slepchenko, B. M. 2009. Diffusion in cytoplasm: effects of excluded volume due to internal membranes and cytoskeletal structures. *Biophysical Journal* 97 (3), 758-767.
- Ohkawa, T., Volkman, L. E. & Welch, M. D. 2010. Actin-based motility drives baculovirus transit to the nucleus and cell surface. *The Journal of Cell Biology* 190 (2), 187-195.
- Ohkawa, T. & Welch, M. D. 2016. Intranuclear actin-based motility drives nuclear envelope disruption during baculovirus egress. Poster presented at 2016 ASCB annual meeting December 3-7, San Francisco, CA, USA.
- Otsu, N. 1979. A threshold selection method from gray-level histograms. *IEEE Transactions on Systems, Man and Cybernetics* 9 (1), 62-66.
- Pante, N. & Kann, M. 2002. Nuclear pore complex is able to transport macromolecules with diameters of ~39 nm. *Molecular Biology of the Cell* 13 (2), 425-434.
- Pelkmans, L., Püntener, D. & Helenius, A. 2002. Local actin polymerization and dynamin recruitment in SV40-induced internalization of caveolae. *Science* 296 (5567), 535-539.

- Peters, R. 1983. Nuclear envelope permeability measured by fluorescence microphotolysis of single liver cell nuclei. *The Journal of Biological Chemistry* 258 (19), 11427-11429.
- Phillips, R., Kondev, J., Theriot, J. & Garcia, H. G. 2012. *Physical biology of the cell*. (2nd edition) New York: Garland Science.
- Piazzesi, G., Reconditi, M., Linari, M., Lucii, L., Bianco, P., Brunello, E., Decostre, V., Stewart, A., Gore, D. B., Irving, T. C., Irving, M. & Lombardi, V. 2007. Skeletal muscle performance determined by modulation of number of myosin motors rather than motor force or stroke size. *Cell* 131 (4), 784-795.
- Plastino, J. & Sykes, C. 2005. The actin slingshot. *Current Opinion in Cell Biology* 17 (1), 62-66.
- Potma, E. O., de Boeij, W. P., Bosgraaf, L., Roelofs, J., van Haastert, P. J. & Wiersma, D. A. 2001. Reduced protein diffusion rate by cytoskeleton in vegetative and polarized dictyostelium cells. *Biophysical Journal* 81 (4), 2010-2019.
- Randall, R. E. & Dinwoodie, N. 1986. Intranuclear localization of herpes simplex virus immediate-early and delayed-early proteins: evidence that ICP 4 is associated with progeny virus DNA. *The Journal of General Virology* 67, 2163-77.
- Reverey, J. F., Jeon, J. -, Bao, H., Leippe, M., Metzler, R. & Selhuber-Unkel, C. 2015. Superdiffusion dominates intracellular particle motion in the supercrowded cytoplasm of pathogenic *Acanthamoeba castellanii*. *Scientific Reports* 5, 11690.
- Roberts, A. J., Kon, T., Knight, P. J., Sutoh, K. & Burgess, S. A. 2013. Functions and mechanics of dynein motor proteins. *Nature Reviews. Molecular Cell Biology* 14 (11), 713-726.
- Schneiter, R., Brügger, B., Sandhoff, R., Zellnig, G., Leber, A., Lampl, M., Athenstaedt, K., Hrastrnik, C., Eder, S., Daum, G., Paltauf, F., Wieland, F. T. & Kohlwein, S. D. 1999. Electrospray ionization tandem mass spectrometry (Esi-MS/MS) analysis of the lipid molecular species composition of yeast subcellular membranes reveals acyl chain-based sorting/remodeling of distinct molecular species en route to the plasma membrane. *The Journal of Cell Biology* 146 (4), 741-754.
- Schnitzer, M. J. & Block, S. M. 1997. Kinesin hydrolyses one ATP per 8-nm step. *Nature* 388, 386-390.

- Schrag, J. D., Venkataram Prasad, B. V., Rixon, F. J. & Chiu, W. 1989. Three-dimensional structure of the HSV1 nucleocapsid. *Cell* 56, 651-60.
- Sodeik, B., Ebersold, M. W. & Helenius, A. 1997. Microtubule-mediated transport of incoming herpes simplex virus 1 capsids to the nucleus. *The Journal of Cell Biology* 136 (5), 1007-1021.
- Soumpasis, D. M. 1983. Theoretical analysis of fluorescence photobleaching recovery experiments. *Biophysical Journal* 41 (1), 95-97.
- Succi, S. 2001. *The lattice Boltzmann equation for fluid dynamics and beyond*. Oxford: Clarendon Press.
- Sweeney, H. L. & Houdusse, A. 2010. Structural and functional insights into the Myosin motor mechanism. *Annual Review of Biophysics* 39 (539-557).
- Syamaladevi, D. P., Spudich, J. A. & Sowdhamini, R. 2012. Structural and functional insights on the Myosin superfamily. *Bioinformatics and Biology Insights* 6, 11-21.
- Tilney, L. G. & Portnoy, D. A. 1989. Actin filaments and the growth, movement, and spread of the intracellular bacterial parasite, *Listeria monocytogenes*. *Journal of Cell Biology* 109 (4), 1597-1608.
- Timney, B. L., Raveh, B., Mironska, R., Trivedi, J. M., Kim, S. J., Russel, D., Wente, S. R., Sali, A. & Rout, M. P. 2016. Simple rules for passive diffusion through the nuclear pore complex. *The Journal of Cell Biology* 215 (1), 57-76.
- Visscher, K., Schnitzer, M. J. & Block, S. M. 1999. Single kinesin molecules studied with a molecular force clamp. *Nature* 400, 184-189.
- Viswanathan, G. M., Afanasyev, V., Buldyrev, S. V., Murphy, E. J., Prince, P. A. & Stanley, H. E. 1996. Lévy flight search patterns of wandering albatrosses. *Nature* 381, 413-415.
- Wachsmuth, M., Waldeck, W. & Langowski, J. 2000. Anomalous diffusion of fluorescent probes inside living cell nuclei investigated by spatially-resolved fluorescence correlation spectroscopy. *Journal of Molecular Biology* 298 (4), 677-689.
- Wang, R. & Brattain, M. G. 2007. The maximal size of protein to diffuse through the nuclear pore is larger than 60kDa. *FEBS Letters* 581 (17), 3164-3170.
- Wei, X., Henke, V. G., Strübing, C., Brown, E. B. & Clapham, D. E. 2003. Real-time imaging of nuclear permeation by EGFP in single intact cells. *Biophysical Journal* 84 (2), 1317-1327.

- Weiss, M., Elsner, M., Kartberg, F. & Nilsson, T. 2004. Anomalous subdiffusion is a measure for cytoplasmic crowding in living cells. *Biophysical Journal* 87 (5), 3518-3524.
- Welch, M. D. & Way, M. 2013. Arp2/3-mediated actin-based motility: a tail of pathogen abuse. *Cell Host Microbe* 14, 242-55.
- Wiesner, S., Helfer, E., Didry, D., Ducouret, G., Lafuma, F., Carlier, M. - & Pantaloni, D. 2003. A biomimetic motility assay provides insight into the mechanism of actin-based motility. *The Journal of Cell Biology* 160 (3), 387-398.
- Woehlke, G. & Schliwa, M. 2000. Walking on two heads: the many talents of kinesin. *Nature Reviews. Molecular Cell Biology* 1 (1), 50-58.
- Wolf-Gladrow, D. 1995. A lattice Boltzmann equation for diffusion. *Journal of Statistical Physics* 79 (5-6), 1023-1032.

ORIGINAL PAPERS

I

DIFFUSION THROUGH THIN MEMBRANES: MODELING ACROSS SCALES

by

Aho, V., Mattila, K., Kühn, T., Kekäläinen, P., Pulkkinen, O., Brondani Minussi, R.,
Vihinen-Ranta, M. & Timonen, J.

Physical Review E, 93:043309, 2016

Diffusion through thin membranes: Modeling across scales

Vesa Aho*

Department of Physics, and Nanoscience Center, P.O. Box 35, University of Jyväskylä, FI-40014 Jyväskylä, Finland

Keijo Mattila

*Department of Physics, and Nanoscience Center, P.O. Box 35, University of Jyväskylä, FI-40014 Jyväskylä, Finland
and Department of Physics, P.O. Box 692, Tampere University of Technology, FI-33101 Tampere, Finland*

Thomas Kühn

Department of Applied Physics, P.O. Box 1627, University of Eastern Finland, FI-70211 Kuopio, Finland

Pekka Kekäläinen

Department of Chemistry, P.O. Box 55, University of Helsinki, FI-00014 Helsinki, Finland

Otto Pulkkinen

Department of Physics, P.O. Box 692, Tampere University of Technology, FI-33101 Tampere, Finland

Roberta Brondani Minussi

Oxford Centre for Industrial and Applied Mathematics, Mathematical Institute, University of Oxford, Oxford, United Kingdom

Maija Vihinen-Ranta

Department of Biological and Environmental Science, and Nanoscience Center, P.O. Box 35, University of Jyväskylä, FI-40014 Jyväskylä, Finland

Jussi Timonen

*Department of Physics, and Nanoscience Center, P.O. Box 35, University of Jyväskylä, FI-40014 Jyväskylä, Finland
and ITMO University, Kronverkskii Ave. 49, 197101, Saint Petersburg, Russia*

(Received 16 November 2015; revised manuscript received 13 February 2016; published 12 April 2016)

From macroscopic to microscopic scales it is demonstrated that diffusion through membranes can be modeled using specific boundary conditions across them. The membranes are here considered thin in comparison to the overall size of the system. In a macroscopic scale the membrane is introduced as a transmission boundary condition, which enables an effective modeling of systems that involve multiple scales. In a mesoscopic scale, a numerical lattice-Boltzmann scheme with a partial-bounceback condition at the membrane is proposed and analyzed. It is shown that this mesoscopic approach provides a consistent approximation of the transmission boundary condition. Furthermore, analysis of the mesoscopic scheme gives rise to an expression for the permeability of a thin membrane as a function of a mesoscopic transmission parameter. In a microscopic model, the mean waiting time for a passage of a particle through the membrane is in accordance with this permeability. Numerical results computed with the mesoscopic scheme are then compared successfully with analytical solutions derived in a macroscopic scale, and the membrane model introduced here is used to simulate diffusive transport between the cell nucleus and cytoplasm through the nuclear envelope in a realistic cell model based on fluorescence microscopy data. By comparing the simulated fluorophore transport to the experimental one, we determine the permeability of the nuclear envelope of HeLa cells to enhanced yellow fluorescent protein.

DOI: [10.1103/PhysRevE.93.043309](https://doi.org/10.1103/PhysRevE.93.043309)**I. INTRODUCTION**

Membranes are selective barriers restricting transport of material between two regions. They are ubiquitous in living organisms; the transport of molecules between a cell and its exterior, and between many cellular compartments, is regulated by lipid bilayers outlining them. These membranes are extremely thin in comparison with the size of the whole cell. For example, the nuclear envelope of a cell is about tens of nanometers thick [1], while a typical eukaryotic cell is

around tens of micrometers in diameter. Hence, a detailed modeling of mass transport in a cell will involve multiple length and time scales. Besides being important building blocks in living organisms, membranes are used in many environmental and industrial applications like food processing and water purification via osmosis [2,3].

In a macroscopic scale, the rate of transport of solute molecules across a membrane is quantified by

$$J_m = -P\delta\rho, \quad (1)$$

where J_m is the flux of particles across the membrane and $\delta\rho$ is the difference between concentrations at the opposite faces

*vesa.p.aho@jyu.fi

of the membrane. In other words, the membrane induces a concentration jump $\delta\rho$ across it. Moreover, the coefficient of proportionality P is the membrane permeability. In the standard solubility-diffusion model, for example, $P = K D_m/w$, where K is a dimensionless partition coefficient, D_m is the intrinsic diffusion coefficient in the membrane, and w is the membrane thickness [4,5].

In this article, we examine diffusion through thin membranes. In a macroscopic analysis, we treat the membrane as a transmission boundary condition between two regions, and derive solutions for the concentration fields in simple configurations. However, many applications of great interest are beyond an analytical treatment due to inherent complexities involved. Hence it is of practical importance to consider numerical modeling of membranes as well. A numerical treatment of continuum-based models requires discretization of the space. When the membrane is considered as a singularity also in the scale of discretization, say in the scale of lattice spacing, it is not immediately clear how the permeability in a numerical scheme should be implemented to be in accordance with the permeability of Eq. (1) in the continuum description. The situation is even more complex in numerical methods which do not explicitly contain the macroscopic differential equations they solve, such as the lattice-Boltzmann method (LBM) [6,7].

In order to focus on this issue, we discretize the macroscopic transmission conditions so as to derive an expression for the mass flux between two discretization points separated by a membrane. The obtained expressions can be readily utilized, e.g., in finite-difference and finite-volume methods for solving the diffusion equation. In a mesoscopic scale, we propose an implementation of LBM, where the membrane is treated as a partial-bounceback condition between two lattice nodes. After presenting the discrete scheme, we perform a multiple-scale analysis and derive an explicit expression for the mass flux at the membrane. To bridge the gap between microscopic and mesoscopic descriptions, we show, in a microscopic description, that the flux coincides with the inverse mean waiting time of a single molecule in the vicinity of the membrane.

Finally, we show that the numerical approximations with LBM agree with analytically derived solutions at a macroscopic level, and show the applicability of the LBM scheme by determining the permeability of the nuclear envelope to enhanced yellow fluorescent protein (EYFP). In this numerical determination of permeability, photobleaching experiments are compared against simulations executed using realistic, three-dimensional, image-based geometries.

II. CONTINUUM THEORY

To begin with, in a macroscopic scale the diffusion equation with a constant diffusion coefficient D is given by

$$\partial_t \rho(x,t) - D \partial_x^2 \rho(x,t) = 0, \quad (2)$$

and Fick's law for the mass flux J is given by

$$J = -D \partial_x \rho. \quad (3)$$

Using Eq. (1) and continuity of the mass flux, we find that the transmission conditions at the membrane (at $x = 0$) can be

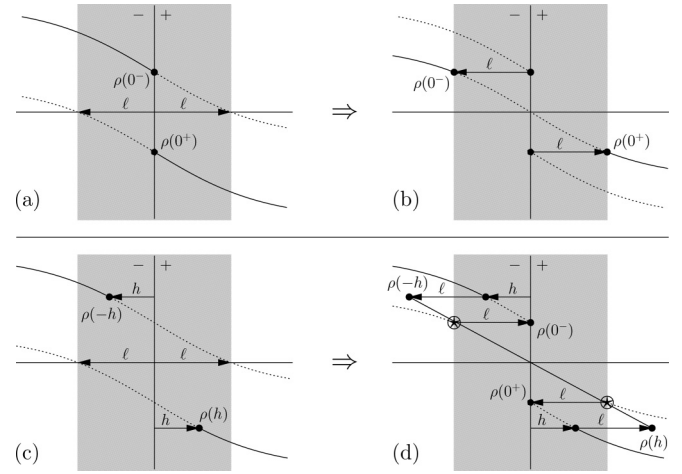


FIG. 1. The top part of the figure, (a) and (b), illustrates an interpretation of the effective membrane thickness, 2ℓ , using $\ell = D/2P$. Shifting the concentration profile by ℓ will remove the concentration jump and, hence, remedy the discontinuity [8]. The bottom part of the figure, (c) and (d), is a schematic description for the linear interpolation of $\rho(0^+)$ and $\rho(0^-)$ according to Eq. (11). The stars indicate the two interpolation points.

expressed in the form,

$$\begin{aligned} D \partial_x \rho(0^-, t) &= P[\rho(0^+, t) - \rho(0^-, t)], \\ \partial_x \rho(0^+, t) &= \partial_x \rho(0^-, t), \end{aligned} \quad (4)$$

where $\rho(0^+)$ and $\rho(0^-)$ now denote concentrations at the opposite faces of the membrane.

Note that the mass flux across the membrane, Eq. (1), can also be expressed in the form,

$$J_m = -D \frac{\rho(0^+) - \rho(0^-)}{2\ell} = -D \partial_x \rho + \mathcal{O}(\ell^2); \quad (5)$$

an effective thickness of the membrane, 2ℓ , is defined using $\ell = D/2P$ [8]. That is, even though the concentration is not formally differentiable across the membrane, a diffusive transport across it can be expressed by the usual Fick's law, when the partial derivative is understood in the manner described above (see the top part of Fig. 1).

A. A steady-state configuration

The steady-state solution for a one-dimensional (1D) diffusion equation, given by $J = -D \partial_x \rho = \text{constant}$, implies a linear concentration profile. Let us consider a domain $[-L/2, L/2]$ with a given reference concentration ρ_r , and a fixed concentration difference $\Delta\rho_L$ between the domain ends, i.e., the boundary conditions,

$$\rho(-L/2) = \rho_r + \frac{\Delta\rho_L}{2} \quad \text{and} \quad \rho(L/2) = \rho_r - \frac{\Delta\rho_L}{2},$$

can support a nonzero, constant mass flux at steady state.

Since the configuration is symmetric,

$$\rho(0^-) = \rho_r + \frac{\delta\rho}{2} \quad \text{and} \quad \rho(0^+) = \rho_r - \frac{\delta\rho}{2}. \quad (6)$$

A transmission boundary condition then enforces a continuous mass flux for a discontinuous concentration, and can be

expressed in the form,

$$D(\partial_x \rho)(0^-) = P\delta\rho = D(\partial_x \rho)(0^+).$$

Since the concentration profile in the bulk is linear at steady state,

$$(\partial_x \rho)(0^-) = \frac{\rho(0^-) - \rho(-L/2)}{L/2} = \frac{\delta\rho - \Delta\rho_L}{L}.$$

Exactly the same expression is obtained for $(\partial_x \rho)(0^+)$. Hence,

$$\frac{D}{L}[\Delta\rho_L - \delta\rho] = P\delta\rho,$$

which finally leads to

$$\delta\rho = \frac{\Delta\rho_L}{1 + \gamma}, \quad (7)$$

where $\gamma = LP/D$.

B. A transient configuration

An analytical solution can be derived for the above membrane boundary condition in the case, where $x \in [-L, 0) \cup (0, L]$, and concentration is initially uniform on one side of the membrane and zero on the other. Mathematically, we write a no-flux boundary condition at $\pm L$,

$$\partial_x \rho(L, t) = \partial_x \rho(-L, t) = 0,$$

and an initial condition at $t = 0$:

$$\rho(x, 0) = \begin{cases} 1; & -L \leq x \leq 0, \\ 0; & 0 < x \leq L. \end{cases}$$

Note that in the following analysis we will, for simplicity, use dimensionless densities which can be understood as normalized quantities of the form $\tilde{\rho} = \rho/\rho_r$, where ρ_r is a reference density. Defining $\xi = x/L$ and $\tilde{t} = t D/L^2$, we can solve the resulting dimensionless problem by separation of variables (see Appendix A), and find that

$$\begin{aligned} \rho(\xi, \tilde{t}) &= \frac{1}{2} - \sum_{k=0}^{\infty} \frac{2\gamma e^{-\mu_{2k+1}^2 \tilde{t}}}{\mu_{2k+1}^2 + 4\gamma^2 + 2\gamma} \\ &\times \left(\text{sgn}(\xi) \cos(\mu_{2k+1} \xi) + \frac{2\gamma}{\mu_{2k+1}} \sin(\mu_{2k+1} \xi) \right), \end{aligned} \quad (8)$$

where again $\gamma = LP/D$, and the eigenvalues μ satisfy

$$\begin{aligned} \mu_{2k} &= k\pi; \quad k = 0, 1, \dots \\ \tan \mu_{2k+1} &= \frac{2\gamma}{\mu_{2k+1}}; \quad k\pi < \mu_{2k+1} < k\pi + \frac{\pi}{2}. \end{aligned} \quad (9)$$

III. DISCRETIZATION OF THE TRANSMISSION BOUNDARY CONDITIONS

In a fine enough discrete numerical model, the membrane can be constructed explicitly by assigning a number of discretization points to it, and setting the membrane diffusion coefficient D_m in those points such that the desired flux through the membrane, Eq. (3), will be obtained. Here we continue instead to treat the membrane as a boundary condition. In a true

multiscale-modeling fashion, we place the membrane *between* two discretization points and discretize the transmission conditions of Eq. (4). We set up our computational grid such that there is a grid point on each side of the membrane with an equal distance h to it.

Furthermore, the continuity condition for the flux at the membrane, approximated to first order in space with backward and forward differences, is given by

$$D \frac{\rho(h) - \rho(0^+)}{h} = D \frac{\rho(0^-) - \rho(-h)}{h}. \quad (10)$$

Setting $P[\rho(0^+) - \rho(0^-)]$ equal to both sides of Eq. (10), separately, we can express $\rho(0^+)$ and $\rho(0^-)$ in terms of $\rho(h)$ and $\rho(-h)$. In this way we find that

$$\begin{cases} \rho(0^+) = \left[1 - \frac{h}{2(h+\ell)}\right]\rho(+h) + \frac{h}{2(h+\ell)}\rho(-h), \\ \rho(0^-) = \left[1 - \frac{h}{2(h+\ell)}\right]\rho(-h) + \frac{h}{2(h+\ell)}\rho(+h). \end{cases} \quad (11)$$

That is, Eq. (11) defines a linear interpolation for obtaining the concentrations at the membrane using the two adjacent discretization points (see the bottom part of Fig. 1). Note that this interpolation is consistent, when $h \rightarrow 0$.

After substituting these expressions into Eq. (1), we find further that

$$J_m = -P \left[\frac{\ell}{h + \ell} \Delta\rho \right] = -P \left[\frac{1}{\lambda + 1} \Delta\rho \right], \quad (12)$$

where $\Delta\rho = \rho(h) - \rho(-h)$ and the dimensionless coefficient $\lambda = h/\ell = 2hP/D$. That is, the mass flux across the membrane is now expressed using the concentration difference between the two adjacent grid points, not between the two faces of the membrane. Therefore the measured difference must be adjusted so as to be consistent with the definition of the permeability coefficient. Thus $\Delta\rho/(1 + \lambda)$ can be considered as the concentration jump interpolated at the membrane.

A. Effective diffusion coefficient in the membrane

An alternative interpretation of the mass flux in Eq. (12) can be adopted. Using the definition of λ , we arrive at

$$J_m = -\frac{\lambda}{1 + \lambda} D \frac{\Delta\rho}{2h} = -\frac{\lambda}{1 + \lambda} D \partial_x \rho(0) + \mathcal{O}(h^2). \quad (13)$$

This same expression, but in a different context, has been reported, e.g., in Refs. [9,10]. Now the partial derivative at the membrane is approximated using the discretization points and, in particular, not across the effective membrane thickness, cf. Eq. (5). While the coefficients in Eq. (13) originate from the concentration-jump approximation, this mass-flux expression is quite elegant: The effect of the membrane is manifested by a single coefficient λ , having the role of reducing the corresponding bulk mass flux. Accordingly, the coefficient $\lambda D/(1 + \lambda)$ can be considered as the effective diffusion coefficient for the membrane. The obtained expressions, Eqs. (11)–(13), can be utilized, e.g., in finite-difference and finite-volume methods for solving the diffusion equation.

IV. LATTICE-BOLTZMANN MODELING OF DIFFUSION ACROSS A MEMBRANE

Numerical modeling on the level of distribution functions of the solute, i.e., on a mesoscopic scale, is conveniently implemented using the lattice-Boltzmann method [6,7], which has emerged as an alternative in a computational treatment of complex transport phenomena. Diffusion processes, for example, can be simulated using the standard lattice-Boltzmann evolution equation with the BGK collision operator [11],

$$f_i(\mathbf{r} + \delta t \mathbf{c}_i, t + \delta t) = f_i(\mathbf{r}, t) - \frac{f_i(\mathbf{r}, t) - f_i^{\text{eq}}(\rho)}{\tau^*},$$

where $i = 0, \dots, q-1$, where q is the number of discrete velocities in the model, τ^* is a dimensionless relaxation time, ρ denotes the local concentration at a given instant, and w_i are suitable weight coefficients for the equilibrium function, $f_i^{\text{eq}} = w_i \rho$. The lattice spacing δr , and discrete time step δt , define a reference velocity, $c_r = \delta r / \delta t$, and $\mathbf{c}_i = c_r \mathbf{c}_i^*$, where \mathbf{c}_i^* are the dimensionless lattice vectors.

The first few moments of the discrete equilibrium distribution function are given by

$$\begin{aligned} \sum_i f_i^{\text{eq}} &= \rho, & \sum_i c_{i,\alpha} f_i^{\text{eq}} &= 0, \\ \sum_i c_{i,\alpha} c_{i,\beta} f_i^{\text{eq}} &= b c_r^2 \rho \delta_{\alpha\beta}, \end{aligned}$$

where b is a constant fixed by selection of the weight coefficients w_i (see Appendix B). The diffusion coefficient can be derived, e.g., with the Chapman-Enskog procedure [11]:

$$D = (\tau^* - 1/2) b \delta t c_r^2. \quad (14)$$

As already mentioned, the most elementary way to construct the membrane in a lattice-Boltzmann framework is to assign a number of lattice nodes to it; the flux is controlled with the diffusion coefficient D_m , e.g., by setting the relaxation time appropriately. This is also the approach taken in Ref. [12] to model the nuclear envelope. However, if the membrane restricts the transport strongly, relaxation time at the membrane sites can be inconveniently small (with respect to the numerical stability [13]), or too large in the surrounding environment (with respect to the numerical error [11]). A possible way to circumvent this problem is to use a local grid refinement at the membrane and its immediate neighborhood. Unfortunately in a complex geometry, which is the typical case, such refinement may be cumbersome or not feasible at all.

Instead, we follow Ref. [14], where a mesoscopic boundary condition corresponding to Eq. (1) was reported, and utilize this simple boundary condition for the implementation of a membrane in a lattice-Boltzmann scheme. The condition relies on a single parameter (we will call it ϕ in the following) that controls the proportion of particles which are able to pass through the membrane. Namely, we introduce a partial halfway-bounceback rule for the distributions that cross the membrane,

$$f_i(\mathbf{r} + \delta t \mathbf{c}_i, t + \delta t) = \phi f_i(\mathbf{r}, t) + (1 - \phi) f_{-i}(\mathbf{r} + \delta t \mathbf{c}_i, t), \quad (15)$$

where subscript $-i$ denotes the direction which is opposite to that of i , i.e., $\mathbf{c}_{-i} = -\mathbf{c}_i$. That is, the location of the

membrane is halfway between two neighboring lattice nodes. Depending on the application, ϕ can be associated with, e.g., the relative area of the membrane, which allows diffusive transport. Equation (15) provides a subgrid-scale model for the membrane diffusion, and it is conveniently implemented even in arbitrarily complex geometries. Previously partial-bounceback schemes have been used in the LBM context for modeling transport in porous media [15–18], thermal conduction across the boundary between two materials [19], or slip flows [20,21].

The Chapman-Enskog analysis of the scheme of Eq. (15) shows (see Appendix B) that it leads to the modified flux as obtained above at the membrane, Eq. (12), and the restrictive effect of the membrane is included in the coefficient $\lambda = P \delta r / D$, $h = \delta r / 2$, where the permeability is given by

$$P = \frac{\phi}{(1 - \phi)^2} \frac{b}{2} c_r. \quad (16)$$

That is, the partial-bounceback scheme is an alternative discretization of the transmission boundary condition.

It is also evident that this expression for the permeability implies a reasonable limiting behavior,

$$J_m \longrightarrow \begin{cases} 0, & \text{when } \phi \longrightarrow 0, \\ -D \partial_\alpha \rho, & \text{when } \phi \longrightarrow 1. \end{cases}$$

Furthermore, when D approaches infinity, i.e., when transport is limited only by the effect of the membrane, J_m approaches the value $-D \partial_\alpha \rho$. This is consistent with Eq. (1), and shows that P can indeed be thought of as the permeability of the membrane. This allows us to compare an approximate solution computed by the lattice-Boltzmann scheme with the analytical solution derived above.

V. MICROSCOPIC MODELING OF DIFFUSION THROUGH A MEMBRANE

We interpret the permeability of the Chapman-Enskog analysis, Eq. (16), in terms of the kinetics of individual solute molecules by studying a single-particle stochastic diffusion process, the probability density of which coincides with the solution of the macroscopic diffusion equation, Eq. (2), with the flux boundary condition, Eq. (4), at the membrane. In that sense, it is the exact microscopic counterpart of the macroscopic description.

The idea of the microscopic process is that a particle must on average collide with the membrane a sufficient number of times to find a pore, through which it passes to the other side of the membrane. Hence there is a pore-density-dependent probability to go through the membrane *given* that the particle is at its immediate vicinity. In a continuum model, the time spent at the membrane is measured by the *local time* [22],

$$L_t = \lim_{\epsilon \rightarrow 0} \frac{1}{2\epsilon} \int_0^t I(-\epsilon < X_s < \epsilon) ds,$$

where X_t is the position of the particle at time t and I is an indicator function. The local time is clearly a stochastic process that can only increase in time. The trajectories of the process L_t typically consist of long periods with no change in its value, as the Brownian particle is on an excursion far

away from the membrane, and bursts of rapid increase when the particle is in its close vicinity.

A continuum stochastic process X_t that passes through the membrane when its local time at the membrane exceeds an exponential random variable is an extension of the elastic Brownian motion [20], called snapping-out Brownian motion in a recent preprint [23]. In the preprint, the process was also shown to be the limit of a diffusion through a membrane of a vanishing diffusion constant $D(w)$ as the membrane width $w \rightarrow 0$. The first passage through the membrane was further shown to be marked by the local time exceeding an exponential random variable with a characteristic time scale, $\tau_c = \lim_{w \rightarrow 0} w/D(w)$, which depends on the microscopic structure of the membrane. However, it can be written down for the residence times of random walks with an idealized, infinitely thin membrane (see Appendix C).

Taking the continuum limit results in a snapping-out Brownian motion, and provides the equivalence of single-molecule and ensemble-averaged permeabilities,

$$\frac{1}{\tau_c} \propto \frac{\phi}{1-\phi}.$$

In other words, the inverse mean local time at the membrane before the particle passes through to its other side is proportional to the permeability in an ensemble experiment. This result is reminiscent of single-molecule reaction kinetics, in which case the mean waiting time to the next chemical reaction that involves an individual enzyme molecule equals the inverse of reaction velocity in a large ensemble of constituent molecules [24].

VI. VERIFICATION OF THE LB MEMBRANE SCHEME

Here we numerically verify that the above presented LB membrane scheme indeed is a consistent discretization of the transmission boundary conditions presented in Sec. II. To this end, we simulated diffusion across a membrane in a one-dimensional setting using the standard LB scheme for diffusion [11] together with the D1Q3 discrete velocity set. We chose $b = 2/3$ which implies $w_i = 1/3$ for all i . Furthermore, we used a constant value for the dimensionless relaxation time, i.e., $\tau^* = \tau/\delta t = 3/2$. The permeability was controlled with ϕ according to Eq. (16). The values of D and P used in the simulations were then substituted into Eqs. (7) and (8) when evaluating the analytical profile.

A. Steady-state benchmark case

First we considered a steady-state benchmark case. The main idea is to compare the analytically derived approximation for the mass flux, Eq. (12), with the mass flux computed numerically. We also compare the analytical and simulated concentration profiles.

In a standard LB scheme for diffusion, the local mass flux is computed as the first moment of nonequilibrium distributions averaged over pre- and post-collisional states. Let J^n denote the flux across the membrane (where n stands for the numerical flux). We then measure (when using D1Q3)

$$J^n = \left(1 - \frac{\delta t}{2\tau}\right) c_r [f_E^{\text{neq}}(\delta r/2) - f_W^{\text{neq}}(-\delta r/2)], \quad (17)$$

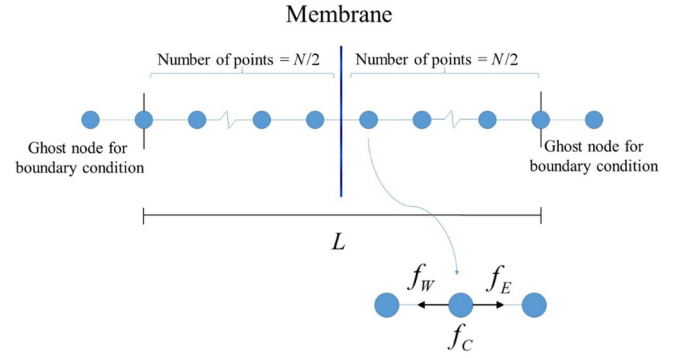


FIG. 2. The 1D steady-state benchmark configuration. The LB scheme is utilized together with the D1Q3 discrete velocity set. The two nodes adjacent to the membrane are located at $-\delta r/2$ and $\delta r/2$.

where $f_E^{\text{neq}}(\delta r/2)$ is the nonequilibrium distribution at the right-hand side of the membrane and at the pre-collision state; $f_W^{\text{neq}}(-\delta r/2)$ is defined accordingly (see Fig. 2).

We carried out the simulations enforcing constant concentrations $\rho(-L/2) = \rho_r + \Delta\rho_L/2$ and $\rho(L/2) = \rho_r - \Delta\rho_L/2$ at the boundaries: ρ_r and L are the reference concentration and domain length, and $\Delta\rho_L$ is the given concentration difference across the domain. These boundary concentrations were also used as the initial concentrations on the left and right subdomains.

All tests were made using $N = 40$ lattice nodes. When comparing to an analytical solution with given P , D , and L , the simulation parameters are then the lattice spacing $\delta r = L/(N-1)$, from Eq. (14) the discrete time step $\delta t = (\tau^* - 1/2)b\delta r^2/D$, and from Eq. (16) the transmission parameter $\phi = 1/(1+C)$, where $C = b\delta r/(2P\delta t)$. We used $\rho_r = 1$ kg/m, $L = 1$ cm, $D = 0.05$ cm²/s in all of our comparisons, and varied the values of P and $\Delta\rho_L$ as described below. Note that according to Eq. (7) the shape of the density profile depends only on the dimensionless ratio $\gamma = LP/D$, so the units of L , P , and D can be adjusted while keeping γ constant, making the results valid in other scales, too.

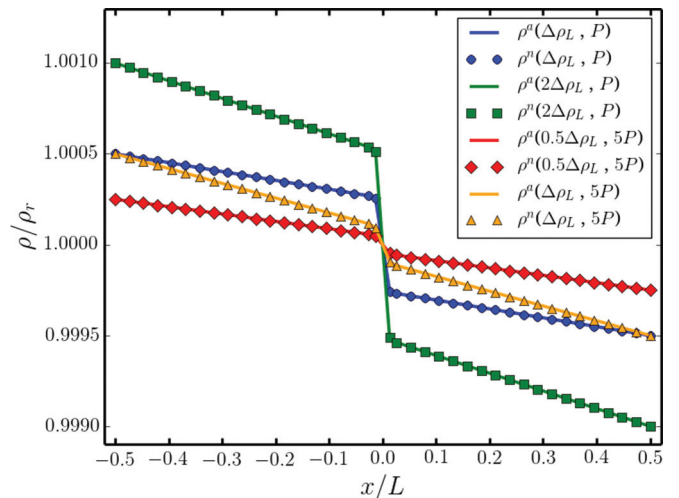


FIG. 3. Comparison of numerical and analytical concentration profiles. The reference values are $\Delta\rho_L = 10^{-3}\rho_r$ and $P = 0.05$ cm/s.

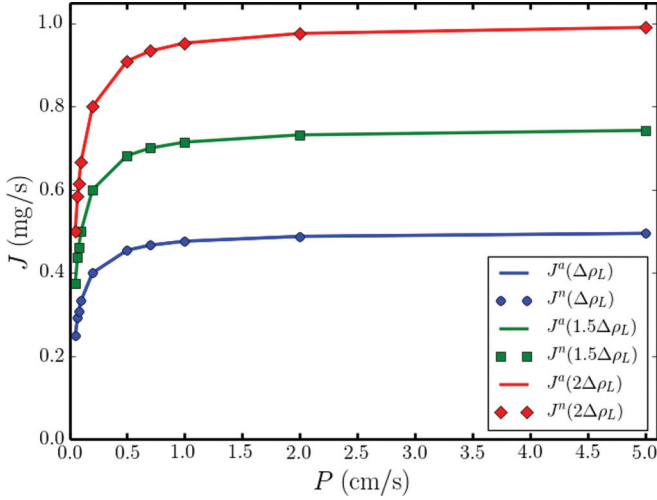


FIG. 4. Comparison of the analytical approximation for the mass flux, Eq. (12), with the flux obtained from the simulations using Eq. (17). The reference value for $\Delta\rho_L$ is $10^{-3}\rho_r$.

We performed two groups of simulations. With the first group we compared the steady-state concentration profiles obtained numerically with the analytical solution, Eqs. (6) and (7), for two different values of P and three different values of $\Delta\rho_L$. With the second group of simulations we compared the mass fluxes obtained from Eqs. (12) and (17) using three different values for $\Delta\rho_L$ and ten values of P for each $\Delta\rho_L$.

Figures 3 and 4 show the results of these simulations. From the figures it is apparent that there is an excellent agreement between the numerical and analytical solutions. In fact, the analytical solutions were reproduced with machine precision, when comparing both the concentration profiles and the mass fluxes. These results are not too surprising as the presented LB scheme for modeling diffusion across membranes is second-order accurate, based on theoretical considerations, and the benchmark is a linear configuration.

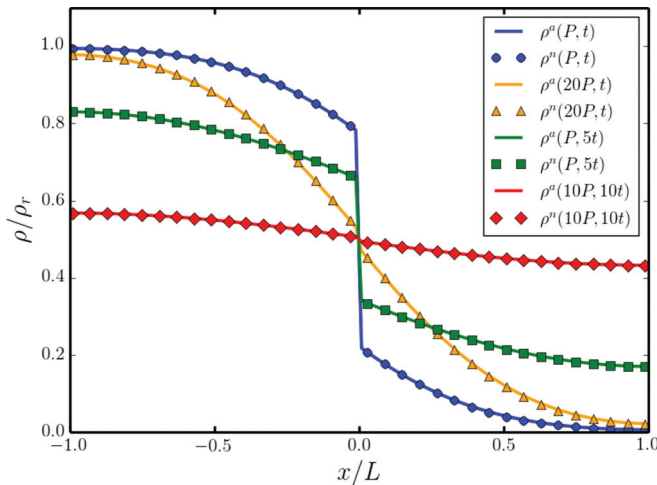


FIG. 5. Comparison of the simulated (ρ^n) and analytically determined (ρ^a) concentration profiles. The reference values are $P = 0.05$ cm/s and $t = 2$ s.

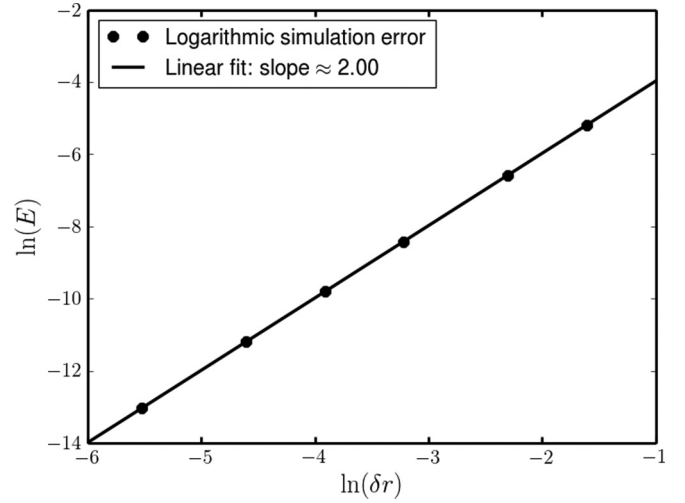


FIG. 6. The result of a convergence test for the lattice-Boltzmann partial-bounceback scheme, showing second-order convergence with respect to the lattice spacing δr .

B. Transient benchmark case

Next we considered a transient benchmark case for verifying the LB membrane scheme. When comparing the analytical solution, Eq. (8), with the simulated solution, we represented the simulation domain with 100 lattice nodes and the membrane was again located at the center of the domain. The initial concentration was $\rho_0 = \rho_r$ on the left side of the membrane and $\rho_0 = 0$ on its right side. At the borders of the simulation domain the standard bounceback rule [25] was applied (i.e., a no-flux condition). The values of D and L were fixed to the values used in the previous section, and the values of P and the time t were varied. The number of grid points determines the lattice spacing (L is fixed) as well as the discrete time step δt due to fixed D and τ^* . The permeability parameter ϕ and the number of simulation time steps were then adjusted to deliver the given P and t . The results of these comparisons are presented in Fig. 5. In each case we observed a very good agreement between the simulated and analytically determined solutions.

To numerically confirm the second-order accuracy, predicted analytically by using the Chapman-Enskog analysis, we measured the convergence rate of error with respect to the grid spacing δr . We repeated the transient simulation and varied the number of grid points in the simulations from 10 to 500. The (absolute) error was measured by comparing the analytical and simulated density values at the lattice point nearest to the membrane on the left side of it. From this experiment, we observed that the convergence rate of error is of second order in space as expected (see Fig. 6).

VII. APPLICATION OF THE LB MEMBRANE SCHEME

After a successful verification of the LB membrane scheme, we demonstrate its capability as a computational tool in a realistic research problem. Namely, we apply the scheme in a biological context, and utilize it for determining the permeability of the nuclear envelope of HeLa cells to enhanced yellow fluorescent protein (EYFP).

Proteins can travel through the nuclear envelope passively by diffusion, or they can be actively transported by proteins called karyopherins. The karyopherin-mediated active transport requires that the transported protein contains peptide signals called nuclear localization signals or nuclear export signals in the case of nuclear import or nuclear export, respectively. The green fluorescent protein (GFP) and GFP-derived fluorescent proteins, like EYFP used here, do not contain these signals and are known to be small enough to travel through the envelope passively.

The irregular shape of the cell and its nucleus, the nonuniformity of the equilibrium concentration of a molecule of interest, and movement of particles between cell organelles and their exterior are some of the problems that need to be addressed when considering the diffusion of particles within cells. These complexities usually mean that analytical methods are very difficult to utilize, and numerical methods become necessary. Instead of using a microscopic model for diffusion, like a random walker to model individual particles, it is more useful to work here on the particle density level instead, since in our approach we compare our simulations to experimentally determined densities. The connection between the particle densities and the lattice-Boltzmann distribution functions is simple (see Sec. IV) making it easy to interpret our simulations. Additionally, Eq. (16) gives us access to the permeability value from the simulation parameters utilized at the location of the nuclear envelope.

With these considerations in mind, we determine the permeability of the nuclear envelope to EYFP by comparing the measured evolution of the EYFP distribution in the cells to the evolution simulated with the lattice-Boltzmann method using different values of permeability. That is, we simulate nuclear transport in a real cellular geometry. The realistic, image-based simulation geometry is itself obtained by using fluorescence microscopy. By correlating the experimental and computational results, it is then possible to determine a permeability value for the nuclear envelope from the simulation parameters utilized.

A. Experimental setup

1. Cells and culturing

Human-carcinoma HeLa MZ cells were used in all the experiments. The cells were grown in Dulbecco's modified Eagle medium with 10% FBS, while incubated at 37°C temperature in the presence of 5% CO₂. The cells were transfected with plasmids encoding a freely diffusing yellow fluorescent protein (EYFP-N3) and a histone-bound cyan fluorescent protein (H2B-ECFP) using the TransIT-2020 reagent (Mirus Bio LLC, Madison, WI) in 5-cm glass-bottom dishes (MatTek, Ashland, MA) 24 hours before the measurements.

2. Microscopy

An Olympus FV1000 confocal microscope was used in the experiments with a 60× water-immersion objective whose numerical aperture was 1.2. The stage heater of the microscope was set to 37°C. The equilibrium distributions of EYFP and H2B-ECFP were imaged in the whole cell by taking confocal planes from the top to the bottom of the cell. The dynamics

of EYFP was imaged in one confocal plane only. The voxel size was set to (150 nm)³ in three-dimensional (3D) imaging and (150 nm)² in two-dimensional (2D) imaging. EYFP was excited using the 514-nm line of an argon laser, and H2B-ECFP using the 405-nm line of a diode laser.

The equilibrium distributions I_{eq} of EYFP and H2B-ECFP were first imaged in the whole cell using an image size of 320 by 240 pixels. The average thickness of the cells was about 80 pixels. Since the EYFP distribution that is seen with the microscope is, macroscopically speaking, in equilibrium, we needed to disturb this equilibrium in order to measure its dynamics. This was achieved using the photobleaching technique, where a high-intensity laser pulse is directed to a region in a cell, destroying the fluorescence in that area. It was observed that after the photobleaching the diffusion of EYFP back towards the equilibrium was very fast, so the process could not be imaged in the entire cell but only in one confocal plane. To further increase the acquisition speed, a smaller area of 320 by 90–100 pixels was selected such that the area contained some of the nucleus, cytoplasm, and nuclear envelope. The dynamics of EYFP was then observed in this area by first photobleaching a circular area of 1.5- μ m diameter in the nucleus using the 514-nm laser line with maximum power, and taking images with 5.2–5.5 frames per second thereafter. The imaged intensity *after* the bleaching in this one layer is called I_{exp} in the following.

B. Simulation setup

For simulations the nucleus was segmented using fluorescence data of H2B-ECFP, and the whole cell was segmented from the background using the EYFP data [see Figs. 7(a)–7(d)]. As the initial condition for the simulation we selected the EYFP distribution after the photobleaching [Figs. 7(e) and 7(f)]. Even though we imaged the photobleaching process in one confocal plane, the laser beam causes the bleached profile to extend also in the direction perpendicular to the imaged plane. We assumed that the intensity profile of the laser was constant in the z direction [12] and calculated a fractional loss of intensity, $\gamma(x, y)$, such that for the before- and after-bleach intensities the relation $I_{after} = \gamma I_{before}$ held. The whole-cell initial concentration distribution for the simulation, $I_{sim}(\mathbf{r}, t = 0)$, was then set by multiplying the intensities of the imaged equilibrium concentration of EYFP in every layer with $\gamma(x, y)$ (extrapolation of the profile in the z direction).

The cell is filled with microscopic structures which prevent the fluorophores from entering certain regions of the cell, effectively reducing the accessible volume for the fluorophores. As these structures cannot be resolved by the microscope, the measured equilibrium distribution appears to be heterogeneous and nonuniform [see Fig. 7(a)]. Due to this nonuniformity, we had to solve the diffusion equation for the dimensionless (relative) intensity, $I^*(\mathbf{r}, t = 0) = I_{sim}(\mathbf{r}, t = 0)/I_{eq}(\mathbf{r})$ [26]. Solving the equation for I_{sim} , instead of I^* , would eventually lead to a uniform equilibrium concentration, which, as mentioned above, is not correct.

For these simulations we used the standard LB scheme for diffusion with the D3Q7 discrete velocity set; parameter b was fixed to 2/7. The grid spacing δr was chosen to be the same as the voxel size of the imaged cells (150 nm). At the borders

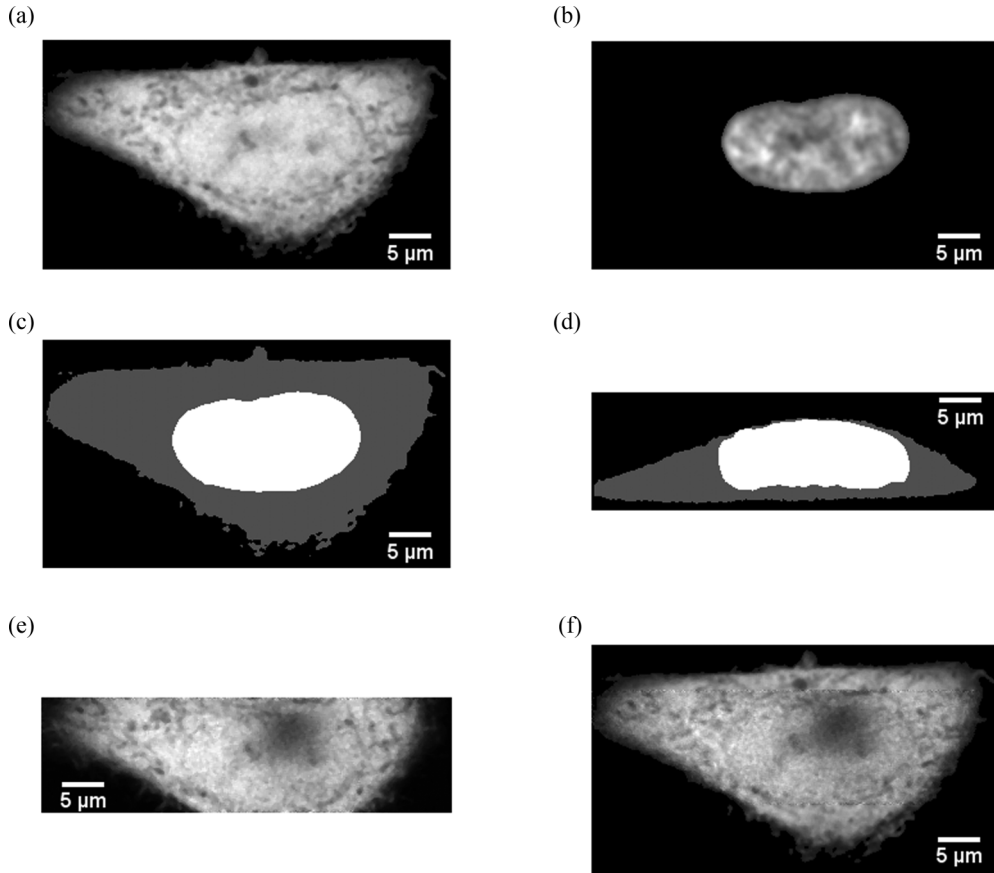


FIG. 7. (a) A confocal microscopy image showing a top cross section of the equilibrium distribution of EYFP inside a HeLa cell. (b) A confocal microscopy image of H2B-ECFP distribution in the nucleus. HB2-ECFP distribution was used to segment the nucleus from the rest of the cell and to determine the location of the nuclear envelope. (c) A cross section of a constructed cell geometry for simulations, showing the cytoplasm in gray and the nucleus in white. The nuclear envelope was constructed by applying the partial-bounceback rule between the white and gray pixels. (d) A side cross section of the cell geometry. (e) Imaged EYFP distribution after the photobleaching. The evolution of the EYFP distribution after the photobleaching was imaged in a smaller region so that the fast dynamics of EYFP could be captured with a better time resolution. (f) A cross section of the initial concentration of a simulation, constructed using the equilibrium distribution [Fig. 6(a)] and the photobleached distribution [Fig. 6(e)]. The bleached profile extends through the cell in the direction perpendicular to the image plane.

of the cell a full bounceback rule [25] was applied (i.e., a no-flux condition), and the flux through the nuclear envelope was implemented by the membrane model presented in Sec. IV. This was achieved by applying the partial-bounceback rule of Eq. (15) to a distribution function $f_i(\mathbf{r})$ if \mathbf{r} was located in the segmented nucleus (cytoplasm) and an adjacent point $\mathbf{r} + \delta r \hat{\mathbf{e}}_i$ was located on the other side of the membrane in the segmented cytoplasm (nucleus). The permeability of the envelope was assumed to be uniform, since the density of the nuclear pores is high and they are rather uniformly located over the nuclear envelope [27,28]. Furthermore, the permeability was assumed to be constant during the simulation, since the total simulated time (only a few seconds) was short.

Besides the volume exclusion effect mentioned above, the cellular structures also reduce the mobility of molecules in their vicinity [12]. Therefore we had to scale the diffusion coefficients in the cell based on the amount of volume exclusion in the imaged equilibrium distribution. Values of $\tau(\mathbf{r})$ were set based on a simple capillary model,

$$D_{\text{eff}}(\mathbf{r}) = \varepsilon(\mathbf{r})D_{\text{max}}, \quad (18)$$

where ε is a porosity parameter that was assumed to be directly proportional to fluorescence intensity in the equilibrium fluorophore distribution, that is, $\varepsilon(\mathbf{r}) = I_{\text{eq}}(\mathbf{r})/I_{\text{max}}$, where I_{max} is the maximum fluorescence intensity of EYFP in the cell. For τ this means that we had to set them according to the equation,

$$\tau^*(\mathbf{r}) = \frac{I_{\text{eq}}}{I_{\text{max}}} \left(\tau_{\text{max}}^* - \frac{1}{2} \right) + \frac{1}{2}, \quad (19)$$

where τ_{max}^* is the maximum value of τ^* in the cell, since, according to Eq. (14), $D \propto \tau^* - 1/2$. The value of τ_{max}^* can now be chosen quite freely, e.g., based on accuracy, stability, or workload considerations for the problem. We found that $\tau_{\text{max}}^* = 2$ was a good choice for our problem. Note that in our analytical considerations, we assumed that the diffusion coefficients on either side of the membrane are the same. This is strictly speaking not true in our simulations, but the gradient $\nabla D(\mathbf{r})$ is still sufficiently small to justify this assumption.

By varying ϕ , the transmission parameter for the nuclear envelope, we obtained several diffusion patterns that were analyzed and fitted to experimentally measured diffusion to yield δt as a fitting parameter. In other words, ϕ was used

to control the amount of nuclear envelope permeation in the simulation, while δt was used to connect the whole simulation to the experiment to which it was compared. This works because both D and P are inversely proportional to δt . The fitting procedure is described in the next section.

1. Data analysis

Distributions of I^* that were obtained from the simulations were compared to measured relative fluorescence of the corresponding experiments, $I_{\text{exp}}^* = I_{\text{exp}}/I_{\text{eq}}$, by calculating cross-correlation functions given by

$$\text{Cc}(\text{exp}, \text{sim}) = \sum_{x,y} \frac{[I_{\text{exp}}^*(x,y) - I_{\text{exp}}^{\text{aver}}] + [I_{\text{sim}}^*(x,y) - I_{\text{sim}}^{\text{aver}}]}{N\sigma_{\text{exp}}\sigma_{\text{sim}}},$$

where subscript ‘‘exp’’ refers to experiment and ‘‘sim’’ to simulation, $I(x,y)$ are fluorescence intensities of the pixels, I^{aver} average intensities of the images, σ the standard deviations of the images, and N is the number of pixels in the image. Notice that the simulations were conducted in the whole cell, while the experimental EYFP diffusion was only imaged in one confocal plane of the cell. For this reason, the corresponding region had to be extracted from the simulations for the comparison. For each experimental time point, the simulation time point that gave the largest cross-correlation value between the two images was determined. In this way a curve was obtained, the linearity of which was used as an indicator of the accuracy of the simulation. For the simulation that yielded the most linear curve, the value of the simulation time step δt was extracted from the slope of the curve. The values of δt and ϕ were then used in Eq. (16) to determine the nuclear envelope permeability.

C. Determination of the nuclear permeability of EYFP

We determined the nuclear envelope permeability of EYFP in HeLa cells by comparing the evolution of EYFP distribution in the cells, measured by fluorescence microscopy, to evolution simulated with different values of permeability (see Fig. 8).

Figure 9 shows that when the value of ϕ in the simulation was too high, the simulation progressed too fast compared to the experiment. Similarly, the simulation progressed too slowly when ϕ was too low. This allowed us to find an optimal

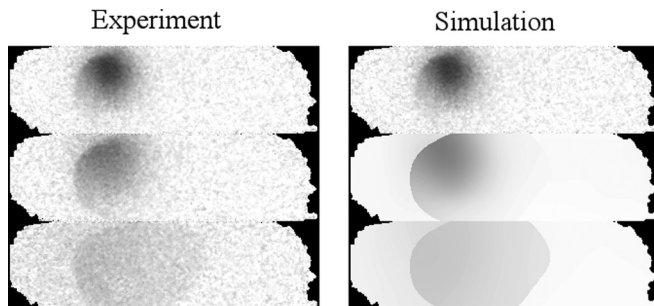


FIG. 8. A comparison of the experimental (left-hand column) and simulated (right-hand column) intensities I^* at three time points. Notice that the experimental data contains imaging noise. This is also true for the initial condition of the simulation, since it is determined from the experimental data.

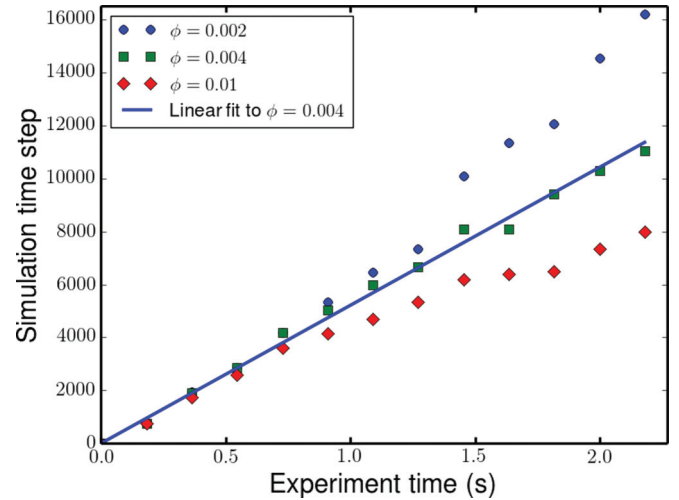


FIG. 9. Comparison of three simulations with different permeability parameters ϕ to an experiment. For every time point of the experiment a time point from the simulation was searched such that it yielded the highest cross correlation between the two. The simulation for $\phi = 0.004$ was the most linear one. The time step of the simulation can be determined from the slope of the linear fit.

ϕ , and to determine the nuclear permeability as described above.

We performed simulations for 12 cells, and the determined permeabilities varied between 0.16 and 0.98 $\mu\text{m}/\text{s}$. The average permeability and its standard deviation were $P = 0.5 \pm 0.3 \mu\text{m}/\text{s}$. The determined simulation time step, together with the used simulation parameters, allowed us to calculate also the diffusion coefficients in the cell. The determined average diffusion coefficients in the nucleus and cytoplasm were $D_{\text{nuc}}^{\text{aver}} = 27 \pm 7 \mu\text{m}^2/\text{s}$ and $D_{\text{cyt}}^{\text{aver}} = 15 \pm 4 \mu\text{m}^2/\text{s}$.

Using the solubility-diffusion model (see Introduction), $P = KD_m/w$, together with equation $A_{\text{pore}} = K/n$, where A_{pore} is the cross-sectional area of one nuclear pore channel and n is the area density of the nuclear pores, we calculated a rough estimate for the effective nuclear pore diameter. The value D_m that we used was the average of the nucleus and cytoplasm diffusion coefficients that we determined (21 $\mu\text{m}^2/\text{s}$) and the value of n was the average of values from [27,28] (25 μm^{-2}) and $w \sim 65 \text{ nm}$ [29,30]. This way we obtained the effective nuclear pore area $A_{\text{pore}} \sim 62 \text{ nm}^2$, or effective pore diameter $d_{\text{pore}} \sim 8.9 \text{ nm}$, which is in good agreement with experimental data [31,32].

D. Discussion

The average diffusion coefficients that we obtained in the nucleus and cytoplasm are close to what has been found in previous studies for EYFP and structurally very similar GFP [12,33,34]. The average diffusion coefficients are about 3–6 times less in the cellular environment than in water [34].

Previously, nuclear envelope permeabilities have been determined mostly by fitting an analytical solution to a measured average fluorescence intensity in the nucleus after photobleaching [35,36]. The solution assumes that diffusion in the nucleus and cytoplasm is fast compared to diffusion through the nuclear envelope, such that the concentrations

in the nucleus and cytoplasm are approximately uniform. A previously reported value of the permeability for enhanced green fluorescent protein EGFP, determined in this manner, is $0.011 \mu\text{m/s}$ in COS7 cells [36]. We obtained a clearly higher permeability value and some reasons for the discrepancy are discussed below.

Besides the fact that the permeability of the nuclear envelope is probably somewhat different between two cell lines, an additional explanation might be that the above approximation used in Refs. [35,36] exaggerates the flux through the nuclear envelope (since it assumes a higher concentration difference over the membrane than there actually is). This leads to an underestimation of the nuclear envelope permeability that is obtained by fitting the model to an experiment. Another assumption used in [36] was that the cytoplasm concentration stayed constant, i.e., the cytoplasm volume was large compared to that of the nucleus. This approximation also further underestimates the permeability.

Regions of the cell where these approximations prove especially problematic (for cells on a hard substrate) are the bottom and the top of the nucleus. There the nucleus is usually very close to the plasma membrane of the cell [see Fig. 7(d)] and, because of the restricted space, it is more difficult for the cell to replace permeated molecules to retain an efficient concentration difference between the two compartments.

VIII. CONCLUSION

We reported here an analysis of modeling diffusion through semipermeable membranes. We intentionally avoided assigning intrinsic properties such as the diffusion coefficient and particle concentration to the membrane itself, but rather treated the membrane as a semipermeable boundary between two regions. In particular, the transmission boundary conditions were imposed at the membrane. This approach is especially useful in cases where the membrane is thin compared to the overall size of the system. To facilitate a numerical modeling of diffusion through thin membranes, we then presented various discrete treatments of the transmission boundary conditions.

First we presented a direct discretization of the conditions at the macroscopic level of description. A mesoscopic discretization, the partial-bounceback scheme, was then shown to be a consistent, alternative approach for enforcing the transmission boundary conditions. Furthermore, an expression for the permeability derived for a mesoscopic LB scheme, was shown to be in accordance with a microscopic, single-particle stochastic diffusion model. Hence, the mesoscopic parameter ϕ provided a bridge between the microscopic and macroscopic descriptions, and could, for example, be used as a coupling parameter between microscopic and macroscopic solvers in a multiscale simulation effort. Moreover, the proposed lattice-Boltzmann scheme for membrane diffusion is directly applicable to advection-diffusion problems as well as to a hydrodynamic transport across a membrane.

To demonstrate the applicability of the membrane scheme, we simulated nuclear transport in a real cellular geometry imaged by fluorescence microscopy. In this application of the LB membrane scheme, together with a prescribed computational procedure, we numerically determined a value for the permeability of the nuclear envelope to EYFP. Since the

number of methods to study nuclear envelope permeability has been limited, our method has the potential to be an important addition to the existing tools.

ACKNOWLEDGMENT

This work was financed by the Jane and Aatos Erkkö foundation.

APPENDIX A: ANALYTICAL SOLUTION TO THE DIFFUSION PROBLEM

Consider a diffusion equation,

$$\frac{\partial \rho}{\partial t}(x,t) - D \frac{\partial^2 \rho}{\partial x^2}(x,t) = 0, \quad (A1)$$

$$x \in [-L,0) \cup (0,L], \quad t > 0,$$

with the boundary conditions

$$\frac{\partial \rho}{\partial x}(L,t) = \frac{\partial \rho}{\partial x}(-L,t) = 0, \quad (A2)$$

and transmission conditions

$$D \frac{\partial \rho}{\partial x}(0-,t) = -P(\rho(0-,t) - \rho(0+,t)),$$

$$\frac{\partial \rho}{\partial x}(0+,t) = \frac{\partial \rho}{\partial x}(0-,t), \quad (A3)$$

and initial condition

$$\rho(x,0) = \begin{cases} 1, & -L \leq x \leq 0 \\ 0, & 0 < x \leq L. \end{cases} \quad (A4)$$

Substitution

$$\xi = \frac{x}{L}, \quad \bar{t} = \frac{tD}{L^2}$$

gives us a dimensionless form of the problem Eqs. (A1)–(A4),

$$\frac{\partial \rho}{\partial \bar{t}}(\xi, \bar{t}) - \frac{\partial^2 \rho}{\partial \xi^2} = 0, \quad \xi \in [-1,0) \cup (0,1],$$

$$\frac{\partial \rho}{\partial \xi}(\pm 1, \bar{t}) = 0,$$

$$\frac{\partial \rho}{\partial \xi}(0+, \bar{t}) = \frac{\partial \rho}{\partial \xi}(0-, \bar{t}) = -\gamma(\rho(0-, \bar{t}) - \rho(0+, \bar{t})),$$

$$\rho(\xi, 0) = \begin{cases} 1, & -1 \leq \xi \leq 0 \\ 0, & 0 < \xi \leq 1, \end{cases}$$

where $\gamma = LP/D$. This problem can be solved by separation of variables, $\rho(\xi, \bar{t}) = v(\xi)w(\bar{t})$. For function v we find an eigenvalue problem,

$$v''(\xi) + \mu^2 v(\xi) = 0, \quad \xi \in [-1,0) \cup (0,1],$$

$$v'(1) = v'(-1) = 0, \quad (A5)$$

$$v'(0+) = v'(0-) = -\gamma(v(0-) - v(0+)),$$

and w satisfies the equation,

$$w'(\bar{t}) = -\mu^2 w(\bar{t}).$$

Solution of the first equation in Eq. (A5), which satisfies the boundary conditions at $\xi = \pm 1$, can be expressed in the form,

$$v(\xi) = \begin{cases} A \cos(\mu(\xi + 1)), & -1 \leq \xi < 0 \\ B \cos(\mu(\xi - 1)), & 0 < \xi \leq 1. \end{cases}$$

The transmission condition in Eq. (A5) leads to an eigenvalue equation,

$$\mu \sin \mu (\mu \sin \mu - 2\gamma \cos \mu) = 0. \quad (\text{A6})$$

Eigenvalues μ_{2k} are given by

$$\mu_{2k} = k\pi, \quad k = 0, 1, \dots,$$

while μ_{2k+1} are given by the solutions of the equation,

$$\tan \mu_{2k+1} = \frac{2\gamma}{\mu_{2k+1}}, \quad k\pi < \mu_{2k+1} < k\pi + \frac{\pi}{2}.$$

The corresponding eigenfunctions are given by

$$v_{2k}(\xi) = \cos(k\pi\xi),$$

$$v_{2k+1}(\xi) = \text{sgn}(\xi) \cos(\mu_{2k+1}\xi) + \frac{2\gamma}{\mu_{2k+1}} \sin(\mu_{2k+1}\xi).$$

From general Sturm-Liouville theory we know that these eigenfunctions are orthogonal with respect to the L^2 inner product, and they form a complete (orthogonal) basis [37]. The solution of the problem of Eq. (A6) can be expressed in the form,

$$\rho(\xi, \tilde{\tau}) = \frac{1}{2} - \sum_{k=0}^{\infty} \frac{2\gamma e^{-\mu_{2k+1}^2 \tilde{\tau}}}{\mu_{2k+1}^2 + 4\gamma^2 + 2\gamma} \times \left(\text{sgn}(\xi) \cos(\mu_{2k+1}\xi) + \frac{2\gamma}{\mu_{2k+1}} \sin(\mu_{2k+1}\xi) \right).$$

APPENDIX B: LATTICE-BOLTZMANN SCHEME OF THE PARTIAL-BOUNCEBACK METHOD

Pure diffusion processes, involving isotropic diffusion, can be simulated, e.g., by using the standard lattice-Boltzmann evolution equation with the BGK-collision operator [11]:

$$f_i(\mathbf{r} + \delta t \mathbf{c}_i, t + \delta t) = f_i(\mathbf{r}, t) - \frac{\delta t}{\tau} [f_i(\mathbf{r}, t) - f_i^{\text{eq}}(\rho)], \quad i = 0, \dots, q-1, \quad (\text{B1})$$

where τ is a relaxation time, ρ denotes the local density at a given instant, and suitable weight coefficients for the equilibrium function, $f_i^{\text{eq}} = w_i \rho$, are given in Table I. The lattice spacing δr , and discrete time step δt , define a reference

TABLE I. Lattice-Boltzmann stencils for simulating diffusion. The second column specifies the dimensionless discrete velocity vectors (relevant permutations are implied). The weight coefficients w_0 and w_1 are associated with the zero and nonzero velocity vectors, respectively.

Stencil	\mathbf{c}_i^*	w_0	w_1	Domain
D1Q3	$\{0, \pm 1\}$	$1 - b$	$b/2$	$0 < b \leq 1$
D2Q5	$\{(0,0), (\pm 1,0)\}$	$1 - 2b$	$b/2$	$0 < b \leq 1/2$
D3Q7	$\{(0,0,0), (\pm 1,0,0)\}$	$1 - 3b$	$b/2$	$0 < b \leq 1/3$

velocity, $c_r = \delta r / \delta t$, and $\mathbf{c}_i = c_r \mathbf{c}_i^*$. With the stencils of Table I, the first few moments of the discrete equilibrium function are given by

$$\sum_i f_i^{\text{eq}} = \rho, \quad \sum_i c_{i,\alpha} f_i^{\text{eq}} = 0, \quad \sum_i c_{i,\alpha} c_{i,\beta} f_i^{\text{eq}} = b c_r^2 \rho \delta_{\alpha\beta}.$$

The diffusion coefficient can be derived, e.g., by the Chapman-Enskog procedure:

$$D_{\text{bulk}} = \left(\tau - \frac{\delta t}{2} \right) b c_r^2.$$

1. Chapman-Enskog analysis of LBGK

First, the left-hand side of Eq. (B1) is expanded as a Taylor series up to second-order terms:

$$(\partial_t + c_{i,\alpha} \partial_\alpha) f_i + \frac{\delta t}{2} (\partial_t + c_{i,\alpha} \partial_\alpha)^2 f_i = -\frac{1}{\tau} (f_i - f_i^{\text{eq}}). \quad (\text{B2})$$

Then, the usual expansions with respect to the small parameter ϵ are introduced such that

$$\partial_t = \epsilon \partial_t^{(1)} + \epsilon^2 \partial_t^{(2)}, \quad \partial_\alpha = \epsilon \partial_\alpha^{(1)}, \quad f_i = f_i^{(0)} + \epsilon f_i^{(1)} + \epsilon^2 f_i^{(2)}. \quad (\text{B3})$$

In addition, the solubility condition, $\sum_i f_i^{(k)} = 0$, $k \geq 1$, is assumed. These expansions are substituted into the Taylor expansion, Eq. (B2), and terms of equal order in ϵ are collected:

$$\mathcal{O}(\epsilon^0): 0 = -\frac{1}{\tau} (f_i^{(0)} - f_i^{\text{eq}}) \Rightarrow f_i^{(0)} = f_i^{\text{eq}}, \quad \rho^{(0)} = \rho, \quad j_\alpha^{(0)} = 0, \quad (\text{B4})$$

$$\mathcal{O}(\epsilon^1): (\partial_t^{(1)} + c_{i,\alpha} \partial_\alpha^{(1)}) f_i^{(0)} = -\frac{1}{\tau} f_i^{(1)}, \quad (\text{B5})$$

$$\begin{aligned} \mathcal{O}(\epsilon^2): & \partial_t^{(2)} f_i^{(0)} + (\partial_t^{(1)} + c_{i,\alpha} \partial_\alpha^{(1)}) f_i^{(1)} \\ & + \frac{\delta t}{2} (\partial_t^{(1)} + c_{i,\alpha} \partial_\alpha^{(1)})^2 f_i^{(0)} = -\frac{1}{\tau} f_i^{(2)} \\ \Rightarrow & \partial_t^{(2)} f_i^{(0)} + \left(1 - \frac{\delta t}{2\tau} \right) (\partial_t^{(1)} + c_{i,\alpha} \partial_\alpha^{(1)}) f_i^{(1)} \\ = & -\frac{1}{\tau} f_i^{(2)}. \end{aligned} \quad (\text{B6})$$

The last equation is obtained after utilization of Eq. (B5). By computing the zeroth moments of Eqs. (B5) and (B6), and summing up the results, we find that

$$\partial_t \rho = -\left(1 - \frac{\delta t}{2\tau} \right) \partial_\alpha j_\alpha^{(1)}.$$

An expression for $j_\alpha^{(1)}$ is obtained by computing the first moment of Eq. (B5):

$$j_\alpha^{(1)} = -\tau b c_r^2 \partial_\alpha \rho. \quad (\text{B7})$$

Using these results, we arrive at the diffusion equation,

$$\partial_t \rho = \underbrace{\left(\tau - \frac{\delta t}{2} \right) b c_r^2}_{D_{\text{bulk}} :=} \partial_\alpha^2 \rho.$$

2. The partial halfway-bounceback scheme

The membrane boundary condition reported in Ref. [14] can be implemented in a lattice-Boltzmann scheme by introducing a partial halfway-bounceback rule for the distributions crossing the membrane,

$$f_i(\mathbf{r} + \delta t \mathbf{c}_i, t + \delta t) = \phi f_i(\mathbf{r}, t) + (1 - \phi) f_{-i}(\mathbf{r} + \delta t \mathbf{c}_i, t), \quad (\text{B8})$$

where subscript $-i$ denotes an opposite direction, i.e., $\mathbf{c}_{-i} = -\mathbf{c}_i$. Membrane is located halfway between adjacent lattice nodes, and, ideally, ϕ represents the relative area of the membrane, which allows for diffusive transport. In general,

$$f_i\left(\mathbf{r} + \frac{\delta t}{2} \mathbf{c}_i, t + \frac{\delta t}{2}\right) = \phi f_i^{\text{post}}\left(\mathbf{r} - \frac{\delta t}{2} \mathbf{c}_i, t - \frac{\delta t}{2}\right) + (1 - \phi) f_{-i}^{\text{post}}\left(\mathbf{r} + \frac{\delta t}{2} \mathbf{c}_i, t - \frac{\delta t}{2}\right),$$

the right-hand side involving distributions after the latest relaxation process. Next we substitute these post-relaxation variables with explicit expressions according to the BGK operator:

$$f_i\left(\mathbf{r} + \frac{\delta t}{2} \mathbf{c}_i, t + \frac{\delta t}{2}\right) = \phi \left[f_i - \frac{\delta t}{\tau} f_i^{\text{neq}} \right] \left(\mathbf{r} - \frac{\delta t}{2} \mathbf{c}_i, t - \frac{\delta t}{2} \right) + (1 - \phi) \left[f_{-i} - \frac{\delta t}{\tau} f_{-i}^{\text{neq}} \right] \left(\mathbf{r} + \frac{\delta t}{2} \mathbf{c}_i, t - \frac{\delta t}{2} \right).$$

Then we expand (Taylor series) both sides of the resulting equation around (\mathbf{r}, t) :

$$\begin{aligned} \left[1 + \frac{\delta t}{2} (\partial_t + c_{i,\alpha} \partial_\alpha) + \frac{\delta t^2}{8} (\partial_t + c_{i,\alpha} \partial_\alpha)^2 \right] f_i &= \phi \left[1 - \frac{\delta t}{2} (\partial_t + c_{i,\alpha} \partial_\alpha) + \frac{\delta t^2}{8} (\partial_t + c_{i,\alpha} \partial_\alpha)^2 \right] \left(f_i - \frac{\delta t}{\tau} f_i^{\text{neq}} \right) \\ &+ (1 - \phi) \left[1 - \frac{\delta t}{2} (\partial_t - c_{i,\alpha} \partial_\alpha) + \frac{\delta t^2}{8} (\partial_t - c_{i,\alpha} \partial_\alpha)^2 \right] \left(f_{-i} - \frac{\delta t}{\tau} f_{-i}^{\text{neq}} \right). \end{aligned} \quad (\text{B9})$$

The usual expansions, Eq. (B3), with respect to the small parameter ϵ are introduced together with the solubility condition, $\sum_i f_i^{(k)} = 0$. After substituting these expansions into Eq. (B9) and collecting terms of equal order in ϵ , we find that

$$\begin{aligned} \mathcal{O}(\epsilon^0) : f_i^{(0)} &= \phi \left[f_i^{(0)} - \frac{\delta t}{\tau} (f_i^{(0)} - f_i^{\text{eq}}) \right] + (1 - \phi) \left[f_{-i}^{(0)} - \frac{\delta t}{\tau} (f_{-i}^{(0)} - f_{-i}^{\text{eq}}) \right], \\ \mathcal{O}(\epsilon^1) : f_i^{(1)} + \frac{\delta t}{2} (\partial_t^{(1)} + c_{i,\alpha} \partial_\alpha^{(1)}) f_i^{(0)} &= \phi \left[\left(1 - \frac{\delta t}{\tau} \right) f_i^{(1)} - \frac{\delta t}{2} (\partial_t^{(1)} + c_{i,\alpha} \partial_\alpha^{(1)}) f_i^{(0)} \right] + (1 - \phi) \left[\left(1 - \frac{\delta t}{\tau} \right) f_{-i}^{(1)} - \frac{\delta t}{2} (\partial_t^{(1)} - c_{i,\alpha} \partial_\alpha^{(1)}) f_{-i}^{(0)} \right], \\ \mathcal{O}(\epsilon^2) : f_i^{(2)} + \frac{\delta t}{2} \partial_t^{(2)} f_i^{(0)} + \frac{\delta t}{2} (\partial_t^{(1)} + c_{i,\alpha} \partial_\alpha^{(1)}) f_i^{(1)} + \frac{\delta t^2}{8} (\partial_t^{(1)} + c_{i,\alpha} \partial_\alpha^{(1)})^2 f_i^{(0)} &= \phi \left(1 - \frac{\delta t}{\tau} \right) \left[f_i^{(2)} - \frac{\delta t}{2} (\partial_t^{(1)} + c_{i,\alpha} \partial_\alpha^{(1)}) f_i^{(1)} \right] + \phi \left[\frac{\delta t^2}{8} (\partial_t^{(1)} + c_{i,\alpha} \partial_\alpha^{(1)})^2 f_i^{(0)} - \frac{\delta t}{2} \partial_t^{(2)} f_i^{(0)} \right] \\ &+ (1 - \phi) \left(1 - \frac{\delta t}{\tau} \right) \left[f_{-i}^{(2)} - \frac{\delta t}{2} (\partial_t^{(1)} - c_{i,\alpha} \partial_\alpha^{(1)}) f_{-i}^{(1)} \right] + (1 - \phi) \left[\frac{\delta t^2}{8} (\partial_t^{(1)} - c_{i,\alpha} \partial_\alpha^{(1)})^2 f_{-i}^{(0)} - \frac{\delta t}{2} \partial_t^{(2)} f_{-i}^{(0)} \right]. \end{aligned}$$

In the subsequent treatments we will utilize

$$\sum_i \mathbf{c}_i^{2k} f_{-i} = \sum_i \mathbf{c}_i^{2k} f_i, \quad \sum_i \mathbf{c}_i^{2k+1} f_{-i} = - \sum_i \mathbf{c}_i^{2k+1} f_i.$$

Note also that $f_{-i}^{\text{eq}} = f_i^{\text{eq}}$.

however, ϕ is only a simulation parameter, which allows control of the diffusive transport across the membrane, i.e., provides control over the permeability of the membrane or its effective diffusion coefficient. Using the Chapman-Enskog analysis, for example, it can be shown that the above modification of the streaming step gives rise to the following effective diffusion coefficient for the membrane,

$$D_{\text{eff}}^{\text{pbb}} = \frac{\phi}{(1 - \phi)} \frac{b}{2} \delta t c_r^2.$$

Furthermore, membrane permeability can be defined as $P^{\text{pbb}} = D_{\text{eff}}^{\text{pbb}} / \delta r$. This relation, where the lattice spacing δr does not represent the actual membrane thickness h , is discussed below.

3. Chapman-Enskog analysis of the partial-bounceback scheme

First we shift Eq. (B8) along the characteristics:

a. Zeroth-order terms

We continue by first considering the ϵ^0 equation. After simple manipulations we find that

$$\begin{aligned} (1 - \phi) f_i^{(0)} - \frac{\delta t}{\tau} (f_i^{(\text{eq})} - \phi f_i^{(0)}) \\ = (1 - \phi) f_{-i}^{(0)} - \frac{\delta t}{\tau} (1 - \phi) f_{-i}^{(0)}, \end{aligned}$$

which is identically true whenever $f_i^{(0)} = f_i^{\text{eq}}$. This in turn implies that

$$\begin{aligned} \sum_i f_i^{(0)} &= \rho, \\ \sum_i c_{i,\alpha} f_i^{(0)} &= 0, \\ \sum_i c_{i,\alpha} c_{i,\beta} f_i^{(0)} &= b c_r^2 \rho \delta_{\alpha\beta}, \\ \sum_i c_{i,\alpha} c_{i,\beta} c_{i,\gamma} f_i^{(0)} &= 0. \end{aligned}$$

b. First-order terms

Now, based on the results above, we can compute the zeroth moment of the ϵ^1 equation:

$$\partial_t^{(1)} \rho = 0. \quad (\text{B10})$$

The first moment can be used to give an expression for the flux:

$$\begin{aligned} j_\alpha^{(1)} &= - \left[\frac{\phi \tau}{(2\tau - \delta t)(1 - \phi) + \phi \delta t} \right] \delta t c_r^2 b \partial_\alpha \rho \\ &= - \left[1 - \frac{(2\tau - \delta t)(1 - \phi)}{(2\tau - \delta t)(1 - \phi) + \phi \delta t} \right] \tau c_r^2 b \partial_\alpha \rho \\ &= - \left[1 - \frac{1}{1 + \frac{\phi \delta t}{(2\tau - \delta t)(1 - \phi)}} \right] \tau c_r^2 b \partial_\alpha \rho. \end{aligned}$$

The diffusion coefficient in the bulk was derived above as $D = (2\tau - \delta t) c_r^2 b / 2$. Using this result we find further that

$$j_\alpha^{(1)} = - \left[1 - \frac{1}{1 + \frac{\phi \delta t c_r^2 b}{2(1 - \phi)}} \right] \tau c_r^2 b \partial_\alpha \rho.$$

This expression for the flux clearly suggests a new variable:

$$D_{\text{memb}}^{\text{eff}} := \frac{\phi}{2(1 - \phi)} \delta t c_r^2 b,$$

which we will refer to in the following as the effective diffusion coefficient of the membrane. Moreover, this coefficient is related to its permeability P via

$$P := \frac{D_{\text{memb}}^{\text{eff}}}{\delta r}. \quad (\text{B11})$$

In order to simplify the expressions further, we define $\lambda \equiv D_{\text{memb}}^{\text{eff}} / D$. Expression for the flux can now be written in the

form,

$$j_\alpha^{(1)} = - \left[1 - \frac{1}{\underbrace{1 + \lambda}_{\text{resistance}}} \right] \tau c_r^2 b \partial_\alpha \rho. \quad (\text{B12})$$

It is instructive to compare the flux of Eq. (B12) across the membrane with the flux in the bulk as given in Eq. (B7). These expressions are otherwise identical except that the membrane flux involves a resistance term. For example, when the ratio of the diffusion coefficients approaches infinity the resistance vanishes. On the other hand, the flux vanishes when the ratio approaches zero. In addition, when the diffusion coefficients are equal, resistance obtains a value that is halfway between the extremes.

c. Second-order terms

It remains to compute the zeroth moment of the ϵ^2 equation:

$$\partial_t^{(2)} \rho = - \frac{(2\tau - \delta t)}{2\tau} \partial_\alpha^{(1)} j_\alpha^{(1)}. \quad (\text{B13})$$

d. Macroscopic equation

By combining Eqs. (B10), (B12), and (B13), diffusive transport across the membrane can be described with the following diffusion equation:

$$\partial_t \rho = \left[1 - \frac{1}{1 + \lambda} \right] D \partial_\alpha^2 \rho. \quad (\text{B14})$$

APPENDIX C: THE SNAPPING-OUT BROWNIAN MOTION AND MICROSCOPIC PERMEABILITY

Perhaps the simplest model of diffusion through a semipermeable membrane is a one-dimensional random walk in discrete space and time with a special site for the membrane. Such a walker takes steps to the left and right with equal probability except at the special site, where it either goes through the membrane (with probability $\phi/2$), or is reflected back with probability $1 - \phi/2$). Hence the membrane vanishes in the limit $\phi \rightarrow 1$ (i.e., fraction of pores $\rightarrow 1$). If N_t denotes the number of collisions with the membrane up to time t , the first-passage time through the membrane obeys

$$P(T > t \mid N_t = n) = (1 - \phi/2)^n, \quad (\text{C1})$$

so the number of visits to the membrane site exceeds a geometric random variable with parameter $\phi/2$ at the time of first passage through the membrane. In other words, the mean number of visits N_T to the special site up to and including the first passage equals $2/\phi$. In particular, two visits on the average are needed to cross a completely permeable membrane (limit $\phi \rightarrow 1$), and the required number of visits diverges proportional to the first inverse power of ϕ as $\phi \rightarrow 0$.

Next we consider a microscopic model continuous in space and time, the probability density of which satisfies the macroscopic diffusion equation Eq. (A1) with the flux boundary condition, Eq. (A3). Following preprint [23], we define the (one-dimensional) snapping-out Brownian motion X_t to be a process on the real line that obeys the usual Brownian dynamics except at the origin where the membrane

is located. Passing through the membrane consists of a single rate-limiting step given that the particle is performing a search at the immediate vicinity of the membrane (this corresponds to a reaction distance in chemical-reaction applications). The amount of time spent performing the search is measured by the local time,

$$L_t = \lim_{\epsilon \rightarrow 0} \frac{1}{2\epsilon} \int_0^t I(-\epsilon < X_s < \epsilon) ds, \quad (\text{C2})$$

at the membrane, and hence the probability that the first-passage time T through the membrane is greater than t (i.e., the particle has not passed through the membrane before that) equals

$$P(T > t | L_t) = \exp\left(-\frac{L_t}{\tau_c}\right), \quad (\text{C3})$$

where $\tau_c = \lim_{w \rightarrow 0} w/D(w)$ is the characteristic time scale that depends on the membrane (w is the membrane width). We remark that finding τ_c directly from its definition as a limit would require a model for the microscopic structure of

the interface. Instead, we now relate time scale τ_c to the pore fraction ϕ by analogy to the random walk. In particular, the number of visits to the membrane site can be considered as the local time of the random walk at the membrane (see Ref. [38] for a convergence proof), and therefore τ_c should diverge as $\sim 1/\phi$ in the limit $\phi \rightarrow 0$. On the other hand, the first passage can occur immediately upon first contact with the membrane (the first time that the local time $L_t > 0$). In particular, this must hold true in the limit of a completely permeable membrane, so we can assume that $\tau_c \rightarrow 0$ as $\phi \rightarrow 1$. The only sensible function of ϕ satisfying these requirements is $\tau_c = 1/\phi - 1$. Hence the microscopic permeability, defined as the inverse of the mean first passage time, coincides with the macroscopic permeability provided by the Chapman-Enskog analysis:

$$P_{\text{micro}} := \frac{1}{\tau_c} \propto \frac{\phi}{1-\phi} \propto P_{\text{macro}}. \quad (\text{C4})$$

-
- [1] A. Hoelz, E. W. Debler, and G. Blobel, *Annu. Rev. Biochem.* **80**, 613 (2011).
- [2] K. B. Petrotos and H. N. Lazarides, *J. Food Eng.* **49**, 201 (2001).
- [3] D. Li and H. Wang, *J. Mater. Chem.* **20**, 4551 (2010).
- [4] J. F. Nagle, J. C. Mathai, M. L. Zeidel, and S. Tristram-Nagle, *J. Gen. Physiol.* **131**, 77 (2008).
- [5] G. Parisio, M. Stocchero, and A. Ferrarini, *J. Chem. Theory Comput.* **9**, 5236 (2013).
- [6] R. Benzi, S. Succi, and M. Vergassola, *Phys. Rep.* **222**, 145 (1992).
- [7] C. K. Aidun and J. R. Clausen, *Annu. Rev. Fluid Mech.* **42**, 439 (2010).
- [8] D. S. Novikov, E. Fieremans, J. H. Jensen, and J. A. Helpen, *Nature Phys.* **7**, 508 (2011).
- [9] J. E. Tanner, *J. Chem. Phys.* **69**, 1748 (1978).
- [10] O. K. Dudko, A. M. Berezhkovskii, and G. H. Weiss, *J. Chem. Phys.* **121**, 11283 (2004).
- [11] D. Wolf-Gladrow, *J. Stat. Phys.* **79**, 1023 (1995).
- [12] T. Kühn, T. O. Ihalainen, J. Hyväluoma, N. Dross, S. F. Willman, J. Langowski, M. Vihinen-Ranta, and J. Timonen, *PLoS ONE* **6**, e22962 (2011).
- [13] B. Servan-Camas and F. T.-C. Tsai, *J. Comput. Phys.* **228**, 236 (2009).
- [14] T. Kosztolowicz and S. Mrówczyński, *Acta Phys. Pol. B* **32**, 217 (2001).
- [15] O. Dardis and J. McCloskey, *Phys. Rev. E* **57**, 4834 (1998).
- [16] D. T. Thorne and M. C. Sukop, *Developments in Water Science* **55**, 1549 (2004).
- [17] S. D. C. Walsh, H. Burwinkle, and M. O. Saar, *Computers & Geosciences* **35**, 1186 (2009).
- [18] H. Yoshida and H. Hayashi, *J. Stat. Phys.* **155**, 277 (2014).
- [19] K. Han, Y. T. Feng, and D. R. J. Owen, *International Journal of Thermal Sciences* **47**, 1276 (2008).
- [20] S. Succi, *Phys. Rev. Lett.* **89**, 064502 (2002).
- [21] M. Sbragaglia and S. Succi, *Phys. Fluids* **17**, 093602 (2005).
- [22] I. Karatzas and S. E. Shreve, *Brownian Motion and Stochastic Calculus*, 2nd ed. (Springer, New York, 1998).
- [23] A. Lejay [<https://hal.inria.fr/hal-00781447v4>].
- [24] B. P. English, W. Min, A. M. van Oijen, K. T. Lee, G. Luo, H. Sun, B. J. Cherayil, S. C. Kou, and X. S. Xie, *Nature Chem. Biol.* **2**, 87 (2006).
- [25] S. Succi, *The Lattice Boltzmann Equation for Fluid Dynamics and Beyond* (Oxford University Press, Oxford, 2001).
- [26] M. H. Ernst, J. Machta, J. R. Dorfman, and H. van Beijeren, *J. Stat. Phys.* **34**, 477 (1984).
- [27] P. Comes and W. W. Franke, *Z. Zellforsch.* **107**, 240 (1970).
- [28] K. Maeshima, H. Iino, S. Hihara, T. Funakoshi, A. Watanabe, M. Nishimura, R. Nakatomi, K. Yahata, F. Imamoto, T. Hashikawa, H. Yokota, and N. Imamoto, *Nat. Struct. Mol. Biol.* **17**, 1065 (2010).
- [29] W. W. Franke, *Int. Rev. Cytol. Suppl.* **4**, 71 (1974).
- [30] C. W. Akey and M. Radermacher, *J. Cell. Biol.* **122**, 1 (1993).
- [31] P. L. Paine, *J. Cell Biol.* **66**, 652 (1975).
- [32] R. Peters, *EMBO J.* **3**, 1831 (1984).
- [33] J. Braga, J. M. P. Desterro, and M. Carmo-Fonseca, *Mol. Biol. Cell* **15**, 4749 (2004).
- [34] E. O. Potma, W. P. de Boeij, L. Bosgraaf, J. Roelofs, P. J. M. van Haastert, and D. A. Wiersma, *Biophys. J.* **81**, 2010 (2001).
- [35] R. Peters, *J. Biol. Chem.* **258**, 11427 (1983).
- [36] X. B. Wei, V. G. Henke, C. Strübing, E. B. Brown, and D. E. Clapham, *Biophys. J.* **84**, 1317 (2003).
- [37] A. Wang, J. Sun, and P. Gao, *J. Spectral Math. Appl.* **1** (2006).
- [38] A. N. Borodin, *Theory Probab. Appl.* **26**, 758 (1981).

II


HERPES SIMPLEX VIRUS 1 INDUCES EGRESS CHANNELS THROUGH MARGINALIZED HOST CHROMATIN

by

Myllys, M., Ruokolainen, V., Aho, V., Smith, E. A., Hakanen, S., Peri, P., Salvetti, A.,
Timonen, J., Hukkanen, V., Larabell, C. A. & Vihinen-Ranta, M.

Scientific Reports, 6:28844, 2016

SCIENTIFIC REPORTS



OPEN

Herpes simplex virus 1 induces egress channels through marginalized host chromatin

Received: 01 March 2016

Accepted: 24 May 2016

Published: 28 June 2016

Markko Myllys^{1,*}, Visa Ruokolainen^{2,*}, Vesa Aho¹, Elizabeth A. Smith^{3,4}, Satu Hakanen², Piritta Peri⁵, Anna Salvetti^{6,7,8,9}, Jussi Timonen^{1,10}, Veijo Hukkanen⁵, Carolyn A. Larabell^{3,5} & Maija Vihinen-Ranta²

Lytic infection with herpes simplex virus type 1 (HSV-1) induces profound modification of the cell nucleus including formation of a viral replication compartment and chromatin marginalization into the nuclear periphery. We used three-dimensional soft X-ray tomography, combined with cryogenic fluorescence, confocal and electron microscopy, to analyse the transformation of peripheral chromatin during HSV-1 infection. Our data showed an increased presence of low-density gaps in the marginalized chromatin at late infection. Advanced data analysis indicated the formation of virus-nucleocapsid-sized (or wider) channels extending through the compacted chromatin of the host. Importantly, confocal and electron microscopy analysis showed that these gaps frequently contained viral nucleocapsids. These results demonstrated that HSV-1 infection induces the formation of channels penetrating the compacted layer of cellular chromatin and allowing for the passage of progeny viruses to the nuclear envelope, their site of nuclear egress.

Herpes viruses target the cell nucleus because of their need for the cellular DNA reproduction machinery. The nuclear entry of viral DNA is followed by the nuclear accumulation of viral proteins and replication of viral DNA, leading to the formation of viral replication compartments (VRCs). Electron microscopy and confocal microscopy studies have illustrated how profoundly these viruses transform the nuclear structure so as to optimise their multiplication^{1–5}.

During cellular entry the nucleocapsid of herpes simplex virus type-1 (HSV-1) undergoes partial disassembly at the nuclear pore complex (NPC), followed by viral genome delivery via the pore^{6,7}. When the infection proceeds, the VRCs emerge as distinct nuclear foci, which subsequently undergo fusion and expansion into a large, globular VRC^{8–11}. The infected cell expresses and multiples only a limited number of input HSV-1 genomes (fewer than eight at a multiplicity of infection of 100)¹². Each small VRC, initially located at the nuclear periphery, originates from a single viral genome^{12–15}. These small VRCs undergo actin-mediated directed movement⁸, resulting in their fusion and eventual enlargement into the entire nucleus. The expansion of the VRCs is accompanied by an increase in the nuclear volume and relocation of the host chromatin into the nuclear periphery^{16,5}. It is in these VRCs that viral nucleocapsid assembly occurs. Soon after assembly, each nucleocapsid penetrates the host chromatin layer and nuclear lamina to the inner nuclear envelope, the site of its egress^{2,17,18}.

Despite their many achievements with biological applications, light- and electron-based imaging techniques suffer from fundamental limitations in 3D imaging of the subcellular architecture of the entire cell. Transmission electron microscopy (TEM) and TEM tomography are limited by fixation-induced distortions of cellular features, damage caused by the electron beam and the limited range of angular sampling. Fluorescence microscopy can determine the positions of specific molecules, but only of those selected based on existing information, including

¹University of Jyväskylä, Department of Physics and Nanoscience Center, Jyväskylä, FI-40500, Finland. ²University of Jyväskylä, Department of Biological and Environmental Science and Nanoscience Center, Jyväskylä, FI-40500, Finland. ³Department of Anatomy, University of California San Francisco, San Francisco, CA, 94158, USA. ⁴Physical Biosciences Division, Lawrence Berkeley National Laboratory, Berkeley, CA, 94720, USA. ⁵University of Turku, Turku, Finland. ⁶International Center for Research in Infectiology (CIRI), INSERM U1111, CNRS UMR5308, Lyon, F-69007, France. ⁷Ecole Normale Supérieure de Lyon, Lyon F-69007, France. ⁸Université de Lyon, UCB-Lyon1, Lyon, F-69007, France. ⁹LabEx Ecofect, Université de Lyon, Lyon, F-69007, France. ¹⁰ITMO University, Kronverkskii ave. 49, 197101, Saint Petersburg, Russia. *These authors contributed equally to this work. Correspondence and requests for materials should be addressed to M.V.-R. (email: maija.vihinen-ranta@jyu.fi)

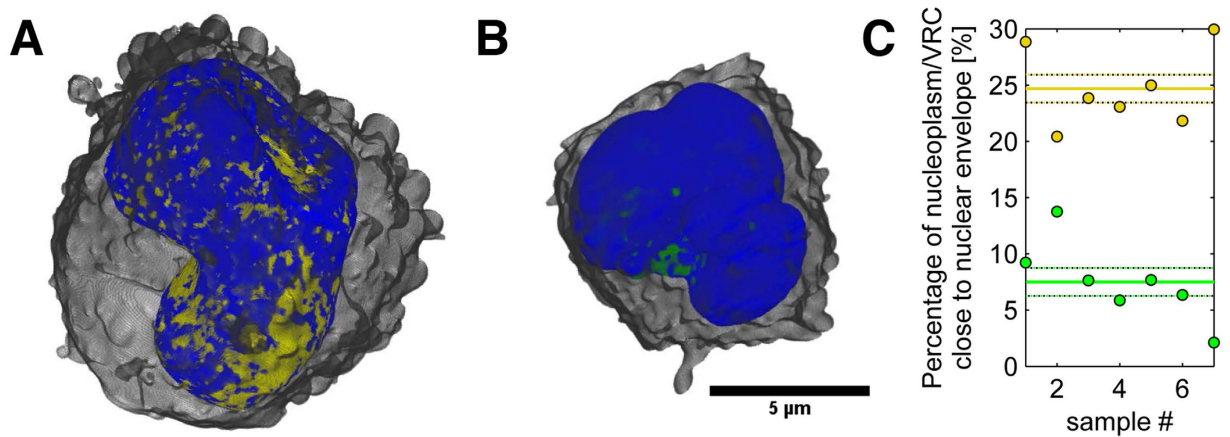


Figure 1. Structure of the marginalized host chromatin. Volume-rendered 3D views of nuclei, showing (A) the high-LAC value heterochromatin (blue) and low-LAC value nucleoplasm with VRC (yellow) of an infected cell, and (B) the heterochromatin (blue) and nucleoplasm without VRC (green) of a non-infected cell. See also Supplementary Video S1. (C) Percentage of nucleoplasm close to the nuclear envelope in infected (with VRC, yellow) and non-infected (green) cells. Solid lines represent the mean and dotted lines the mean \pm SEM ($n=7$).

the sizes of the labels and the density of the labelling. Furthermore, immunofluorescence imaging is prone to artefacts by fixation or permeabilization^{19,20}.

We employed a strategy integrating 3D soft X-ray tomography (SXT) imaging with cryogenic fluorescence microscopy (CFM), confocal and electron microscopy, and advanced data analysis in order to study in more detail the HSV-1-induced changes in nuclear architecture, molecular organization of the host chromatin and, in particular, the formation of channels across the chromatin layer. The short wavelength of soft X-rays enabled high-resolution 3D imaging of the nuclear architecture. Moreover, since X-rays can penetrate 15 μm -thick biological material, SXT allows for quantitative assessment of the entire cell. For SXT image acquisition, the cells were placed in (cylindrical) thin-walled capillaries of diameter up to 15 μm . B cells were used because of their small size and HSV-1 susceptibility^{21,22}.

In fact, SXT permits cell imaging in a near-native state i.e. intact, unsliced, unstained, and fully hydrated. X-ray absorption depends on the concentration of organic material in each voxel. Therefore, SXT not only detects multiple cellular structures but can also provide quantitative assessment of their composition and structure. Contrast in soft X-ray microscopy is generated by differential attenuation of X-rays by the biomolecules in the specimen and is not muted by weakly absorbing water. Attenuation of X-rays by the specimen follows the Beer-Lambert law²³ and is therefore both a linear and a quantitative measure of the thickness and the chemical species present at each point in the cell^{24–26}. To gain insight into the spatial localization of the host chromatin and of the viral and cellular proteins and nucleocapsids, we complemented 3D SXT with confocal and electron microscopy imaging techniques.

Results

Infectivity of B cells. To follow the progress of infection, we analysed the expression of viral immediate-early, early and late genes by cytometry and real-time RT-PCR (qPCR) and of the virus yields by plaque assay^{27–30}. We detected the presence of viral proteins, as well as the expression of viral lytic genes of all three phases of the replication cycle and substantial production of the progeny virus from the B cells. The highest yield of virus was obtained at 24 h p.i. (Supplementary Figs S1 and S2; see also Supplementary Text S1 for additional information). This suggests that not only could HSV-1 enter and infect B cells but also that its replication cycle was completed. Based on these findings, we decided to use a multiplicity of infection (MOI) of 5 and the time point 24 h p.i. in our subsequent experiments.

Virus-induced reorganization of the host chromatin. To further analyse the nuclear architecture, we used SXT on hydrated cells in their near-native state. The image contrast of SXT is based on the absorption of X-rays by mainly carbon and nitrogen. This allows measurement of the linear absorption coefficients (LAC) of cellular structures reflecting their concentration of cellular biomolecules^{31,32}. Owing to its high density of biomolecules, the heterochromatin region of the nucleus has a higher LAC than the less densely packed nucleoplasm, as is evident from computer-generated SXT ortho-slices through nuclei (Supplementary Fig. S3). The use of an HSV-1 strain expressing EYFP-ICP4 allowed the detection of infected cells with enlarged VRC by CFM used in SXT studies. When SXT ortho-slices were aligned with CFM images of the same cell^{33,34}, EYFP-ICP4 was found to be localized in distinct nuclear foci or in a few enlarged foci in the heterochromatin-depleted nuclear regions (Supplementary Fig. S3).

Virus-induced gaps in the cellular chromatin. The distinct LAC values of SXT were used to automatically segment the nuclear structures for 3D visualization of the spatial information in HSV-1 infected cells.

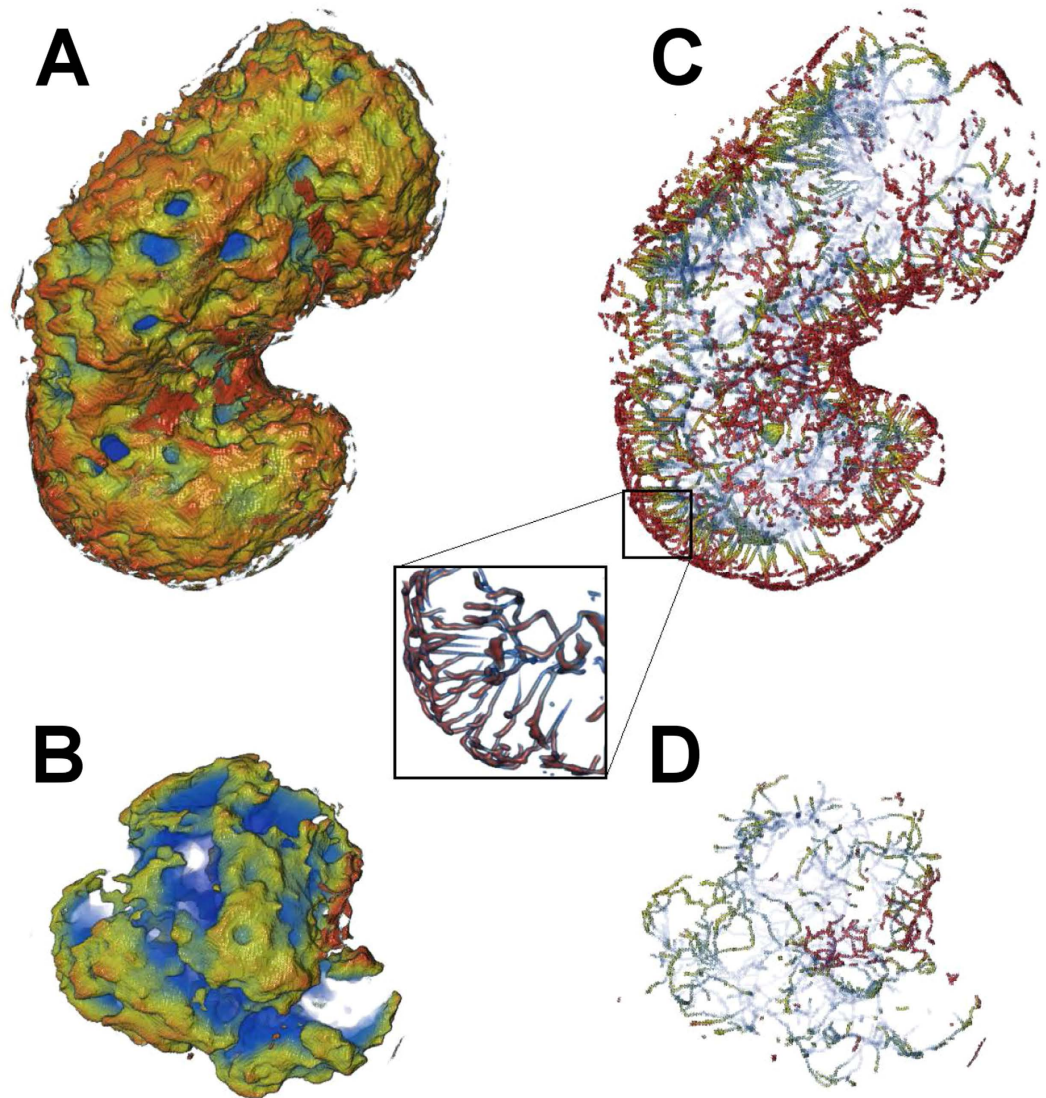


Figure 2. Distribution of low-LAC channels in close proximity to the nuclear envelope in infected and non-infected cells. Low-LAC regions of the nucleoplasm with (A) and without (B) VRC adjacent to the nuclear envelope. A computationally reduced skeletonized structure of the low-LAC regions in the $0.5\ \mu\text{m}$ -thick layer of host chromatin close to the nuclear envelope, which shows channels across the peripheral heterochromatin in infected (C) as well as non-infected (D) cells. Pseudo-colour indicates (increasing from red to blue) the distance from the nuclear envelope. See also Supplementary Video S2.

Surface-rendered 3D tomographic reconstructions (Fig. 1A; Supplementary Video S1) of the nuclear periphery of the infected cells revealed low-density gaps in the compact layer of marginalized host chromatin. Statistical analysis showed that $24.7 \pm 1.2\%$ ($n = 7$) of the surface area (10 closest voxels with a linear voxel size of $320\ \text{nm}$) of the chromatin had a low-LAC value ($0.222\text{--}0.322\ \mu\text{m}^{-1}$), suggesting the presence of low-density regions in the compact chromatin (Fig. 1C). In the non-infected cells the relative area of the region with a low LAC value was $7.5 \pm 1.2\%$ ($n = 7$) (Fig. 1B,C).

In order to further study the low-LAC regions, we analysed their ‘skeletonized’ versions. The skeletonized structure revealed that the low-LAC regions formed channels in the $0.5\ \mu\text{m}$ -thick layer of host chromatin close to the nuclear envelope, some of which penetrated the nuclear periphery across the layer of peripheral (compacted) chromatin in both infected and non-infected cells (Fig. 2A–D; see also Supplementary Video S2). However, in the infected cells the total number of low-LAC breaks, 900 ± 300 ($n = 7$), was significantly higher ($p < 0.01$) than in the non-infected cells (170 ± 40 , $n = 7$). Note that the average volume of the nucleus ($260 \pm 20\ \mu\text{m}^3$), was significantly ($p < 0.01$) increased in the infected cells compared to the non-infected cells ($170 \pm 14\ \mu\text{m}^3$). Additionally, analysis of the density of these channels across the layer of marginalized heterochromatin as a function of distance from the nuclear envelope (SXT images) revealed that, in a $0.1\ \mu\text{m}$ band close to the nuclear envelope, the area density of these channels was significantly ($p < 0.01$) higher in the infected ($2.4 \pm 0.4\ \mu\text{m}^{-2}$) than in the non-infected ($0.65 \pm 0.11\ \mu\text{m}^{-2}$) cells (Fig. 3A). Furthermore, analysis of their local thickness as a function

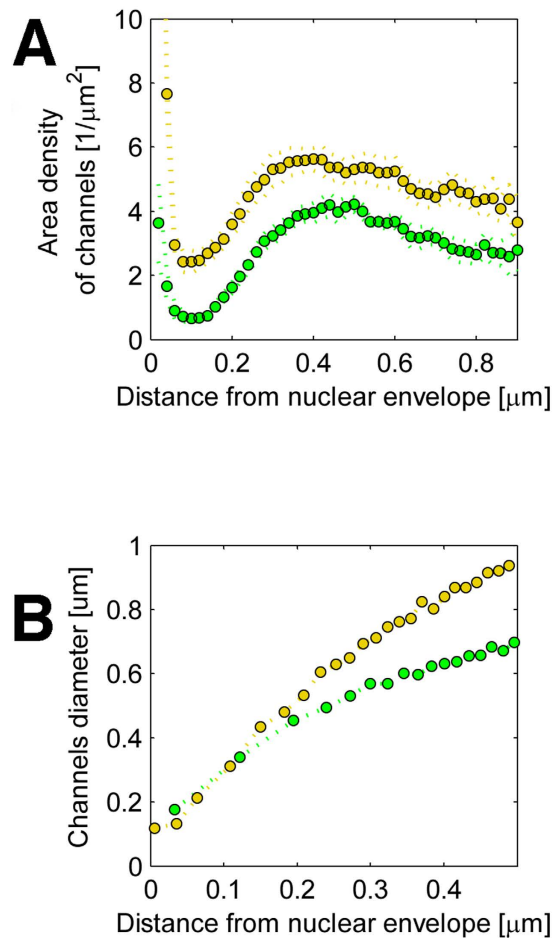


Figure 3. Density and diameter of low-LAC channels next to nuclear envelope. (A) Analysis of SXT images, showing the area density of channels across the heterochromatin as a function of distance from the nuclear envelope for infected (yellow) and non-infected (green) cells. (B) Local thickness of the channels as a function of distance from the nuclear envelope. Dotted lines represent the means of the distributions (n = 7).

of distance from the nuclear envelope indicated that their diameter increased towards the nuclear centre, and that they finally merged with the nucleoplasm of the infected (with a VRC) and non-infected cells. The smallest diameter of these channels at the nuclear periphery, at 0.1 μm from the nuclear envelope in both cases, was at least 200 nm (Fig. 3B). Their size was thus sufficient to allow the passage of at least one viral nucleocapsid (diameter 125 nm) at a time.

It is known that heterochromatin-free gaps are associated with NPCs and involved in nucleo-cytoplasmic transport of non-infected cells³⁵. This prompted us to study whether the virus-induced channels are connected with NPCs. The number and distribution of low-DAPI gaps across the heterochromatin were compared with those of NPCs. Immunolabelling of cells with the Nup153 antibody revealed that NPCs frequently formed clusters in both infected and non-infected cells. Some of these clusters were significantly enlarged in the infected cells (Fig. 4A; see also Supplementary Fig. S4). The numbers of NPCs or NPC clusters in the infected cells (105 ± 6 , n = 19) were reduced compared to those in non-infected (145 ± 9 , n = 20) cells (Fig. 4A,B; see also Supplementary Fig. S4). Accordingly, in the infected cells the total number of low-LAC breaks was higher than the number of NPCs, whereas in the non-infected cells the number of breaks in the nuclear periphery was close to that of NPCs. Moreover, our studies showed that, in the infected cells, the low-DAPI regions were almost always located independently of NPCs, whereas in the non-infected cells, the low-DAPI regions were located adjacent to the NPCs (Fig. 4A,B).

In summary, these results demonstrated that HSV-1 infection increases the number of virus-capsid-sized and NPC-independent gaps, which may facilitate the viral transport across the compacted layer of chromatin.

Nucleocapsids in low-density chromatin gaps. Confocal microscopy was performed to detect the presence of nucleocapsid proteins in the low-density chromatin regions of the nuclear periphery. Viral capsid protein VP5 was frequently seen in low-DAPI regions in close proximity to the nuclear envelope (Fig. 5; see also Supplementary Video S3).

Next, we used transmission electron microscopy to examine the distribution of nucleocapsids with respect to the peripheral marginalized chromatin. The images showed that nucleocapsids were very often localized in the

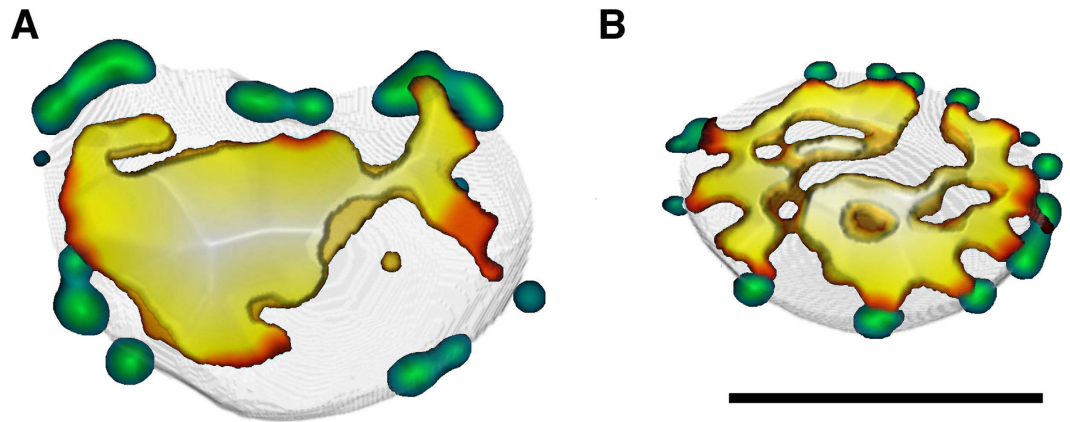


Figure 4. Spatial interaction between low-density gaps and nuclear pore complexes. Views of nuclear middle section, showing 3D reconstructions of confocal images of (A) infected and (B) non-infected cells. Images show the distribution of low-DAPI areas in comparison to Nup153-labeled NPCs (green). Low-DAPI areas denote DAPI intensity $< 23\%$ of maximum. In the colour map, the low-DAPI area ranges from blue to white. Blue indicates a minimal distance whereas white indicates a maximal distance from the nuclear envelope. Scale bars, $3\ \mu\text{m}$.

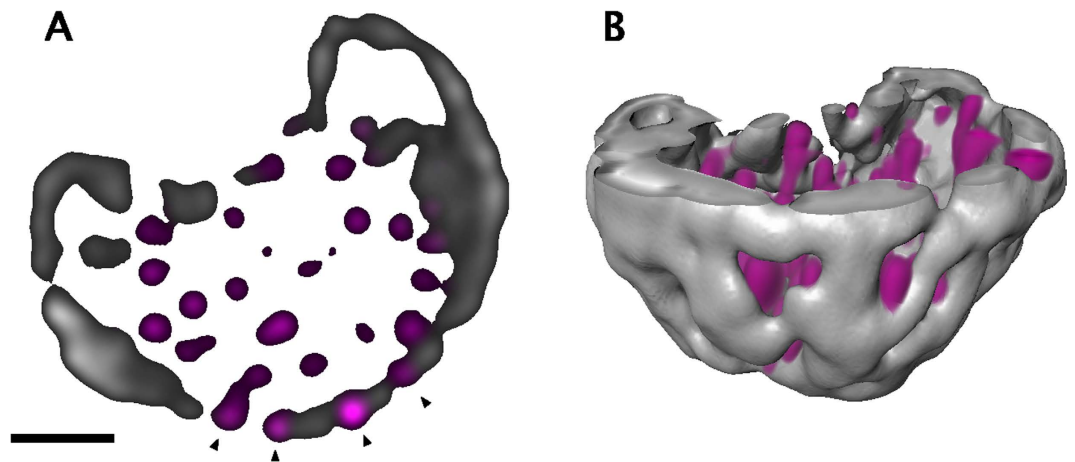


Figure 5. Distribution of nucleocapsid proteins in low-density chromatin regions of nuclear periphery. (A) Confocal microscopy images of an infected cell with marginalised chromatin stained with antibodies for the capsid protein VP5 (magenta) and DAPI (grey). White arrowheads indicate the presence of VP5 in the low-DAPI regions (black) in close proximity to the nuclear envelope. Scale bar is $3\ \mu\text{m}$. (B) 3D reconstruction of confocal image, which shows VP5 (magenta) and chromatin (grey). See also Supplementary Video S3.

chromatin region next to the nuclear envelope. Consistently with the confocal data, these nucleocapsids were located in the low-density chromatin breaks and narrow virus-nucleocapsid-sized channels (Fig. 6A). The NPCs are mostly invisible in the infected cells, presumably because of virus induced structural changes of the NE. The distribution of chromatin and NPCs in the non-infected cells is shown in the Supplementary Fig. S5. This is in line with recent studies showing that herpesvirus infection increases the porosity of the nucleus, leading to an enhancement of nucleocapsid motility³⁶. Altogether, our findings showed that HSV-1 infection induces breakages penetrating the cellular chromatin barrier to permit nucleocapsid access to the nuclear envelope.

Discussion

Formation of a VRC as a result of HSV-1 lytic infection is followed by structural changes in the host chromatin^{5,37–39}. Profound reorganization of the nuclear chromatin by HSV-1 has been known to include chromatin marginalization to the nuclear periphery^{16,5}. A compact layer of host heterochromatin constitutes an accessibility barrier for the translocation of viral nucleocapsids toward the inner nuclear envelope across which they exit the nucleus. A previous indication of HSV-1 infection's ability to disrupt marginalised chromatin, so as to allow access through it, has come from immunofluorescence studies showing fragmented distribution of histone H1, suggesting the presence of routes through chromatin⁵. By combining SXT, CFM and confocal imaging techniques with advanced image analysis, we achieved a new insight into the 3D structure and distribution of such breakages.

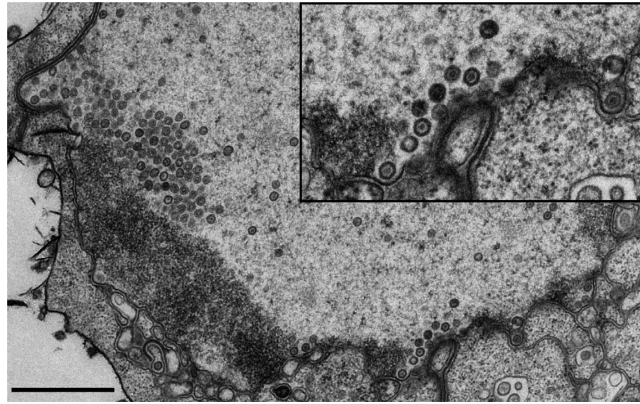


Figure 6. Nucleocapsids in low-density regions of chromatin. Transmission electron microscopy images of infected cell nuclei, which show B cells at 24 h p.i. The inset shows enlarged view of the boxed areas containing the viral nucleocapsids adjacent to the nuclear envelope. Scale bar, 1 μ m.

We observed that the low-density regions in the host chromatin formed gaps through it. In the absence of infection these openings were typically located near NPCs, in agreement with earlier results on the density distribution of the host chromatin³⁵. In the infected cells, the number of these low-density breakages was significantly increased, and they were most often located independent of NPCs. This independence was in agreement with the NPC-independent nuclear egress of the virus^{2,40}. The SXT analysis revealed channels wide enough to allow the passage of a 125-nm-wide HSV-1 nucleocapsid. However, the narrowest channels, with a diameter of 200 nm, allowed the passage of only one or a few nucleocapsids at a time. This leads to the presence of nucleocapsids in the discontinuous-density regions of the peripheral chromatin close to the nuclear envelope, which agrees well with the egress mechanism demonstrated previously^{2,5}. The exact nature of the molecular mechanisms involved in the intra-nuclear motility of the capsids is controversial. It has been suggested that nucleocapsids are transported in the nucleoplasm via an active process mediated by an intra-nuclear actin and myosin motor protein^{3,41–45}. However, a very recent study showed that their motility is based on passive diffusion^{36,46}.

In summary, we were able to create 3D reconstructions of intact and fully hydrated HSV-1 infected cell nuclei by using SXT. We also used other techniques to complement the structural information thus gained. Our study reveals the induction of channels allowing for the nuclear egress of the progeny viruses across the host chromatin. Moreover, this work used a new combination of methods in the study of virus-cell interactions.

Materials and Method

Cells and viruses. A continuously growing pre-B cell line was produced with the Abelson murine virus⁴⁷. The female mouse B cells were a gift from Barbara Panning (UCSF School of Medicine, Biochemistry and Biophysics, San Francisco, CA). The Epstein-Barr virus-transformed human B lymphocytes (GM12878) were purchased from the NGIMS Human Genetics Cell Repository, Coriell Institute of Medical Research (NJ). The mouse B and human B cells were maintained as suspension cultures at 37 °C in RPMI-1640 medium (GIBCO, Invitrogen, Inc.), supplemented with 10% or 15% of fetal bovine serum (FBS) (GIBCO, Invitrogen, Inc.), L-glutamine, penicillin, streptomycin and 5% CO₂. The medium was refreshed every two to three days to maintain a cell density of 0.8–2 $\times 10^6$ cells/ml. The HSV-1 strains were wt (17+) and 17+ expressing EYFP-ICP4 (vEYFP-ICP4), a generous gift from R. Everett (MRC Virology Unit, Glasgow, Scotland, UK)¹. The viruses had been isolated as described in¹. For infection, cells were inoculated with HSV-1 or HSV-1 EYFP-ICP4 (MOI 5–10) and kept at 37 °C until the SXT analysis, live-cell microscopy or fixation.

Immunolabelling studies. The cells were infected with HSV-1 or vEYFP-ICP4 HSV-1 at MOI 5. At 24 h p.i., cells were collected by centrifugation (400 RCF for 5 min), spread and air-dried on Zeiss high-performance cover slips (D = 0.17 mm, size 18 \times 18 mm²). Cells were fixed with 4% paraformaldehyde (PFA; 20 min at room temperature [RT]). Viral capsid proteins were detected with a capsid protein VP5-specific monoclonal antibody (MAB; Santa Cruz Biotechnology, Inc., TX) and NPCs with Nup153 MAb (Abcam, Cambridge, MA), followed by a goat anti-mouse Alexa 594 secondary antibody (Ab; Molecular Probes, Life Technologies, NY). DNA was stained during embedding with DAPI (4',6-diamidino-2-phenylindole; Molecular Probes), containing ProLong antifade compound. Imaging was done using a Nikon A1R laser-scanning confocal microscope (Nikon Instruments, Inc., Amsterdam, Netherlands.) with the CFI Plan Apo VC 60XH (NA 1.4, WD 0.13, oil immersion objective). DAPI was excited with a 405-nm diode laser and its fluorescence was detected with a 450/50-nm band-pass filter. EYFP was excited with a 514-nm argon laser and its fluorescence was collected with a 540/30-nm band-pass filter. Alexa 594 was excited with a 561-nm sapphire laser and the fluorescence was collected with a 595/50-nm band-pass filter. For 3D image stacks, 512 \times 512 pixels were collected from an appropriate depth depending on the sample. Pixel resolution was adjusted to 50 nm/pixel in x and y dimensions, and to 150 nm in the z dimension. AutoGain was used in multipoint imaging. Iterative deconvolution was performed with a signal-to-noise ratio set at 7, a quality threshold set at 0.01. Deconvolution was performed with Huygens Essential software (SVI, Hilversum, Netherlands). Image analysis was done with ImageJ⁴⁸. The number of NPCs was calculated from the maximum

intensity projection images. The amount and volume of NPC areas were calculated by a 3D object counter from manually thresholded data. In the fixed-cell images the volume analysis was done by first de-noising the images with a Gaussian blur, $\sigma = 2$, and then making a binary image with the Otsu threshold. Holes were filled and the amount and volume of objects were determined using the 3D-Objects-Counter plugin⁴⁹.

Specimen preparation for soft X-ray tomography. Cells were seeded at a concentration of 10^6 cells/ml into a standard plastic culture flask (Corning, Corning, NY), and infected with vEYFP-ICP4 at a MOI of 5 for 24 h at 37 °C. Infected cells were pelleted by centrifugation (400 RCF for 5 min), re-suspended in the growth medium, filtered, loaded into thin-walled glass capillaries and then vitrified by quickly plunging them into liquid-nitrogen-cooled (~ 90 °K) liquid propane, using a custom device³⁴.

Cryogenic confocal fluorescence microscopy. Vitrified cells expressing EYFP-ICP4 were identified and imaged in specimen capillaries, using a custom-made cryogenic confocal fluorescence microscope. The cryogenic light microscope, made in-house, features a custom-made specimen holder, a modified immersion objective lens and a ~ 10 l reservoir of liquid nitrogen. Other components were commercial, including a Yokogawa spinning-disk confocal head (CSU-X1, Yokogawa, Tokyo, Japan) and an integrated system of acousto-optical tuneable filtered (AOTF) lasers (Andor Laser Combiner, Model LC-501A; Andor Technologies, Belfast, UK). For more detailed description of the instrument, see³⁴. EYFP was excited using a 491-nm laser and imaged with an EMCCD (iXon Model Numbers DV887ECS-BV, Andor Technologies) using a standard 580/30-nm band-pass emission filter (Chroma Technology Corp., Bellows Falls, VT).

Soft X-ray tomography. SXT data were collected with a soft X-ray microscope XM-2 in the National Center for X-ray Tomography (<http://ncxt.lbl.gov>) at the Advanced Light Source (<http://www.als.lbl.gov>) of Lawrence Berkeley National Laboratory (Berkeley, CA) using a 50-nm objective zone plate. Cells were kept in a stream of liquid-nitrogen-cooled helium gas^{31,50} during data collection, which allowed the collection to be conducted without observable radiation damage. For each data set, 90–180 projection images were collected sequentially around a rotation axis in 1–2° increments, with a total rotation of 180°, using a 300–400 ms exposure time. Projection images were normalized²⁵ and manually aligned using the IMOD software, by tracking fiducial markers on adjacent images⁵¹; tomographic reconstructions were calculated using iterative reconstruction methods^{52,53}. LAC values were determined as described⁵⁴. The student's t-test (two-tailed, unequal variance) was used to evaluate statistical significance.

Transmission electron microscopy (TEM). Infected cells and non-infected control cells were fixed in 4% paraformaldehyde and 0.25% glutaraldehyde in 50 mM phosphate buffer (pH 6.8) and post-fixed in 1% OsO₄ for 1 h on ice. Cells were dehydrated through an ethanol series and then embedded in low-viscosity embedding resin (TAAB Laboratories Equipment Ltd, UK). Thin sections were cut using Ultracut UC6a ultramicrotome (Leica Mikrosysteme GmbH, Germany) and collected on Pioloform-coated, single-slot copper grids. After double staining with 2% aqueous uranyl acetate and lead citrate, the sections were examined using TEM JEOL JEM1400JEOL (JEOL Ltd., Tokyo, Japan), operated at 80 kV. The images were recorded using a bottom-mounted Quemesa CCD camera with 4008 × 2664 pixel resolution.

References

- Everett, R. D., Sourvinos, G. & Orr, A. Recruitment of herpes simplex virus type 1 transcriptional regulatory protein ICP4 into foci juxtaposed to ND10 in live, infected cells. *J. Virol.* **77**, 3680–3689 (2003).
- Johnson, D. C. & Baines, J. D. Herpesviruses remodel host membranes for virus egress. *Nat. Rev. Microbiol.* **9**, 382–394 (2011).
- Reynolds, A. E., Liang, L. & Baines, J. D. Conformational changes in the nuclear lamina induced by herpes simplex virus type 1 require genes U(L)31 and U(L)34. *J. Virol.* **78**, 5564–5575 (2004).
- Salvetti, A. & Greco, A. Viruses and the nucleolus: the fatal attraction. *Biochim. Biophys. Acta.* **1842**, 840–847 (2014).
- Simpson-Holley, M., Baines, J. D., Roller, R. & Knipe, D. M. Herpes simplex virus 1 U(L)31 and U(L)34 gene products promote the late maturation of viral replication compartments to the nuclear periphery. *J. Virol.* **78**, 5591–5600 (2004).
- Copeland, A. M., Newcomb, W. W. & Brown, J. C. Herpes simplex virus replication: roles of viral proteins and nucleoporins in capsid-nucleus attachment. *J. Virol.* **83**, 1660–1668 (2009).
- Pasdeloup, D., Blondel, D., Isidro, A. L. & Rixon, F. J. Herpesvirus capsid association with the nuclear pore complex and viral DNA release involve the nucleoporin CAN/Nup214 and the capsid protein pUL25. *J. Virol.* **83**, 6610–6623 (2009).
- Chang, L. *et al.* Herpesviral replication compartments move and coalesce at nuclear speckles to enhance export of viral late mRNA. *Proc. Natl. Acad. Sci. USA* **108**, E136–44 (2011).
- Kobiler, O., Drayman, N., Butin-Israeli, V. & Oppenheim, A. Virus strategies for passing the nuclear envelope barrier. *Nucleus* **3**, 526–539 (2012).
- Lukonis, C. J. & Weller, S. K. Formation of herpes simplex virus type 1 replication compartments by transfection: requirements and localization to nuclear domain 10. *J. Virol.* **71**, 2390–2399 (1997).
- Simpson-Holley, M., Colgrove, R. C., Nalepa, G., Harper, J. W. & Knipe, D. M. Identification and functional evaluation of cellular and viral factors involved in the alteration of nuclear architecture during herpes simplex virus 1 infection. *J. Virol.* **79**, 12840–12851 (2005).
- Kobiler, O., Lipman, Y., Therkelsen, K., Daubechies, I. & Enquist, L. W. Herpesviruses carrying a Brainbow cassette reveal replication and expression of limited numbers of incoming genomes. *Nat. Commun.* **1**, 146 (2010).
- Kobiler, O., Brodersen, P., Taylor, M. P., Ludmir, E. B. & Enquist, L. W. Herpesvirus replication compartments originate with single incoming viral genomes. *MBio* **2**, e00278–11 (2011).
- Silva, L., Cliffe, A., Chang, L. & Knipe, D. M. 2008. Role for A-type lamins in herpesviral DNA targeting and heterochromatin modulation. *PLoS Pathog.* **4**, e1000071 (2008).
- Silva, L. *et al.* Roles of the nuclear lamina in stable nuclear association and assembly of a herpesviral transactivator complex on viral immediate-early genes. *MBio* **3**, e00300–11.
- Monier, K., Armas, J. C., Etteldorf, S., Ghazal, P. & Sullivan, K. F. 2000. Annexation of the interchromosomal space during viral infection. *Nat. Cell Biol.* **2**, 661–665 (2008).

17. Klupp, B. G. *et al.* Vesicle formation from the nuclear membrane is induced by coexpression of two conserved herpesvirus proteins. *Proc. Natl. Acad. Sci. USA* **104**, 7241–7246 (2007).
18. Park, R. & Baines, J. D. Herpes simplex virus type 1 infection induces activation and recruitment of protein kinase C to the nuclear membrane and increased phosphorylation of lamin B. *J. Virol.* **80**, 494–504 (2006).
19. Fischer, A. H., Jacobson, K. A., Rose, J. & Zeller, R. Fixation and permeabilization of cells and tissues. *CSH Protoc.* pdb top36 (2008).
20. Wilson, S. M. & Bacic, A. Preparation of plant cells for transmission electron microscopy to optimize immunogold labeling of carbohydrate and protein epitopes. *Nat. Protoc.* **7**, 1716–1727 (2012).
21. Spear, P. G. & Longnecker, R. Herpesvirus entry: an update. *J. Virol.* **77**, 10179–10185 (2003).
22. Eling, D. J., Johnson, P. A., Sharma, S., Tufaro, F. & Kipp, T. J. Chronic lymphocytic leukemia B cells are highly sensitive to infection by herpes simplex virus-1 via herpesvirus-entry-mediator A. *Gene Ther.* **7**, 1210–1216 (2000).
23. Hanssen, E. *et al.* Soft X-ray microscopy analysis of cell volume and hemoglobin content in erythrocytes infected with asexual and sexual stages of *Plasmodium falciparum*. *J. Struct. Biol.* **177**, 224–232 (2012).
24. Larabell, C. A. & Nugent, K. A. Imaging cellular architecture with X-rays. *Curr. Opin. Struct. Biol.* **20**, 623–631 (2012).
25. Parkinson, D. Y., Knoechel, C., Yang, C., Larabell, C. A. & Le Gros, M. A. Automatic alignment and reconstruction of images for soft X-ray tomography. *J. Struct. Biol.* **177**, 259–266 (2012).
26. Parkinson, D. Y. *et al.* Nanoimaging cells using soft X-ray tomography. *Methods Mol. Biol.* **950**, 457–481 (2013).
27. Nygårdas, M. *et al.* A herpes simplex virus-derived replicative vector expressing LIF limits experimental demyelinating disease and modulates autoimmunity. *PLoS One* **8**, e64200 (2013).
28. Paavilainen, H. *et al.* Innate responses to small interfering RNA pools inhibiting herpes simplex virus infection in astrocytoid and epithelial cells. *Innate Immun.* **21**, 349–357 (2015).
29. Romanovskaya, A. *et al.* Enzymatically produced pools of canonical and Dicer-substrate siRNA molecules display comparable gene silencing and antiviral activities against herpes simplex virus. *PLoS One* **7**, e51019 (2012).
30. Ziegler, T. *et al.* Typing of herpes simplex virus isolates with monoclonal antibodies and by nucleic acid spot hybridization. *J. Virol. Methods* **12**, 169–177 (1985).
31. McDermott, G., Le Gros, M. A., Knoechel, C. G., Uchida, M. & Larabell, C. A. Soft X-ray tomography and cryogenic light microscopy: the cool combination in cellular imaging. *Trends Cell Biol.* **19**, 587–595 (2009).
32. McDermott, G. *et al.* Visualizing and quantifying cell phenotype using soft X-ray tomography. *Bioessays* **34**, 320–327 (2012).
33. Smith, E. A. *et al.* Correlative cryogenic tomography of cells using light and soft x-rays. *Ultramicroscopy* **143**, 33–40 (2014).
34. Smith, E. A. *et al.* The Topological Organization of the Inactive X Chromosome in its Native State. *Biophys. J.* **106**, 434a–435a (2014).
35. Raices, M. & D'Angelo, M. A. Nuclear pore complex composition: a new regulator of tissue-specific and developmental functions. *Nat. Rev. Mol. Cell Biol.* **13**, 687–699 (2012).
36. Bosse, J. B. *et al.* Remodeling nuclear architecture allows efficient transport of herpesvirus capsids by diffusion. *Proc Natl Acad Sci. USA* **112**, E5725–E5733 (2015).
37. Knipe, D. M. & Cliffe, A. Chromatin control of herpes simplex virus lytic and latent infection. *Nat. Rev. Microbiol.* **6**, 211–221 (2008).
38. Knipe, D. M. *et al.* M. Snapshots: chromatin control of viral infection. *Virology* **435**, 141–156 (2013).
39. Weller, S. K. Herpes simplex virus reorganizes the cellular DNA repair and protein quality control machinery. *PLoS Pathog.* **6**, e1001105 (2010).
40. Nagel, C. H. *et al.* Nuclear egress and envelopment of herpes simplex virus capsids analyzed with dual-color fluorescence HSV1(17+). *J. Virol.* **82**, 3109–3124 (2008).
41. Tseng, Y., Lee, J. S., Kole, T. P., Jiang, I. & Wirtz, D. Micro-organization and visco-elasticity of the interphase nucleus revealed by particle nanotracking. *J. Cell Sci.* **117**, 2159–2167 (2004).
42. Cano-Monreal, G. L., Wylie, K. M., Cao, F., Tavis, J. E. & Morrison, L. A. Herpes simplex virus 2 UL13 protein kinase disrupts nuclear lamins. *Virology* **392**, 137–147 (2009).
43. Forest, T., Barnard, S. & Baines, J. D. Active intranuclear movement of herpesvirus capsids. *Nat. Cell Biol.* **7**, 429–431 (2005).
44. Leach, N. R. & Roller, R. J. Significance of host cell kinases in herpes simplex virus type 1 egress and lamin-associated protein disassembly from the nuclear lamina. *Virology* **406**, 127–137 (2010).
45. Roberts, K. L. & Baines, J. D. Actin in herpesvirus infection. *Viruses* **3**, 336–346 (2011).
46. Bosse, J. B. *et al.* Nuclear herpesvirus capsid motility is not dependent on F-actin. *MBio* **7**, e01909–14 (2014).
47. D'Andrea, E., Saggioro, D., Fleissner, E. & Chieco-Bianchi, L. Abelson murine leukemia virus-induced thymic lymphomas: transformation of a primitive lymphoid precursor. *J. Natl. Cancer Inst.* **79**, 189–195 (1987).
48. Abramoff, M. D., Magalhães, P. J. & Ram, S. J. Image processing with ImageJ. *Biophot. internat.* **11**, 36–43 (2004).
49. Bolte, S. & Cordelières, F. P. A guided tour into subcellular colocalization analysis in light microscopy. *J. Microsc.* **224**, 213–232 (2006).
50. Le Gros, M. A., McDermott, G. & Larabell, C. A. X-ray tomography of whole cells. *Curr. Opin. Struct. Biol.* **15**, 593–600 (2006).
51. Kremer, J. R., Mastronarde, D. N. & McIntosh, J. R. Computer visualization of three-dimensional image data using IMOD. *J. Struct. Biol.* **116**, 71–76 (1996).
52. Mastronarde, D. N. Fiducial marker and hybrid alignment methods for single-and double-axis tomography. In *Electron Tomography*, 163–185 (Springer, 2006).
53. Stayman, J. W. & Fessler, J. A. Compensation for nonuniform resolution using penalized-likelihood reconstruction in space-variant imaging systems. *IEEE Trans. Med. Imaging* **23**, 269–284 (2004).
54. Weiss, D. *et al.* Tomographic imaging of biological specimens with the cryo transmission X-ray microscope. Nuclear Instruments and Methods In *Physics Research Section A: Accelerators, Spectrometers, Detectors and Associated Equipment* **467**, 1308–1311 (2001).

Acknowledgements

We thank the staff of Advanced Light Source (Lawrence Berkeley National Laboratory, Berkeley, CA) staff for providing a safe, reliable source of photons used for imaging the cells in the present study. The SXT research was conducted at the National Center for X-ray Tomography (NCXT), and first-class experimental support by Rosanne Boudreau is gratefully acknowledged. We thank Liisa Lund, Arja Strandell, Mervi Lindman and Mervi Laanti for technical assistance and Electron Microscopy Unit of the Institute of Biotechnology, University of Helsinki, for EM sample preparation. We are grateful to Klaus Hedman for comments on the manuscript. This work was supported by INSERM, CNRS, Université Claude Bernard Lyon-1 and Ecole Normale Supérieure de Lyon (AS). It was financed by the Jane and Aatos Erkkö Foundation (JT, MVR), the National Institute of General Medical Sciences of the National Institute of Health, under the award number P41 GM103445, and the US Department of Energy, Biological and Environmental Research (DE-AC02-05CH11231, CAL) and the Academy of Finland, under the award numbers 138388 (MVR) and 259725 (VH).

Author Contributions

Conceived and designed the experiments: V.R., V.H., C.A.L. and M.V.-R. Performed the experiments: V.R., E.A.S., V.A., S.H. and P.P. Analysed the data M.M., V.R., E.A.S., V.A. and P.P. Contributed reagents/materials/analysis tools J.T., A.S., V.H., C.A.L. and M.V.-R. Wrote the paper: V.R., E.A.S., V.A., J.T., V.H., C.A.L. and M.V.-R. All authors reviewed the manuscript.

Additional Information

Supplementary information accompanies this paper at <http://www.nature.com/srep>

Competing financial interests: The authors declare no competing financial interests.

How to cite this article: Myllys, M. *et al.* Herpes simplex virus 1 induces egress channels through marginalized host chromatin. *Sci. Rep.* **6**, 28844; doi: 10.1038/srep28844 (2016).



This work is licensed under a Creative Commons Attribution 4.0 International License. The images or other third party material in this article are included in the article's Creative Commons license, unless indicated otherwise in the credit line; if the material is not included under the Creative Commons license, users will need to obtain permission from the license holder to reproduce the material. To view a copy of this license, visit <http://creativecommons.org/licenses/by/4.0/>

III


CHROMATIN ORGANIZATION REGULATES VIRAL EGRESS DYNAMICS

by

Aho, V., Myllys, M., Ruokolainen, V., Hakanen, S., Mäntylä, E., Virtanen, J., Hukkanen, V., Kühn, T., Timonen, J., Mattila, K., Larabell, C. A. & Vihinen-Ranta, M.

Scientific Reports, 7:3692, 2017

SCIENTIFIC REPORTS



OPEN

Chromatin organization regulates viral egress dynamics

Vesa Aho¹, Markko Myllys¹, Visa Ruokolainen², Satu Hakanen², Elina Mäntylä², Jori Virtanen³, Veijo Hukkanen⁴, Thomas Kühn^{5,6}, Jussi Timonen ^{1,7}, Keijo Mattila ^{1,8}, Carolyn A. Larabell^{9,10} & Maija Vihinen-Ranta²

Received: 22 January 2017

Accepted: 2 May 2017

Published online: 16 June 2017

Various types of DNA viruses are known to elicit the formation of a large nuclear viral replication compartment and marginalization of the cell chromatin. We used three-dimensional soft x-ray tomography, confocal and electron microscopy, combined with numerical modelling of capsid diffusion to analyse the molecular organization of chromatin in herpes simplex virus 1 infection and its effect on the transport of progeny viral capsids to the nuclear envelope. Our data showed that the formation of the viral replication compartment at late infection resulted in the enrichment of heterochromatin in the nuclear periphery accompanied by the compaction of chromatin. Random walk modelling of herpes simplex virus 1-sized particles in a three-dimensional soft x-ray tomography reconstruction of an infected cell nucleus demonstrated that the peripheral, compacted chromatin restricts viral capsid diffusion, but due to interchromatin channels capsids are able to reach the nuclear envelope, the site of their nuclear egress.

DNA viruses target the nucleus due to their dependence on the cellular DNA reproduction machinery, and the viral infection induces profound modifications of nuclear structures including chromatin. In lytic herpes simplex virus 1 (HSV-1) infection, the injection of the viral DNA into the nucleoplasm is followed by the formation of several small viral replication compartments (VRCs)^{1,2}. Later in infection, viral DNA replication and the accumulation of viral proteins is accompanied by the fusion of small VRCs into an enlarged VRC and increase in the nuclear volume^{3,4}. At the same time, with the emergence of the extensive VRC, the host chromatin is relocated into the nuclear periphery⁵⁻⁷. Chromatin marginalization that correlates with the expansion of the VRC is also seen in parvovirus⁸ and baculovirus⁹ infected cells. The progress of HSV-1 infection and the marginalization of host chromatin are accompanied by changes in the host gene expression¹⁰. Earlier studies have revealed that, instead of an HSV-1-induced general shut-down of cellular genes, the expression of some genes is maintained, or even increased in infection¹⁰⁻¹⁶. The final nuclear steps of infection are the assembly of viral capsids and their egress by budding through the inner nuclear membrane into the perinuclear space, followed by subsequent fusion with the outer nuclear membrane¹⁷⁻²⁰. To reach the inner nuclear membrane, viral capsids have to penetrate through the layer of marginalized host chromatin.

Despite many achievements in the research of virus-nucleus interactions, prior studies have not provided sufficient details on the spatial and molecular organization of chromatin to elucidate whether chromatin constitutes an accessibility barrier for the translocation of viral capsids towards the inner nuclear membrane. Thus, we investigated the detailed structural organization of chromatin at late infection. First, to gain insight into the spatial localization of chromatin and viral capsids, we used confocal and transmission electron microscopy (TEM) imaging. Next, we analysed the molecular organization of chromatin using soft x-ray tomography (SXT), which allows for assessment of the composition and structure of chromatin by providing a quantitative, linear measure of its density^{21,22}. Finally, we created high-resolution 3D SXT reconstructions of the chromatin of infected cell nuclei and used them for numerical modelling of the viral capsid-sized particle mobility in the chromatin using

¹Department of Physics, and Nanoscience Center, University of Jyväskylä, Jyväskylä, Finland. ²Department of Biological and Environmental Science, and Nanoscience Center, University of Jyväskylä, Jyväskylä, Finland. ³Institute of Biotechnology, University of Helsinki, Helsinki, Finland. ⁴Faculty of Medicine, University of Turku, Turku, Finland. ⁵Department of Applied Physics, University of Eastern Finland, Kuopio, Finland. ⁶Finnish Meteorological Institute, Kuopio, Finland. ⁷ITMO University, Saint Petersburg, Russia. ⁸Department of Physics, Tampere University of Technology, Tampere, Finland. ⁹Department of Anatomy, University of California San Francisco, San Francisco, California, USA. ¹⁰Physical Biosciences Division, Lawrence Berkeley National Laboratory, Berkeley, California, USA. Markko Myllys and Visa Ruokolainen contributed equally to this work. Correspondence and requests for materials should be addressed to M.V.R. (email: maija.vihinen-ranta@jyu.fi)

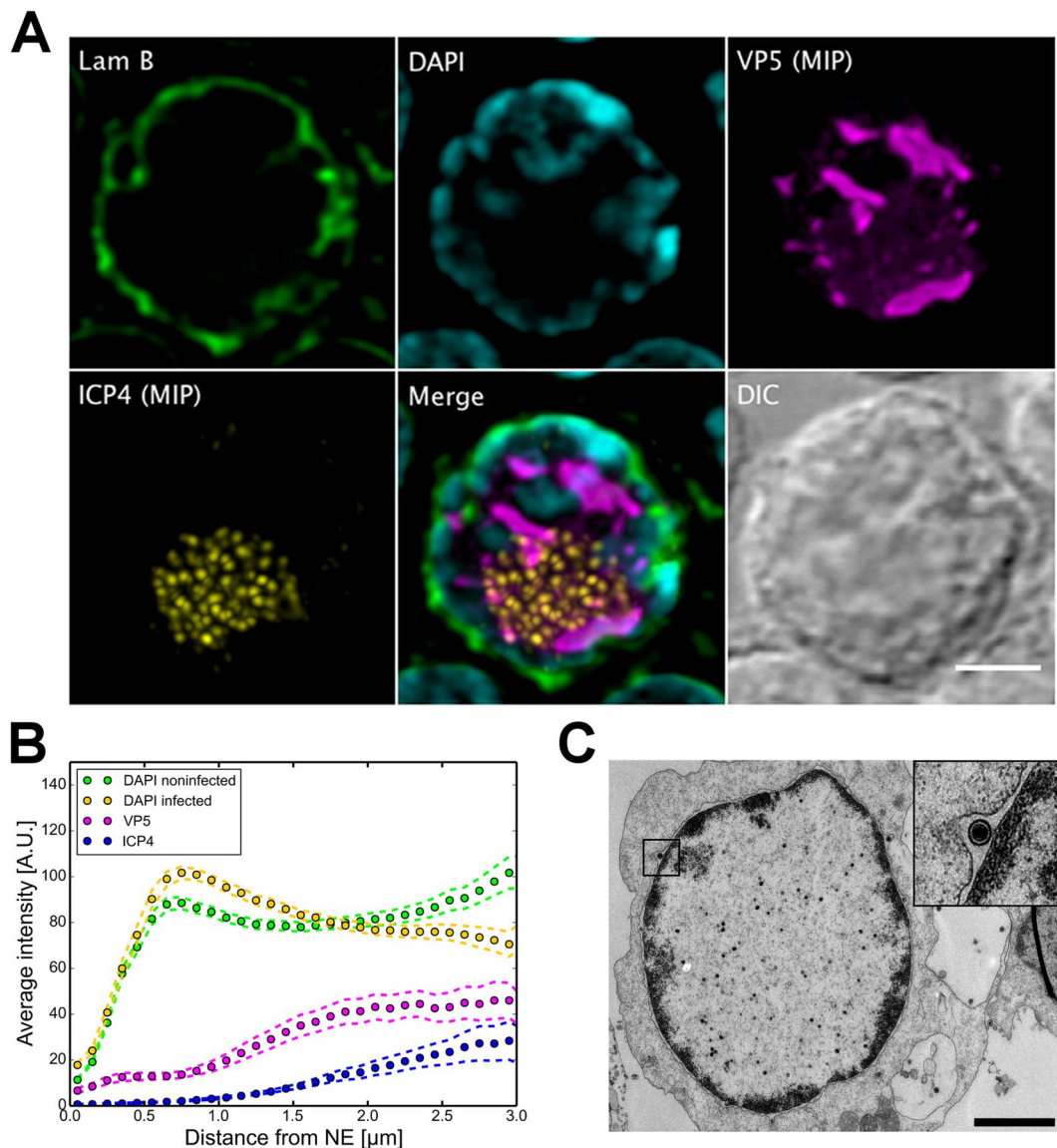


Figure 1. Nuclear distribution of host chromatin in infected cells with enlarged VRCs. **(A)** Confocal microscopy images showing the distribution of DAPI-labelled chromatin (cyan) and lamin B (green) together with maximum intensity projections (MIP) of viral EYFP-ICP4 (yellow) and VP5 (magenta) proteins at 24 h p.i. A differential interference contrast (DIC) image is also shown. Scale bar, 3 μm . **(B)** The mean spatial distribution of chromatin in infected ($n = 16$) and non-infected ($n = 20$) cells together with VP5 and ICP4 shown as plots of the intensity at increasing distances from the NE. Dotted error lines represent the mean \pm the standard error of the mean (SEM). **(C)** A TEM image of an infected cell nucleus at 24 h p.i. The inset shows an enlarged view of the boxed area containing the viral capsid in the space between the inner and outer leaflets of the nuclear membrane. Scale bar, 3 μm .

a random walk model. These studies revealed that the spatial organization and density of chromatin change in the late stage of infection and that these structural changes restrict the mobility of capsids. This demonstrates that low-density channels through the chromatin are needed to allow for the passage of progeny capsids to the nuclear envelope (NE).

Results

Marginalization of chromatin at late infection. The analysis of immunolabelled cells showed that at 24 h post infection (p.i.), 4',6-diamidino-2-phenylindole (DAPI)-labelled chromatin was concentrated at the nuclear periphery. At the same time, the viral immediate early protein EYFP-ICP4 accumulated into distinct small foci inside the VRC, whereas the capsid protein VP5 was located throughout the VRC. In contrast to control cells (Supplementary Figure S1), lamin B staining appeared discontinuous along the nuclear rim (Fig. 1A). The total volumes occupied by the viral proteins in the inner regions of the nucleus were $15 \pm 10 \mu\text{m}^3$ and $42 \pm 20 \mu\text{m}^3$ ($n = 20$) for ICP4 and VP5, respectively, while 0.24% of ICP4 and 8.8% of VP5 were located in the nuclear

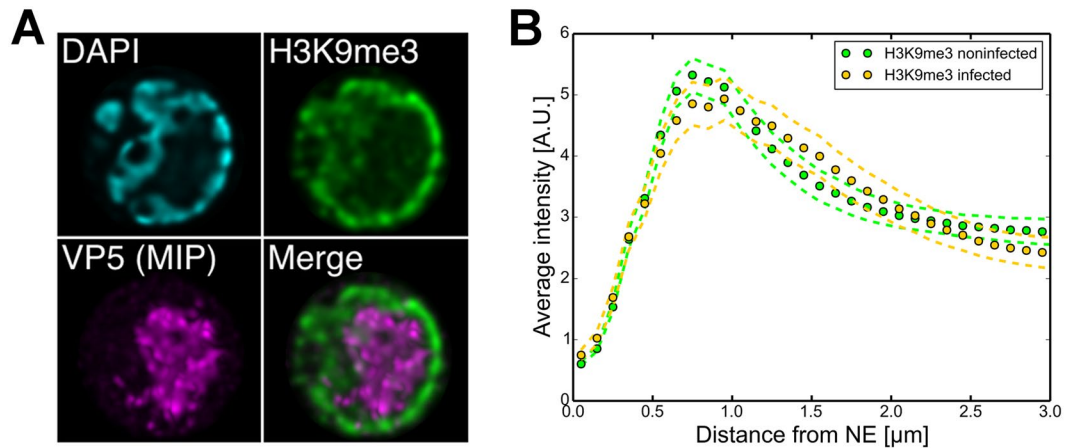


Figure 2. Redistribution of heterochromatin marker. **(A)** Confocal microscopy images of an infected cell with an enlarged VRC, stained with antibodies for VP5 (magenta), heterochromatin marker H3K9me3 (green) and DAPI (cyan) at 24 h p.i. See also Supplementary Figure S3. **(B)** Plot of the intensity of H3K9me3 in infected (yellow) and non-infected (green) cells as a function of the distance from the NE. Dotted error lines represent the mean \pm SEM.

periphery (the region between the DAPI label and NE). In some cells, EYFP-ICP4 and VP5 were also found to concentrate to the nuclear periphery (Supplementary Figure S2). Quantitative analysis of confocal microscopy data as a function of increasing distance from the NE confirmed the accumulation of chromatin to the region nearest to the NE in the infected cells. The amount of chromatin decreased towards the nuclear centre in infected cells, whereas in the non-infected cells chromatin was distributed more evenly throughout the nucleus (Fig. 1B). Here, although the VRC is in general devoid of the DNA-binding fluorochrome DAPI²³, we cannot rule out the possibility that a small portion of the host chromatin might be located in the same area with the VRC. In all the infected nuclei examined ($n = 16$), the majority of ICP4 and VP5 were located in the nuclear centre, with only a small fraction of the proteins located in a 1 μm -thick chromatin region next to the lamin B layer and to the NE.

Consistent with the confocal data, TEM analysis demonstrated that at 24 h p.i. the host chromatin was marginalized in close proximity to the NE. Viral capsids were typically located in the centre of the nucleus in the enlarged VRC area, and a portion of capsids was found in the gaps between the two nuclear membranes (Fig. 1C). In addition, our earlier studies indicated the presence of capsids in the virus-induced low-density chromatin breakages penetrating the peripheral chromatin⁷. In summary, confocal analysis combined with TEM confirmed that the emergence of an enlarged VRC was accompanied by the accumulation of chromatin at the nuclear periphery.

Distribution of modified histones. Histone proteins assemble DNA into nucleosomes, whose composition and spacing contribute to chromatin packing of higher order. We used histone H3 trimethyl Lys9 (H3K9me3) as a marker of transcriptional silencing to identify the tightly packed heterochromatin^{24,25}. Immunolabelling showed that this marker was located near the nuclear periphery in both the infected cells at late infection and in the non-infected cells (Fig. 2A, Supplementary Figure S3). We quantified the distribution of the chromatin marker by plotting fluorescence intensity as a function of distance from the NE detected with DAPI (Fig. 2B). The analysis showed that in both the infected and non-infected cells the H3K9me3 signal was strongest at the nuclear periphery and the infection did not cause major changes in the distribution of heterochromatin in comparison with that of non-infected cells. This suggested that the observed shift in the DAPI from the central regions of infected nuclei towards the nuclear periphery (Fig. 1B) was mainly caused by the exclusion of euchromatin to the periphery due to the emergence of an enlarged VRC.

Virus-induced compaction and reorganization of the host chromatin. To further study the architecture of the nucleus, we used SXT to image hydrated cells in the near-native state. SXT image contrast is based on the absorption of x-rays by mainly carbon and nitrogen. This allows the measurement of the linear absorption coefficient (LAC) of cell structures, which reflects the concentration of cellular biomolecules^{26,27}. Because of the increased density of biomolecules in heterochromatin, the heterochromatin region of the nucleus has a higher LAC than the less densely packed euchromatin, as is evident from computer-generated SXT orthoslices through nuclei (Supplementary Movie S1). The EYFP-ICP4 HSV-1 strain allowed detection of the VRC and identification of the infected cells by cryogenic fluorescence microscopy (CFM)⁷. When SXT orthoslices were aligned with CFM images of the same cell²⁸, EYFP-ICP4 was found to be localized in distinct nuclear foci or in a few enlarged foci in the heterochromatin-depleted regions of the nuclei⁷.

The distinct LAC values of SXT were used to automatically segment nuclear structures in the HSV-1 infected cells. In both the infected and non-infected cells, two populations of differing densities were evident (Fig. 3A and B, Supplementary Movie S1). In the following sections, the high-density population is referred to as heterochromatin and the low-density population either as euchromatin in the non-infected cells or VRC in the infected cells. Because of the similar LAC values of euchromatin and VRC, they cannot be distinguished in the infected cells, but due to the infection-induced marginalization of chromatin, which was also seen in our fluorescence

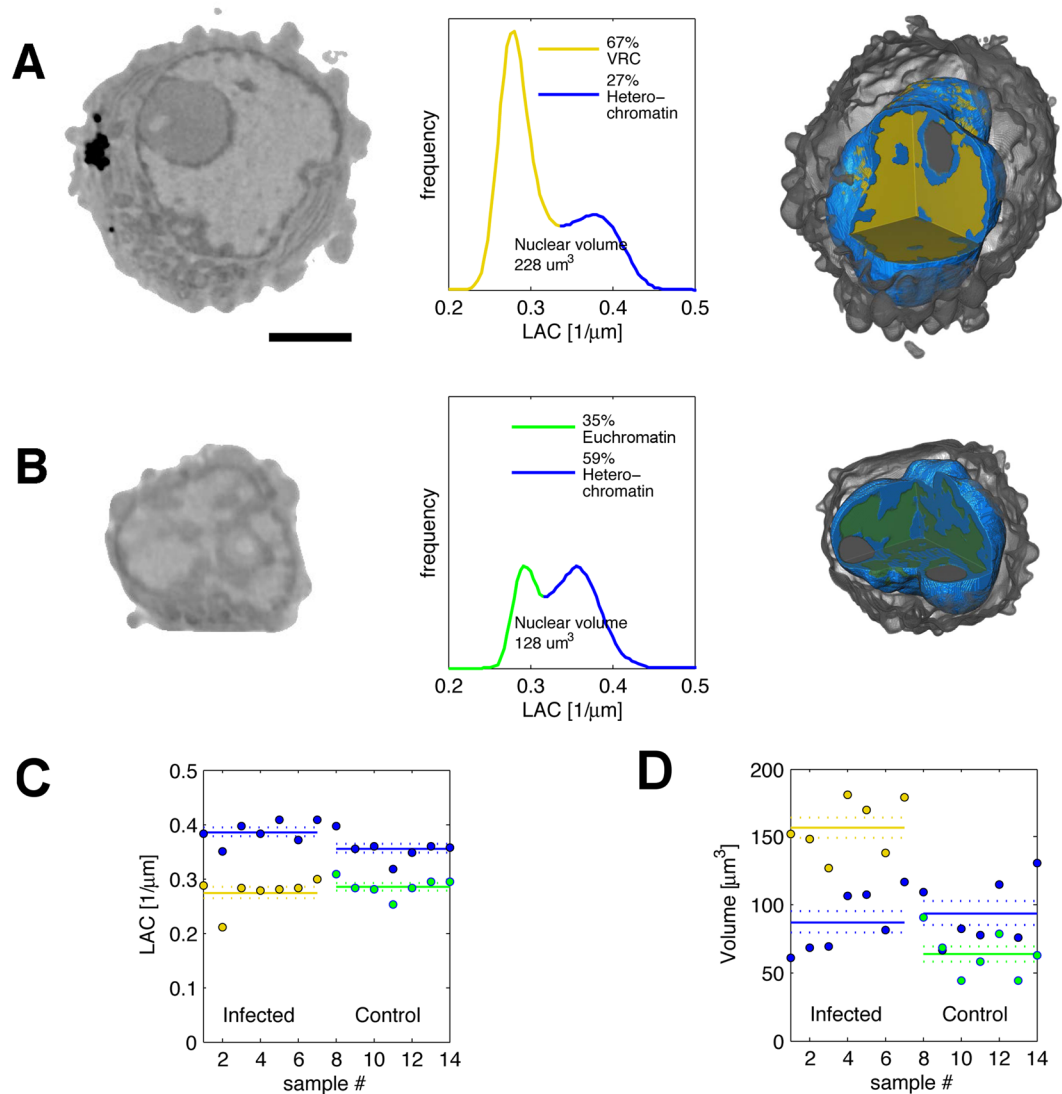


Figure 3. Virus-induced compaction and re-organization of the host chromatin. Nuclear volume of infected cells (A) was increased compared with non-infected cells (B) to accommodate VRC, as seen in SXT orthoslices (left) LAC-histograms plotting number of voxels with specific LAC values (centre), and 3D views of segmented and color-coded nuclei (right). Scale bar, 3 μm . (C) Nuclear LAC values and (D) volumes of heterochromatin (blue) and VRC (yellow) of infected cells ($n=7$) and volumes of heterochromatin (blue) and euchromatin (green) of non-infected cells. Solid lines represent the mean and dotted lines the mean \pm SEM. See also Supplementary Movie S1.

microscopy data, euchromatin is most likely relocated towards the same perinuclear areas where heterochromatin is located (Fig. 1B).

The infection-induced marginalization of the host chromatin had a clear effect on the heterochromatin density, increasing the LAC values of heterochromatin in comparison with those of the non-infected cells (Fig. 3A and B). In the infected cells, the average LAC of heterochromatin was $0.386 \pm 0.007 \mu\text{m}^{-1}$ ($n=7$), whereas in the non-infected cells it was $0.356 \pm 0.008 \mu\text{m}^{-1}$ ($n=7$) (Fig. 3C). In the infected cells, the highest LAC value was $0.459 \pm 0.012 \mu\text{m}^{-1}$, while it was $0.416 \pm 0.009 \mu\text{m}^{-1}$ in the non-infected cells. This indicated that heterochromatin was more tightly packed in the infected cells. The average LAC value of the VRC, $0.27 \pm 0.01 \mu\text{m}^{-1}$, was relatively similar to (or slightly lower than) that of the euchromatin (*i.e.*, in the non-infected cells), $0.285 \pm 0.006 \mu\text{m}^{-1}$ (Fig. 3C). The accuracy of the LAC measurements had been determined earlier by comparing increasing concentrations of BSA and haemoglobin *in vitro* with theoretical LAC values²⁹ and with those of alcohol-oxidase crystals in yeast cells²².

Plotting the number of voxels (volume) for specific LAC values showed that the average volume of both the nucleus ($260 \pm 20 \mu\text{m}^3$) and cytoplasm ($410 \pm 30 \mu\text{m}^3$) were increased in the infected cells (in the non-infected cells they were $170 \pm 14 \mu\text{m}^3$ and $178 \pm 14 \mu\text{m}^3$, respectively). The surface area of the nucleus also was increased, from $176 \pm 9 \mu\text{m}^2$ in the non-infected cells to $260 \pm 20 \mu\text{m}^2$ in the infected cells. Most of the increase in nuclear volume was due to the space occupied by the VRC ($157 \pm 7 \mu\text{m}^3$) – more than twice the volume occupied by

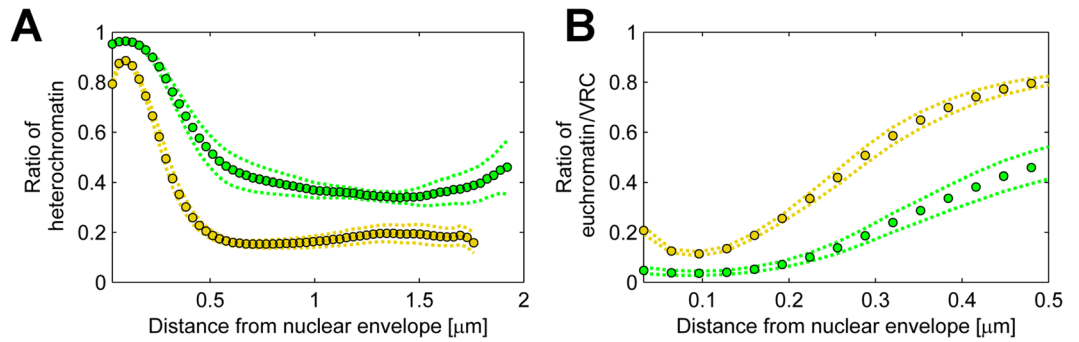


Figure 4. Relative distribution of cellular heterochromatin and viral VRC. (A) The relative amount of heterochromatin in infected (yellow) and non-infected (green) cells as a function of distance from the NE. (B) The relative amount of euchromatin/VRC in infected (yellow) and non-infected (green) cells at increasing distances from the NE. Dotted error lines represent the mean \pm SEM.

euchromatin ($64 \pm 6 \mu\text{m}^3$, Fig. 3D). In contrast, the average heterochromatin volume remained relatively unaltered as a result of infection ($87 \pm 8 \mu\text{m}^3$ in infected cells, $94 \pm 8 \mu\text{m}^3$ in non-infected cells).

To determine the effects of viral infection on the 3D architecture of heterochromatin, we mapped the relative distribution of heterochromatin and euchromatin/VRC as a function of the distance from the NE. This analysis indicated that in the infected cells, 78% of the heterochromatin was concentrated in a band less than $0.5 \mu\text{m}$ thick in the nuclear periphery, next to the NE (Fig. 4A). This finding is consistent with the immunofluorescence analysis of infected cells, which showed that the heterochromatin marker was concentrated in the nuclear periphery (Fig. 2A). In the non-infected cells, 68% of the heterochromatin was located within $0.5 \mu\text{m}$ from the NE, and the rest was distributed through the inner nuclear regions (Fig. 4A), with the majority of the low LAC euchromatin. Notably, our analysis indicated that, in the infected cells, $15.0 \pm 0.7\%$ of the euchromatin/VRC was located within 160 nm from the NE, in contrast with only $4.1 \pm 1.0\%$ in the non-infected cells (Fig. 4B). This shows that infection increased the presence of low LAC nucleoplasm close to the NE, suggesting that the heterochromatin layer is discontinuous along the nuclear rim. In summary, our results indicate that the formation of VRC is accompanied by a profound modification of the nuclear architecture, including the expansion of the nucleus, the marginalization of host heterochromatin, and the emergence of the low-density areas in the nuclear periphery.

Simulations of the nuclear transport of HSV-1 capsids. To study the intranuclear transport of HSV-1 capsids at late infection, capsid motion was simulated with the time-domain random walk method where the diffusing particles are moved on a lattice and the waiting time between consecutive jumps is an exponentially distributed random variable. The model was used to simulate paths of HSV-1-sized particles (125 nm) in 3D reconstructions of nuclei generated from SXT orthoslices. Our aim was to determine how the chromatin geometry of the infected cells affects the diffusive transport of capsids to the NE.

Diffusion coefficients in the nucleus were set to the value $2 \times 10^{-2} \mu\text{m}^2/\text{s}$, consistent with the values observed in a recent study³⁰. The value was treated as a rough approximation, sufficient for analysing the timescales and properties of transport. Even though the diffusion coefficient was rather low, the diffusion coefficient of chromatin itself in non-infected cells is about one to two orders of magnitude lower than the value used for capsids here³¹. To avoid increased complexity, and to take into account that the infection-induced compaction is likely accompanied by stabilization of chromatin, chromatin motion was not included into the model.

The TEM data and fluorescence data of viral capsid protein VP5, imaged together with DAPI, showed that the viral capsids and VP5 stain were mostly located in the lower-density areas of the nucleus (VRC and euchromatin) but rarely in the denser heterochromatin regions (Fig. 1). Accordingly, the capsid motion was restricted to areas where the LAC values were below $0.34 \mu\text{m}^{-1}$ (Fig. 3A).

First, we simulated the motion of 30,000 virus-sized particles in every cell ($n = 7$, Fig. 5A and Supplementary Movie S2). The simulations showed that in the infected cell nuclei the median time for a randomly placed particle to reach the NE ranged between 2.5 and 21 minutes (Fig. 5B), while the average of these values over the cells was 9 ± 2 minutes (average \pm SEM). Since almost all the capsids (99.9%) were eventually (within the total simulated time of four hours) able to reach the NE, the nuclear chromatin had few areas enclosing and trapping the capsids inside. Next, we studied the restrictive effect caused by heterochromatin to transport times by allowing the capsids to move freely in the entire nucleus, regardless of the chromatin density. In these simulations, the median time to reach the NE was only about 15 seconds, which demonstrates that capsid transport to the NE is significantly limited by the presence of peripheral chromatin.

To study how the infection-induced changes in the chromatin geometry and density affect the capsid transport we also simulated capsid diffusion in the non-infected control cell nuclei. These studies revealed that transport times to the NE varied significantly. In four cells, the median time to reach the NE was relatively similar to that of the infected cells, but in the other three cells, the transport was either very slow or did not occur at all (Fig. 5B). This suggests that the chromatin distribution varied strongly between the non-infected cells. Some of the cells contained pathways through the chromatin that were wide enough to allow the simulated passage of capsids, whereas in others the chromatin layer did not allow capsid transport.

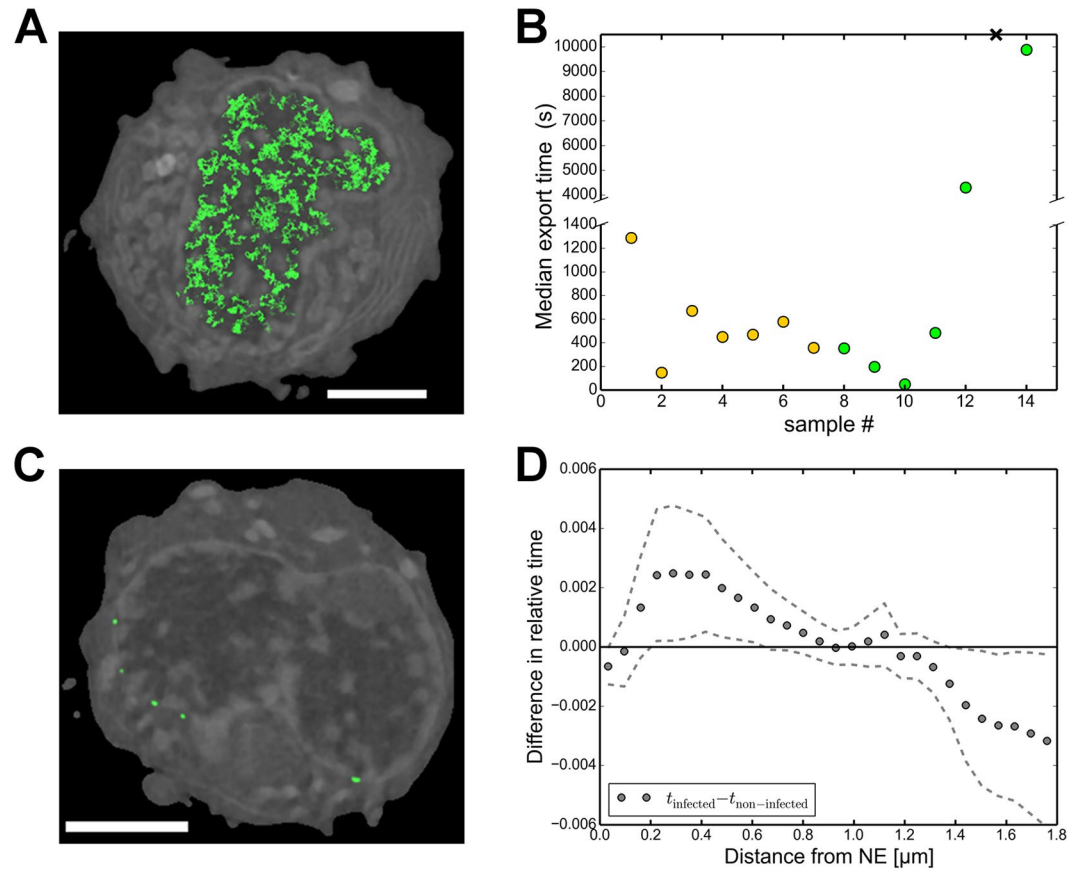


Figure 5. Nuclear transport of capsids to the NE. **(A)** Paths traced by 1000 capsids for 5 seconds (green) near one plane of the simulation geometry. The displayed path has a lower intensity when it is farther away from the SXT orthoslice shown as background (grey). Low and high LAC values of chromatin are indicated with dark and light greyscale values. Scale bar, 3 μm . See also Supplementary Movie S2. **(B)** Median transport times of capsids to the NE for infected (yellow) and non-infected (green) cells. The control cell with a cross symbol did not allow passage of capsids, and the median time is therefore not defined for it. The break in the y-axis separates low and high transport times. **(C)** Low-density nuclear egress sites of capsids (green) in an SXT cross-section of an infected cell. Scale bar, 3 μm . See also Supplementary Movie S3. **(D)** Difference in the relative amount of time spent by capsids at various distances from the NE between the infected and non-infected cells. Dotted error lines represent the mean \pm SEM.

Our earlier studies disclosed the induction of low-density virus-sized channels across the host chromatin in infection⁷. To examine the presence of export locations at the NE, we recorded the positions where the capsids arrived at the NE during the simulations (Fig. 5C and Supplementary Movie S3). In the infected cells on average $1.9 \pm 0.5\%$ of the lattice sites defining the nuclear envelope had a capsid arriving to them during the simulation. In the non-infected cells the value was $2.1 \pm 0.8\%$. In the infected cells, there were 150 ± 20 separate export locations at the NE, whereas in the non-infected cells there were 37 ± 17 export locations.

Finally, to study the effect of the marginalized chromatin on the distribution pattern of capsids over time, we recorded the total time spent by the particles for every lattice point in the nucleus. The lattice sites were then grouped based on their distance from the nuclear envelope, and the relative amount of time that the particles spent at every distance was calculated. Our analysis revealed that in the infected cells the capsids spent relatively longer time near the nuclear periphery than in the non-infected cells (Fig. 5D). A possible explanation for this behaviour is that in the control cells the capsids at these locations were already inside the peripheral chromatin layer, while in the infected cells, due to the chromatin being displaced more towards the edge, the capsids were still outside the chromatin layer, trying to find paths through it (Fig. 5D). This finding is consistent with our SXT analyses (Fig. 3), which showed that heterochromatin was located closer to the NE in infected cells than in non-infected cells. In the non-infected cells the capsids spent more time in the central parts of the nucleus, which can be explained by the more central distribution of chromatin which restricted the motion away from there. We also observed that a border within 0.5 μm from the NE restricted the flux of particles beyond this region (Supplementary Figure S4). This further shows that peripheral chromatin causes capsids to spend more time in the central parts of the nucleus devoid of chromatin, possibly diffusing around and seeking routes through the chromatin layer around them.

In summary, our simulations using the random walk model in 3D SXT reconstruction verified that the diffusion of viral capsids is limited by the compacted peripheral chromatin and that low-density channels through the chromatin layer are required to facilitate the viral transport and nuclear egress.

Discussion

Although HSV-1 infection is known to cause marginalization of the host chromatin, the quantitative effects on the density and organization of chromatin, and whether chromatin limits capsid translocation towards the NE, are not known. By combining SXT, TEM and confocal imaging techniques with advanced image analysis and numerical modelling, we revealed the condensation of chromatin and restricted mobility of the viral capsids in it.

Our studies confirmed that the emergence of an enlarged VRC was accompanied by the exclusion of host chromatin and its marginalization into the nuclear periphery. The analysis of heterochromatin distribution showed that it was enriched in the nuclear periphery both in infected and non-infected cells. Because the heterochromatin distribution did not change much during the infection, it is probable that the observed exclusion of chromatin from the nuclear centre is due to active euchromatin being relocated towards the nuclear periphery of the infected cells. This is in line with earlier HSV-1 studies showing that the expression of some genes is maintained or increased in infection^{10–13}. Moreover, HSV-1 proteins are known to be able to influence chromatin status towards either the loosely packed, transcriptionally active euchromatin, or towards inactive condensed heterochromatin^{14–16, 24, 25, 32–34}.

Our SXT analysis showed that the late stage of HSV-1 infection triggers an extensive modification of nuclear size and host chromatin organization. Both the mean volume of the nucleus and cytoplasm were increased in the infected cells. Notably, heterochromatin enrichment near the nuclear periphery was accompanied by compaction of the host chromatin. The HSV-1-induced changes in the nucleus have been studied intensely by light- and electron-based imaging techniques. These studies have verified increases in the nuclear volume and marginalization of the host genome^{5, 6, 35}. However, these approaches are confronted with fundamental limitations in 3D imaging of the architecture of the entire nucleus and/or in quantitative analysis of the molecular composition of nuclear chromatin compartments. SXT imaging circumvents these shortcomings by using comparatively short wavelengths of soft x-rays, which enables high-resolution 3D imaging of the nuclear architecture and quantitative assessment of the molecular density of nuclear structures including chromatin^{7, 22, 36}.

Our simulations of particle distribution in a 3D SXT chromatin reconstruction revealed that the marginalized chromatin indeed acts as an obstacle to the virus-sized particle motion. This suggests that the compact layer of host heterochromatin constitutes an accessibility barrier for the translocation of viral capsids towards the inner nuclear membrane across which they exit the nucleus. However, infection-induced breaks in the marginalized chromatin enable the capsid motion through it⁷. The simulations showed that the virus-sized particles were able to move to numerous locations at the NE in the infected cell chromatin geometries. This suggests that at any given moment there are sufficient channels through the chromatin to allow the passage of capsids. Moreover, our results demonstrate that the immobile chromatin network assumed in the simulations is sufficient for capsid egress, suggesting that chromatin motion is not necessarily required for it. Furthermore, diffusion seems to be an adequate method for capsid transport to the NE, which supports the idea of passive transport of capsids in the nucleus. This is in line with recent studies concluding that the motility of capsids is a process based on passive diffusion^{30, 37}.

Studying the capsid motion *in silico* allows us to change the details of the model and to examine a hypothetical case where the capsids can move regardless of the surrounding chromatin densities. When the capsids were allowed to travel in the entire nucleus, without the presence of restricting chromatin, capsid transport to the NE was significantly faster. This reveals the strong effect that the exclusion of capsids by the dense chromatin has on capsid export dynamics. Comparing the transport in infected cells to those in control cells, we observed that the transport times to the NE were more consistent in the infected cells than in the non-infected cells. This suggests that the changes to the chromatin geometry, low-density channels across the host chromatin in particular, are beneficial for capsid egress.

In summary, SXT imaging combined with advanced data analysis allowed us, for the first time, to demonstrate the HSV-1-induced molecular compaction of host chromatin. The modelling in the 3D SXT reconstruction of chromatin demonstrated that condensed chromatin in the infected cell nucleus constitutes an accessibility barrier and that there exist interchromatin channels allowing capsid transport to multiple locations at the NE.

Materials and Methods

Cells and viruses. To allow the long-term growth of B lymphocytes, the Abelson murine virus was used to infect them and to produce immortalized pre-B cell lines of a female mouse³⁸. The original cells were a gift from Barbara Panning (UCSF School of Medicine, Biochemistry and Biophysics, San Francisco, CA, USA). Cells were maintained as suspension cultures by a procedure described in ref. 7. The HSV-1 strain 17+ expressing EYFP-ICP4 (vEYFP-ICP4) was a generous gift from R. Everett (MRC Virology Unit, Glasgow, Scotland, UK³⁹). The viruses had been isolated as described in ref. 39. To infect the cells, they were inoculated with HSV-1 or HSV-1 EYFP-ICP4 at an MOI of 5–10 and kept at 37 °C until live-cell microscopy, fixation, and SXT analysis.

Confocal microscopy studies. For immunolabelling studies, cells were infected with HSV-1 or vEYFP-ICP4 HSV-1 at an MOI of 5. The cells were collected by centrifugation (400 RCF for 5 min) at 24 h p.i., spread and air dried on Zeiss high performance cover glasses (D = 0.17 mm, size 18 × 18 mm), after which they were fixed with 4% paraformaldehyde (PFA; 20 min at room temperature [RT]). Capsid protein VP5-specific monoclonal antibody (MAb; Santa Cruz Biotechnology Inc. Dallas, TX, USA) was used to detect viral capsids, followed by goat anti-mouse Alexa 594 secondary antibody (Ab; Thermo Fisher Scientific, Massachusetts, USA). Modified histones were labelled with rabbit antibody against H3K9me3 (Abcam, Cambridge, UK) followed by goat anti-rabbit Atto 647 (Abcam) conjugated secondary Ab. The nuclear lamina was detected with a lamin

B1-specific Ab (Abcam) followed by anti-rabbit Alexa 647 conjugated secondary Ab (Thermo Fisher Scientific). DNA was stained in the embedding stage with 4'-6-diamidino-2-phenylindole (DAPI)-containing ProLong anti-fade reagent (Thermo Fisher Scientific).

The immunolabelled cells were imaged using Nikon A1R laser scanning confocal microscope (Nikon Instruments Inc., Melville, USA) with CFI Plan Apo VC 60XH oil immersion objective (N.A 1.4). DAPI and EYFP were excited with a 405 nm diode laser and a 514 nm argon laser, respectively. DAPI fluorescence was detected with a 450/50 nm band-pass filter and EYFP fluorescence with a 540/30 nm band-pass filter. A 561 nm sapphire laser was used to excite Alexa 594, and the fluorescence was collected with a 595/50 nm band-pass filter. Atto 647 and Alexa 647 were excited with a 642 nm diode laser and the fluorescence was collected with a 660 nm long-pass filter. Stacks of 512×512 pixels were collected with a pixel size of 50 nm/pixel in the x- and y- directions, and 150 nm in the z-direction. Images were iteratively deconvoluted with Huygens Essential software (SVI, the Netherlands) using a signal-to-noise ratio of 7 and quality threshold of 0.01. Image analysis was done with ImageJ.

Co-localization analyses were done in ImageJ software using the JACoP plugin⁴⁰ with manually adjusted threshold values. The images were first denoised with a Gaussian blur, $\sigma = 2$, and then a binary image was generated with the Otsu threshold. After filling any holes, the amount and volume of objects were determined using the 3D Objects Counter plugin⁴⁰. Distance analysis of the fixed cell samples was done by first making a Euclidian distance map from an image of interest using Exact Euclidian Distance Transform (3D) plugin in ImageJ, and then comparing the original image against the distance map using an in-house Java code. The distance values were sorted to 0.1 μm -wide bins and the average intensity of the studied label was calculated for each bin.

Transmission electron microscopy. Infected cells and non-infected control cells were fixed in 4% paraformaldehyde and 0.25% glutaraldehyde in 50 mM phosphate buffer (at a pH of 6.8) followed by post-fixation in 1% OsO₄ for 1 h on ice. Cells were dehydrated with ethanol and then embedded in low-viscosity embedding resin (TAAB Laboratories Equipment Ltd, UK). Thin sections were cut by Ultracut UC6a ultramicrotome (Leica Mikrosysteme GmbH, Germany) followed by collection on Pioloform-coated, single-slot copper grids. Sections were double stained with 2% aqueous uranyl acetate and lead citrate and examined using TEM JEOL JEM1400 (JEOL Ltd., Tokyo, Japan), operated at 80 kV. The images were recorded using a bottom-mounted Quemesa CCD camera with 4008×2664 pixel resolution (EMSIS GmbH, Münster Germany).

Soft x-ray tomography. By a procedure described in ref. 7, mouse B cells were infected with vEYFP-ICP4 HSV-1, prepared and frozen into glass capillaries, and imaged using an XM-2 soft x-ray microscope in the National Center for X-ray Tomography (<http://ncxt.lbl.gov>) located at the Advanced Light Source (<http://www.als.lbl.gov>) of Lawrence Berkeley National Laboratory. Capillaries were kept in a stream of liquid nitrogen-cooled helium gas during data collection^{41,42}. This allowed data collection without any observable radiation damage. Each dataset contained 90–180 projection images collected sequentially around a rotation axis in $1\text{--}2^\circ$ increments, which gives a total rotation of 180° , using a 300–400 ms exposure time. The voxel size was 32 nm. Projection images were normalized²⁶ and then manually aligned using the IMOD software. Finally, tomographic reconstructions were calculated using iterative reconstruction methods^{43,44}. LAC values were determined as described previously⁴⁵.

Numerical simulations of capsid motion. Capsid diffusion in nuclei was simulated using the time-domain random walk method^{46–49}, where the probability for a random walker to jump from one lattice site to another is proportional to the harmonic average of the diffusion coefficients of the two sites and the time interval between two jumps is an exponentially distributed random variable. The simulation geometry was constructed using the SXT 3D images of the cells and, to get a more refined discrete representation of the diffusion dynamics, the lattice defined by the 32 nm pixels of the SXT images was subdivided by a factor of 4 to yield a lattice spacing of 8 nm for the simulations. The nuclei were divided into allowed regions, where the particle could diffuse freely, and into forbidden regions, where the particle was not allowed to travel, by setting a chromatin density limit for the particle motion. This density limit was defined as the minimum point between the two density populations in the LAC histogram (Fig. 3). The forbidden regions consisted of those areas where the centre of the particle was closer than its radius (62.5 nm) to a region that had too high a chromatin density. In the beginning of the simulation particles were placed randomly in the allowed regions of the nucleus, and during the simulations the arrival times of the particles to the NE and the arrival locations were recorded for each particle. From the arrival locations of the particles at the NE, distinct exit locations were identified by grouping contiguous pixels together. The number of particles was 30000 for every simulation.

References

- Kobiler, O., Lipman, Y., Therkelsen, K., Daubechies, I. & Enquist, L. W. Herpesviruses carrying a Brainbow cassette reveal replication and expression of limited numbers of incoming genomes. *Nat. Commun.* **1**, Article number: 146 (2010).
- Kobiler, O., Brodersen, P., Taylor, M. P., Ludmir, E. B. & Enquist, L. W. Herpesvirus replication compartments originate with single incoming viral genomes. *mBio* **2**, e00278–11 (2011).
- Lukonis, C. J. & Weller, S. K. Formation of herpes simplex virus type 1 replication compartments by transfection: requirements and localization to nuclear domain 10. *J. Virol.* **71**, 2390–9 (1997).
- Simpson-Holley, M., Baines, J., Roller, R. & Knipe, D. M. Herpes simplex virus 1 *U_L31* and *U_L34* gene products promote the late maturation of viral replication compartments to the nuclear periphery. *J. Virol.* **78**, 5591–5600 (2004).
- Randall, R. E. & Dinwoodie, N. Intranuclear localization of herpes simplex virus immediate-early and delayed-early proteins: evidence that ICP 4 is associated with progeny virus DNA. *J. Gen. Virol.* **67**, 2163–77 (1986).
- Monier, K., Armas, J. C., Etteldorf, S., Ghazal, P. & Sullivan, K. F. Annexation of the interchromosomal space during viral infection. *Nat. Cell Biol.* **2**, 661–5 (2000).

7. Myllys, M. *et al.* Herpes simplex virus 1 induces egress channels through marginalized host chromatin. *Sci. Rep.* **6**, 28844 (2016).
8. Ihalainen, T. O. *et al.* Parvovirus induced alterations in nuclear architecture and dynamics. *PLoS One* **4**, e5948 (2009).
9. Nagamine, T., Kawasaki, Y., Abe, A. & Matsumoto, S. Nuclear marginalization of host cell chromatin associated with expansion of two discrete virus-induced subnuclear compartments during baculovirus infection. *J. Virol.* **82**, 6409–18 (2008).
10. Esclatine, A., Taddeo, B., Evans, L. & Roizman, B. The herpes simplex virus 1 UL41 gene-dependent destabilization of cellular RNAs is selective and may be sequence-specific. *Proc. Natl. Acad. Sci. USA* **101**, 3603–8 (2004).
11. Mossman, K. L. *et al.* Herpes simplex virus triggers and then disarms a host antiviral response. *J. Virol.* **75**, 750–8 (2001).
12. Nyström, K. *et al.* Real time PCR for monitoring regulation of host gene expression in herpes simplex virus type 1-infected human diploid cells. *J. Virol. Methods* **118**, 83–94 (2004).
13. Chew, T., Taylor, K. E. & Mossman, K. L. Innate and adaptive immune responses to herpes simplex virus. *Viruses* **1**, 979–1002 (2009).
14. Knipe, D. M. & Cliffe, A. Chromatin control of herpes simplex virus lytic and latent infection. *Nature Reviews. Microbiology* **6**, 211–21 (2008).
15. Guise, A. J., Budayeva, H. G., Diner, B. A. & Cristea, I. M. Histone deacetylases in herpesvirus replication and virus-stimulated host defense. *Viruses* **5**, 1607–1632 (2013).
16. Van Opdenbosch, N., Favoreel, H. & Van de Walle, G. R. Histone modifications in herpesvirus infections. *Biol. Cell* **104**, 139–64 (2012).
17. Lorenz, M. *et al.* A single herpesvirus protein can mediate vesicle formation in the nuclear envelope. *J. Biol. Chem.* **290**, 6962–74 (2015).
18. Bigalke, J. M., Heuser, T., Nicastrò, D. & Heldwein, E. E. Membrane deformation and scission by the HSV-1 nuclear egress complex. *Nat. Commun.* **5**, Article number: 4131 (2014).
19. Funk, C. *et al.* The herpes simplex virus protein pUL31 escorts nucleocapsids to sites of nuclear egress, a process coordinated by its N-terminal domain. *PLoS Pathog.* **11**, e1004957 (2015).
20. Hagen, C. *et al.* Structural basis of vesicle formation at the inner nuclear membrane. *Cell* **163**, 1692–701 (2015).
21. Do, M., Isaacson, S. A., McDermott, G., Le Gros, M. A. & Larabell, C. A. Imaging and characterizing cells using tomography. *Arch. Biochem. Biophys.* **581**, 111–21 (2015).
22. Le Gros, M. A. *et al.* Soft X-ray tomography reveals gradual chromatin compaction and reorganization during neurogenesis *in vivo*. *Cell Rep.* **17**, 2125–2136 (2016).
23. Callé, A. *et al.* Nucleolin is required for an efficient herpes simplex virus type 1 infection. *J. Virol.* **82**, 4762–73 (2008).
24. Bannister, A. J. & Kouzarides, T. Regulation of chromatin by histone modifications. *Cell Res.* **21**, 381–395 (2011).
25. Santos-Rosa, H. *et al.* Active genes are tri-methylated at K4 of histone H3. *Nature* **419**, 407–11 (2002).
26. Parkinson, D. Y., Knoechel, C., Yang, C., Larabell, C. A. & Le Gros, M. A. Automatic alignment and reconstruction of images for soft X-ray tomography. *J. Struct. Biol.* **177**, 259–66 (2012).
27. Parkinson, D. Y. *et al.* Nanoimaging cells using soft X-ray tomography. *Methods Mol. Biol.* **950**, 457–81 (2013).
28. Smith, E. A. *et al.* Correlative cryogenic tomography of cells using light and soft x-rays. *Ultramicroscopy* **143**, 33–40 (2014).
29. Hanssen, E. *et al.* Soft X-ray microscopy analysis of cell volume and hemoglobin content in erythrocytes infected with asexual and sexual stages of *Plasmodium falciparum*. *J. Struct. Biol.* **177**, 224–32 (2012).
30. Bosse, J. B. *et al.* Remodeling nuclear architecture allows efficient transport of herpesvirus capsids by diffusion. *Proc. Natl. Acad. Sci. USA* **112**, E5725–E5733 (2015).
31. Dion, V. & Gasser, S. M. Chromatin movement in the maintenance of genome stability. *Cell* **152**, 1355–64 (2013).
32. Smolle, M. & Workman, J. L. Transcription-associated histone modifications and cryptic transcription. *Biochim. Biophys. Acta* **1829**, 84–97 (2013).
33. Ferrari, K. J. *et al.* Polycomb-dependent H3K27me1 and H3K27me2 regulate active transcription and enhancer fidelity. *Mol. Cell* **53**, 49–62 (2014).
34. McKittrick, E., Gafken, P. R., Ahmad, K. & Henikoff, S. Histone H3.3 is enriched in covalent modifications associated with active chromatin. *Proc. Natl. Acad. Sci. USA* **101**, 1525–30 (2004).
35. Wild, P. *et al.* Exploring the nuclear envelope of herpes simplex virus 1-infected cells by high-resolution microscopy. *J. Virol.* **83**, 408–19 (2009).
36. Isaacson, S. A., Larabell, C. A., Le Gros, M. A., McQueen, D. M. & Peskin, C. S. The influence of spatial variation in chromatin density determined by X-ray tomograms on the time to find DNA binding sites. *Bull. Math. Biol.* **75**, 2093–117 (2013).
37. Bosse, J. B. *et al.* Nuclear herpesvirus capsid motility is not dependent on F-actin. *mBio* **5**, e01909–14 (2014).
38. D'Andrea, E., Saggioro, D., Fleissner, E. & Chieco-Bianchi, L. Abelson murine leukemia virus-induced thymic lymphomas: transformation of a primitive lymphoid precursor. *J. Natl. Cancer Inst.* **79**, 189–95 (1987).
39. Everett, R. D., Sourvinos, G. & Orr, A. Recruitment of herpes simplex virus type 1 transcriptional regulatory protein ICP4 into foci juxtaposed to ND10 in live, infected cells. *J. Virol.* **77**, 3680–9 (2003).
40. Bolte, S. & Cordelières, F. P. A guided tour into subcellular colocalization analysis in light microscopy. *J. Microsc.* **224**, 213–32 (2006).
41. McDermott, G., Le Gros, M. A., Knoechel, C. G., Uchida, M. & Larabell, C. A. Soft X-ray tomography and cryogenic light microscopy: the cool combination in cellular imaging. *Trends Cell Biol.* **19**, 587–95 (2009).
42. Le Gros, M. A., McDermott, G. & Larabell, C. A. X-ray tomography of whole cells. *Curr. Opin. Struct. Biol.* **15**, 593–600 (2005).
43. Mastronarde, D. N. In *Electron Tomography: Methods for Three-Dimensional Visualization of Structures in the Cell* 163–185 (Springer New York, 2006).
44. Stayman, J. W. & Fessler, J. A. Compensation for nonuniform resolution using penalized-likelihood reconstruction in space-variant imaging systems. *IEEE Trans. Med. Imaging* **23**, 269–84 (2004).
45. Weiss, D. *et al.* Tomographic imaging of biological specimens with the cryo transmission X-ray microscope. *Nucl. Instr. Meth. Phys. Res. A* **467**, 1308–11 (2001).
46. Delay, E., Porel, G. & Sardini, P. Modelling diffusion in a heterogeneous rock matrix with a time-domain Lagrangian method and an inversion procedure. *CR Geosci.* **334**, 967–73 (2002).
47. Bortz, A. B., Kalos, M. H. & Lebowitz, J. L. A new algorithm for Monte Carlo simulation of Ising spin systems. *J. Comput. Phys.* **17**, 10–18 (1975).
48. McCarthy, J. F. Continuous-time random walks on random media. *J. Phys. A* **26**, 2495–503 (1993).
49. Montroll, E. W. & Weiss, G. H. Random walks on lattices. II. *J. Math. Phys.* **6**, 167–81 (1965).

Acknowledgements

We thank the staff of Advanced Light Source (Lawrence Berkeley National Laboratory, Berkeley, CA) for providing a safe, reliable source of photons used for imaging the cells in the present study. The SXT research was conducted at the National Center for X-ray Tomography (NCXT), and first-class experimental support by Rosanne Boudreau is gratefully acknowledged. We thank Liisa Lund, Arja Strandell, Mervi Lindman and Mervi Laanti for technical assistance, and Electron Microscopy Unit of the Institute of Biotechnology, University of Helsinki, for EM sample preparation. We are grateful to Klaus Hedman for his comments on the manuscript. The project was financed by the Jane and Aatos Erkkö Foundation (JT, MVR), the National Institute of General

Medical Sciences of the National Institute of Health, under the award number P41 GM103445, and the US Department of Energy, Biological and Environmental Research (DE-AC02-05CH11231, CAL) and the Academy of Finland, under the award numbers 138388 (MVR) and 259725 (VH). We acknowledge the financial support from the European Community's Seventh Framework programme NMP.2013.1.4-1 under Grant Agreement no. 604005 (KM).

Author Contributions

Conceived and designed the experiments: V.A., V.R., V.H., K.M., C.A.L., M.V.R. Performed the experiments: V.A., V.R., S.H. Analysed the data: V.A., M.M., V.R., E.M., J.V., T.K. Contributed reagents/materials/analysis tools: V.H., T.K., J.T., K.M., C.A.L., M.V.R. Wrote the paper: V.A., V.R., E.M., J.T., C.A.L., M.V.R. All authors reviewed the manuscript.

Additional Information

Supplementary information accompanies this paper at doi:[10.1038/s41598-017-03630-y](https://doi.org/10.1038/s41598-017-03630-y)

Competing Interests: The authors declare that they have no competing interests.

Publisher's note: Springer Nature remains neutral with regard to jurisdictional claims in published maps and institutional affiliations.



Open Access This article is licensed under a Creative Commons Attribution 4.0 International License, which permits use, sharing, adaptation, distribution and reproduction in any medium or format, as long as you give appropriate credit to the original author(s) and the source, provide a link to the Creative Commons license, and indicate if changes were made. The images or other third party material in this article are included in the article's Creative Commons license, unless indicated otherwise in a credit line to the material. If material is not included in the article's Creative Commons license and your intended use is not permitted by statutory regulation or exceeds the permitted use, you will need to obtain permission directly from the copyright holder. To view a copy of this license, visit <http://creativecommons.org/licenses/by/4.0/>.

© The Author(s) 2017

IV

ACTIN-PROPELLED NAVIGATION OF BACULOVIRUS THROUGH THE CHROMATIN NETWORK

by

Aho, V., Ohkawa, T., Chen, J. H., Kühn, T., Mattila, K., Volkman, L., Larabell, C. A.,
Welch, M. D. & Vihinen-Ranta, M.

Manuscript, 2018